UNIVERSIDADE FEDERAL DO CEARÁ
CENTRO DE CIÊNCIAS
PROGRAMA DE PÓS-GRADUAÇÃO EM QUÍMICA

ANTÔNIO ALVERNES CARNEIRO CRUZ

SENSING STRATEGY DEVELOPMENT FOR IDENTIFICATION OF TRACE ELEMENTS AND MYELODYSPLASTIC SYNDROME BASED ON FLUORESCENT DOPED CARBON QUANTUM DOTS

FORTALEZA
2022

ANTÔNIO ALVERNES CARNEIRO CRUZ

SENSING STRATEGY DEVELOPMENT FOR IDENTIFICATION OF TRACE ELEMENTS AND MYELODYSPLASTIC SYNDROME BASED ON FLUORESCENT DOPED CARBON QUANTUM DOTS

Doctoral dissertation submitted to the Graduate Program in Chemistry of the Federal University of Ceará, as a partial requirement to obtain the title of PhD in Chemistry. Area of concentration: Physical Chemistry.

Supervisor: Prof. Dr. Pierre Basílio Almeida Fechine.
Cosupervisor: Prof. Dr. Rafael Melo Freire.

FORTALEZA

2022

Dados Internacionais de Catalogação na Publicação
Universidade Federal do Ceará
Sistema de Bibliotecas
Gerada automaticamente pelo módulo Catalog, mediante os dados fornecidos pelo(a) autor(a)

C96s Cruz, Antoônio Alvernes Carneiro.
Sensing strategy development for identification of trace elements and myelodysplastic syndrome based on fluorescent doped carbon quantum dots / Antoônio Alvernes Carneiro Cruz. – 2023.
120 f. : il. color.

Tese (doutorado) – Universidade Federal do Ceará, Centro de Ciências, Programa de Pós-Graduação em Química, Fortaleza, 2023.
Orientação: Prof. Dr. Pierre Basílio Almeida Fechine .
Coorientação: Prof. Dr. Rafael Melo Freire.

1. Pontos quânticos de carbono. 2. Dopoagem. 3. Sensor nariz químico. 4. ConBr. 5. Quimiometria. I. Título.

CDD 540

ANTÔNIO ALVERNES CARNEIRO CRUZ

SENSING STRATEGY DEVELOPMENT FOR IDENTIFICATION OF TRACE ELEMENTS AND MYELODYSPLASTIC SYNDROME BASED ON FLUORESCENT DOPED CARBON QUANTUM DOTS

Doctoral dissertation submitted to the Graduate Program in Chemistry of the Federal University of Ceará, as a partial requirement to obtain the title of PhD in Chemistry. Area of concentration: Physical Chemistry.

Aprovada em: __/__/____.

BANCA EXAMINADORA

_____
Prof. Dr. Pierre Basílio Almeida Fechine (Supervisor)
Universidade Federal do Ceará (UFC)

_____
Prof. Dr. Francisco Audisio Dias Filho
Universidade Federal do Ceará (UFC)

_____
Prof. Drª. Gisele Simone Lopes
Universidade Federal do Ceará (UFC)

_____
Prof. Drª. Flávia Oliveira Monteiro Da Silva Abreu
Universidade Estadual do Ceará (UECE)

_____
Prof. Dr. Livia Paulia Dias Ribeiro
Universidade da Integração Internacional da Lusofonia Afro-Brasileira (UNILAB)

A Deus.

Aos meus pais, Francisco de Araújo Cruz e Francisca Lucelina Carneiro Cruz, que sempre estiveram presentes e trabalharam muito para garantir uma boa educação para mim e meus irmãos.

Aos meus irmãos, Francisca Tatianne Carneiro Cruz e Antônio Eriko Carneiro Cruz, por serem grandes irmãos e amigos. A minha Tia Maria Lurdes Carneiro por todo seu apoio.

A todos os meus amigos que contribuíram de alguma forma para a realização desse trabalho.

AGRADECIMENTOS

Ao CNPQ, pelo apoio financeiro com a manutenção da bolsa, e ao Departamento de Pós-Graduação em Química pela disponibilização da vaga para que eu pudesse concluir a pós-graduação.

Ao professor e amigo Pierre Basílio Almeida Fechine e Lillian Fechine, por toda paciência para a orientação durante o tempo do doutorado e pela enorme contribuição para a minha formação profissional e pessoal.

A todos os integrantes do laboratório GQMat da Universidade Federal do Ceará pelo grande apoio e pela amizade.

Aos amigos que fiz durante toda a pós-graduação, pois estes contribuíram diretamente para a minha formação profissional e cidadã.

Agradeço a todas as pessoas que ajudaram, direta ou indiretamente, para a minha formação acadêmica e pessoal.

Aos professores participantes da banca examinadora pelo tempo e pelas valiosas colaborações e sugestões.

A Nayane Amorim, Kedma Roque, Rosenda, Helainne Alilad, Arthur Grangeiro, Kelton Wadson, Alan Ibiapina, Alexandre Lima, Edicarlos Lopes e Carolina Marques, amigos verdadeiros que sempre me incentivaram a seguir em frente, por suas reflexões, críticas e sugestões.

Ao Valter Filho, Sostenes Cruz e Ivone Mary pelo companheirismo no final do doutorado e que estiveram nos momentos de aprendizado na minha vida.

A Edina Ribeiro pelo companheirismo desde o início da minha graduação e sempre. Especialmente ao Rafael Freire e à professora Selma Mazzetto, pois talvez não existam palavras suficientes e significativas que me permitam agradecer com justiça e com o devido merecimento. A ajuda e o apoio de vocês foram para mim de valor inestimável e tudo o que me resta é expressar através da limitação de meras palavras e com elas prestar-lhes esta humilde, mas sincera homenagem. Muito obrigado.

“Há uma força motriz mais poderosa que o vapor, a eletricidade e a energia atômica: A vontade.” (Albert Einstein)

RESUMO

Os Pontos Quânticos de Carbono (CQDs) receberam enorme atenção ao longo dos últimos anos devido às suas propriedades químicas, eletrônicas e ópticas. Neste trabalho, uma série de CQDs dopados com N, P e S foram sintetizados e suas propriedades ópticas e estruturais avaliadas. A rota sintética selecionada foi a termólise, com o ácido cítrico (AC), etilenodiamina, ácido fosfórico e ácido mercaptosuccínico atuando como fontes de C, N, P e S, respectivamente. Além disso, a ureia foi utilizada como fonte de N para síntese de CQDs diferentes cores. Os CQDs obtidos possuíram diâmetros na faixa de 1-4 nm e apresentam os grupos funcionais previamente escolhidos, além de carbono desordenado. Posteriormente, uma abordagem baseada no "nariz" foi desenvolvida usando um conjunto com quatro distintos *CQDs - ConBr* dopados com N, P e S, o que permitiu adquirir padrões de fluorescência diferentes e reprodutíveis para três carboidratos (glicose, manose e Metil-α-D-mannopironosideo) em uma faixa de concentração entre 30-800 μmol L^{-1}. Posteriormente, o reconhecimento de padrões foi realizado utilizando análise linear discriminante (LDA) e 36 amostras foram corretamente identificadas, com 100% de acurácia. Em seguida, um sensor multicanal foi desenvolvido com uma mistura de dois CQDs para a identificação de íons metálicos (Co^{2+}, Cu^{2+}, Mg^{2+}, Mn^{2+}, Fe^{2+}, Mo^{2+} e Zn^{2+}) na faixa de concentração de 100-700 μmol L^{-1}. Os resultados obtidos foram tratados por análise de componentes principais (PCA) seguidos de LDA. Além disso, outra abordagem baseada no "nariz" foi desenvolvida usando um conjunto com três distintos *CQDs -ConBr* (copados com P e S), o que nos permitiu adquirir padrões de fluorescência diferentes e reprodutíveis para amostras de sangue periférico e médula óssea de pacientes acometidos pela síndrome mielodisplásica (SMD).

Palavras-chave: pontos quânticos de carbono; dopagem; sensor nariz químico; *ConBr*; sensor multicolorido; quimiometria.

ABSTRACT

Carbon Quantum Dots (CQDs) have received enormous attention over the past few years due to their chemical, electronic and optical properties. In this work, a series of CQDs doped with N, P and S were synthesized and their optical and structural properties evaluated. The synthetic route selected was thermolysis and citric acid (CA), ethylenediamine, phosphoric acid and mercaptosuccinic acid acted as sources of C, N, P and S, respectively. In addition, urea was used as a source of N for the synthesis of multicolored CQDs. The samples were structurally characterized and the results showed that the CQDs obtained had diameters in the range of 1-4 nm and present the previously chosen functional groups, in addition to disordered carbon. Subsequently, a "nose" approach was developed using a set of four distinct CQDs - Doped-ConBr (Doped = N, P and S), which allowed us to acquire different and reproducible fluorescence patterns for three carbohydrates (glucose, mannose and Methyl-α-D-mannopyroside) in a concentration range between 30-800 μmol L-1. Subsequently, pattern recognition was performed using linear discriminant analysis (LDA) and 36 samples were correctly identified, with 100% accuracy. Then, a multichannel sensor was developed with a mixture of two CQDs for the identification of metal ions (Co^{2+}, Cu^{2+}, Mg^{2+}, Mn^{2+}, Fe^{2+}, Mo^{2+}, Zn^{2+}) in the concentration range of 100-700 μmol L^{-1}. The results obtained were treated by principal component analysis (PCA) followed by LDA. In addition, another "nose" approach was developed using a set of three distinct CQDs - Doped-ConBr (Doped = P and S), which allowed us to acquire different and reproducible fluorescence patterns for peripheral blood and bone marrow samples. of patients affected by myelodysplastic syndrome (MDS).

Keywords: carbon quantum dots; doped; sensor array; *ConBr;* sensor multicolor; chemometrics.

SUMÁRIO

1. SYNTHESIS AND CHARACTERIZATION OF CQDs

1.1 Introduction

Nanotechnology is the science, engineering and technology conducted at the nanoscale, (which is about 1 to 100 nm) that enables the manipulation of materials to fit existing needs. Nanoscience and nanotechnology involve the ability to see and control individual atoms and molecules (OLAWOYIN, 2018). However, advanced materials in this range of size are called nanomaterials and comprise nanotubes, nanoforms, and a wide variety of nanoparticles. Figure 1 shows the nanometric dimension (10^{-9} m), compared to the other materials.

Figure 1- Nanometer scale when compared with other structures.

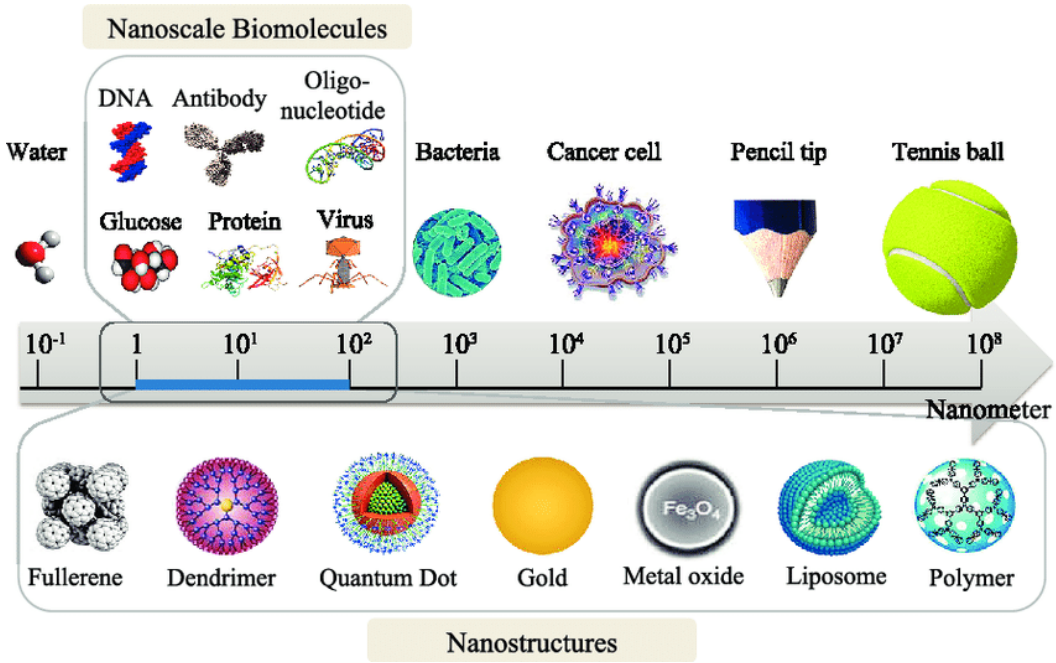

Source: (SAALLAH; LENGGORO, 2017)

Among nanomaterials, one class that has gained prominence in recent years is carbon-based nanomaterials. This element is one of the most abundant in the universe, existing in various allotropic forms in nature and as a major component of living organisms. Carbon may exist in nanometer scale: nanofibers, nanotubes, graphenes, fullerenes, and carbon quantum dots (CQDs), among others (HONG et al., 2015).

1.2 Carbon Quantum Dots (CQDs)

Carbon Quantum Dots (CQDs) are a new class of fluorescent nanomaterials that present unique optical properties such as tunable photoluminescence (PL) and excitation dependent multicolor emission (ZHU et al., 2015b; ZU et al., 2017). Iin comparison to other quantum dots (QDs) and organic probes, the CQDs also show low toxicity, biocompatibility and chemical inertness (KHAN; PATIL, 2020) (Figure 2).

Figure 2 - Schematic illustration of properties, syntheses and applications of CQDs, considering sensing strategy.

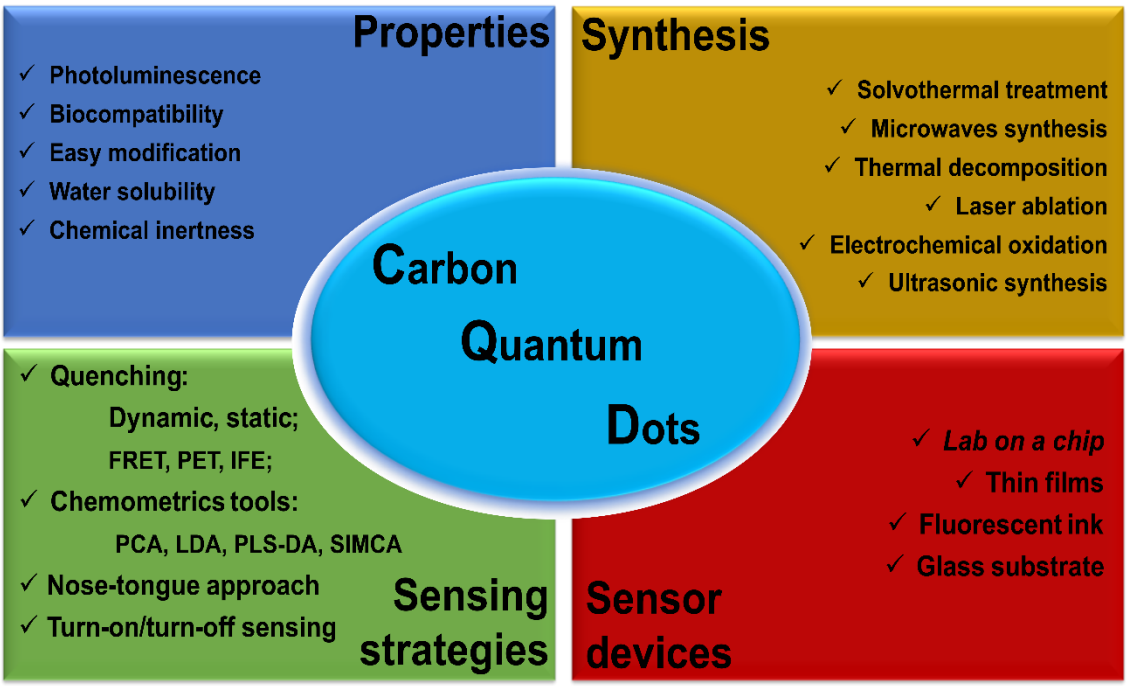

Source: (CRUZ et al., 2021)

The high fluorescence and good water solubility profiles are a consequence of the strong quantum confinement effect, surface defects and chromophores groups on their surfaces (RANI et al., 2020), which allow the application of CQDs in several areas such as photocatalysis (HUANG et al., 2021), photovoltaic cells (ALI et al., 2020), light-emitting diodes (LEDs)(LIN et al., 2020), drug delivery (NAIR et al., 2020), nanomedicine (DEVI; SAINI; KIM, 2019), biosensors (GHOLAMI et al., 2020) and chemical sensors (YI et al., 2021). In this sense, CQDs are great candidates for application in sensing analyzes as metal detection of Cr (VI) (LUO et al., 2021), Mn (VII) (HU et al., 2020) and Fe (III) (RAJA; SUNDARAMURTHY, 2020), and food security (CARNEIRO et al., 2019b; FAN et al., 2020;

KWAN et al., 2019).

CQDs were discovered accidentally in 2004 through an electrophoretic analysis of soot-derived carbon nanotubes (XU et al., 2004). In this work, fluorescent nanoparticles were observed, promoting a certain wondering regarding chemical structure of the obtained material. Then, many efforts were made to understand both composition and their application, where further the use in sensing strategies was started in 2010 by Gonçalves and collaborators in the sensing of Hg (II) (GONÇALVES et al., 2010). The authors obtained CQDs by direct laser ablation of carbon targets immersed in water and, after functionalization with NH_2–polyethylene-glycol (PEG_{200}) and N-acetyl-l-cysteine (NAC), the carbon nanoparticles become fluorescent. Generally, the design of fluorescent CQDs sensors is based on three strategies:

- The direct interaction between analytes and carbon dots, leading with the change of fluorescence signals of carbon dots (RAJA; SUNDARAMURTHY, 2020);
- Post-functionalization of CQDs, which is based on the conjugation of specific receptors and carbon dots to be applied as fluorescent sensors with high sensitivity and specificity (YI et al., 2021);
- Interaction of CQDs with other materials used in sensing, such as quenchers, fluorophores and substrates. For example, the fluorescence of a quenched CQD complex is recovered due to the breaking of quenching and combination of quencher molecules with analytes (SUN; LEI, 2017; SUN; WANG; LEI, 2015).

In this sense, CQDs have been applied in the development of sensors arrays, an important analytical approach to discriminate and classify a class of analytes with similar structures. Briefly, the analysis is obtained through collecting signals generated from a group of sensors, after their interaction with analytes. Hence, sufficient sensing units should be applied, and nonspecific interactions between sensors and analytes are necessary for the generation of cumulative responses (ASKIM; MAHMOUDI; SUSLICK, 2013; LI; ASKIM; SUSLICK, 2019). Indeed, CQDs are already a reality in the area of optical sensing, however, the unexplored possibilities are still searching for advanced applications.

1.3 Synthesis and structures

CQDs are nanomaterials constituted mainly by carbon with functional groups (−COOH,−OH,−NH_2,−CNH,−SH) on their surface, and heteroatoms (B, N, O, S, P) in the core of the structure (XU et al., 2004). These nanoparticles are obtained with a dimension between 1 and 10 nm and quasi-spherical shape (CARNEIRO et al., 2019b), where the chemical and

morphological properties can be adjusted, using the most appropriate synthesis method. In this perspective, CQDs are obtained from top-down and bottom-up approaches, as shown in figure 3.

Figure 3 – Schematic representation of CQDs synthesis methods.

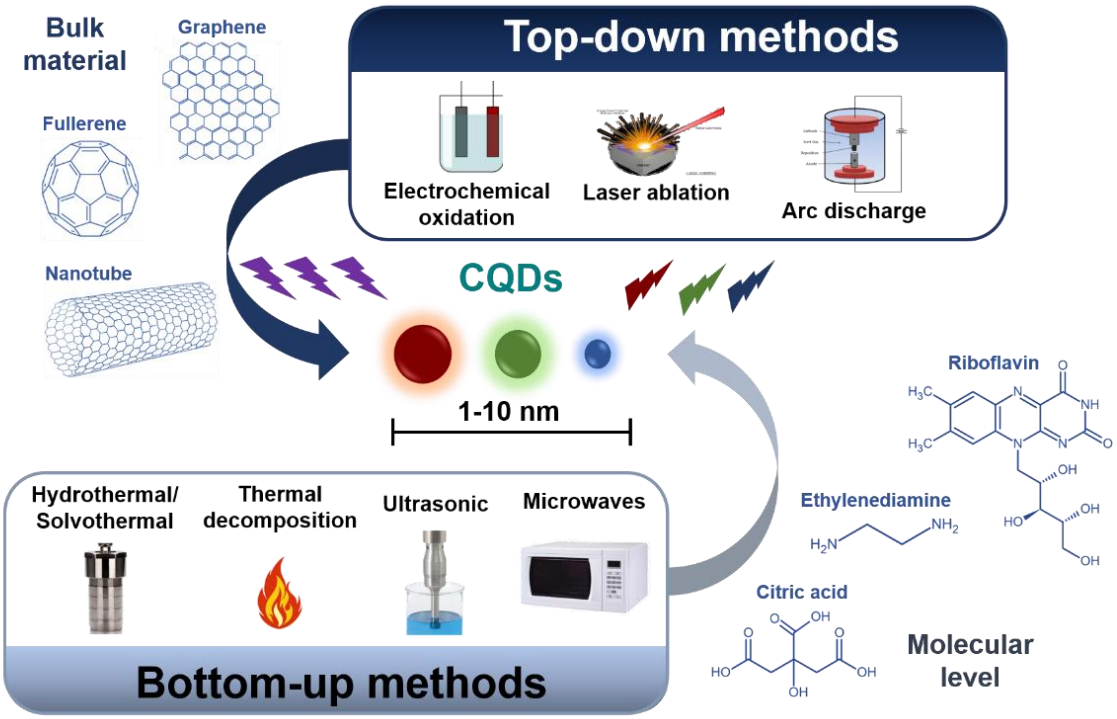

Source: (CRUZ et al., 2021)

Top-down synthesis consists of the breakdown of carbono macromolecules like graphite, carbon nanotubes and fullerenes using physical forces, such as laser ablation, arc discharge, or chemical oxidation. In Bottom-up synthesis, CQDs are formed through condensation/dehydrogenation of organic molecules used as carbon source through microwave synthesis, solvothermal treatment, thermal decomposition, or ultrasonic synthesis (KHAN; PATIL, 2020).

Since carbon-based macromolecules can be used in CQDs syntheses, the top-down approach offers high quality to final product, but involves complex and extreme experimental conditions instead (FAN et al., 2020). In contrast, reactional conditions of the bottom-up approach are easier and also present a low-cost synthetic route. In both methods, it requires additional post-purification steps, centrifugation, filtration or dialysis, to remove excess of unreacted reagents or intermediates formed during the synthesis. Besides, in the bottom-up process, there is the possibility of a scale-up production (YAO et al., 2019).

Considering bottom-up synthesis, most precursors are from natural sources such as potatoes, carrots, bananas, oranges (TEJWAN; SAHA; DAS, 2020), food residues, vegetable, fruit and cereal sub-products (FAN et al., 2020), and biomass residues (BORUAH et al., 2020)as well as compounds at molecular level like organic acids and carbohydrates (YAO et al., 2019).

Thus, in all synthetic routes, CQDs can be characterized with their photoluminescent properties, structurally and morphologically. For size analyzes, Transmission Electron Microscopy (TEM) and Atomic Force Microscopy (AFM) are suitable techniques for determination of both morphology and size particle distribution of CQDs. For instance, from TEM images of *Enteromorpha prolifera*-derived CQDs synthesized via hydrothermal treatment, it was possible to obtain a histogram of the CQDs, as shown in figure 4(a and b), in which was also observed the crystal lattice parameter of dots structure.

From AFM, the particle size distribution can be associated with height profiles, as shown in figure 4(c and d). The combination of both techniques show CQDs with spherical morphology and average diameter around 2.75 ± 0.12 nm, also presenting uniform dispersion without any aggregation (XU et al., 2017b). Indeed, considering CQDs light emission, generally, small particles are in the blue region whereas larger particles are in the red region.

Figure 4 – Techniques for size particle evaluation of CQDs: (a) TEM images of CQDs dispersion. Inset: HR-TEM; and (b) corresponding particle size distribution. (c) AFM topography image and (d) corresponding height profile.

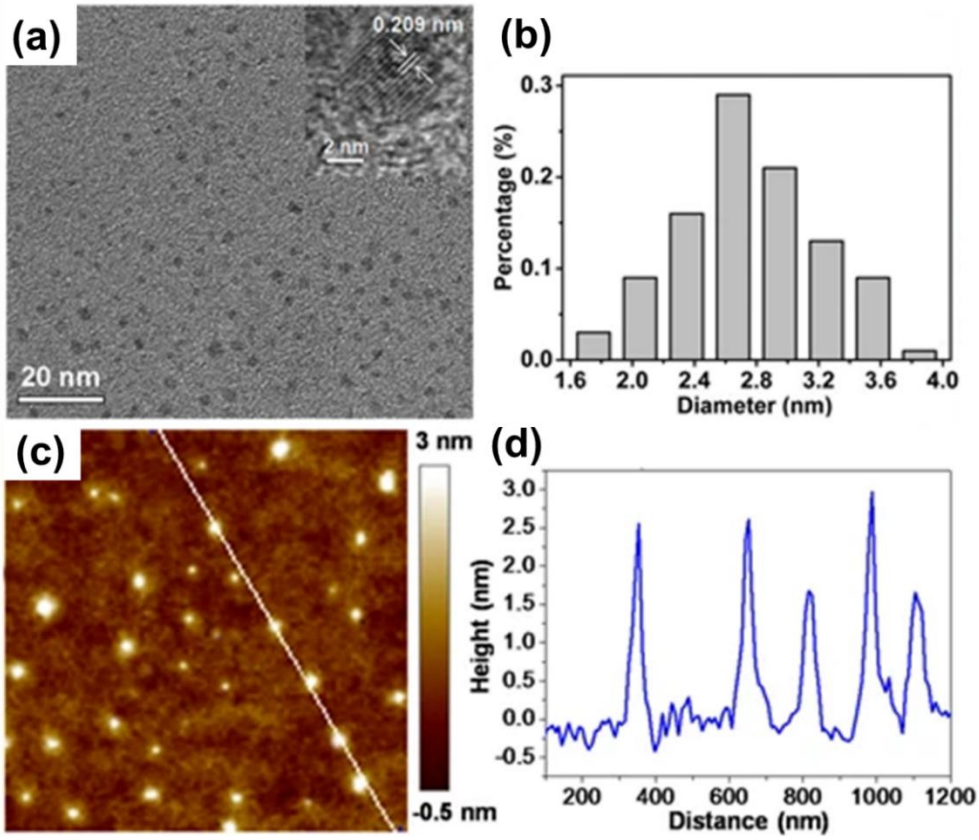

Source: Adapted from [Xu]. Copyright © 2017 by the authors, with permission from Springer Nature. This article is open access. Article distributed under the terms and conditions of the Creative Commons Attribution (CC BY) license (http://creativecommons.org/licenses/by/4.0/)

In addition, CQDs show a setup of characteristics that can be used to understand their chemical composition. In figure 5(a) is shown the luminescence emitted when the nitrogen-doped carbon quantum dots (N-CQDs), produced employing chitosan as precursor via hydrothermal, prepared in solid form and dispersed in solution are exposed under ultraviolet light, where it is observed the emission of blue light, depending on structural characteristics such as the presence of different functional groups, doping atoms, and particle size (YANG et al., 2020).

Figure 5 – Characterization methods for N-CQDs (a) solid-state and solution under UV light. (b) X-Ray Diffraction pattern. (c) Raman spectrum. (d) Fourier Transform Infrared (FTIR) spectrum. (e) UV-vis absorption spectrum. (f) PL spectra.

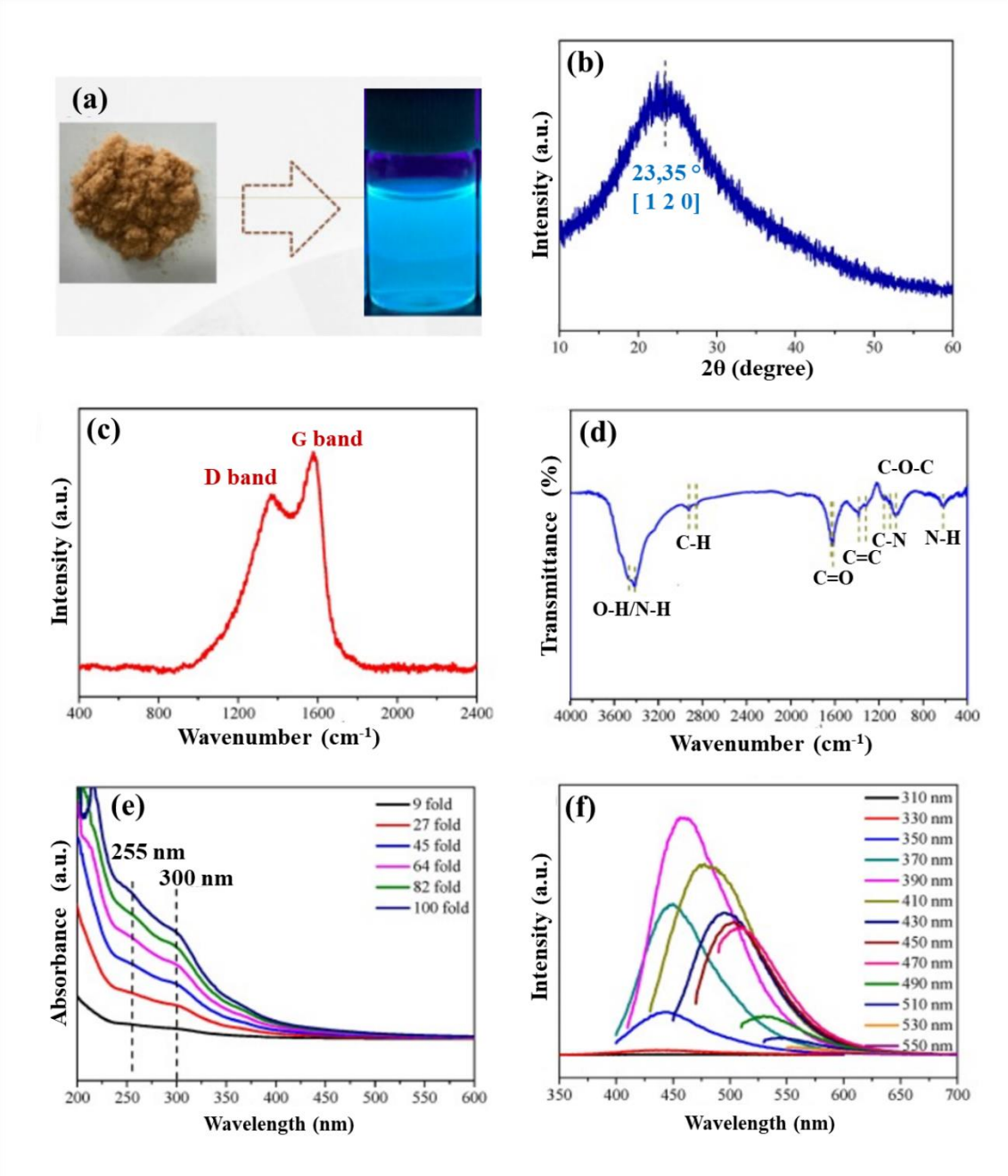

Source: Reproduced from [Yang et al]. Copyright ©2020 by the authors. Licensee MDPI, Basel, Switzerland. This article is open access. Article distributed under the terms and conditions of the Creative Commons Attribution (CC BY) license (http://creativecommons.org/licenses/by/4.0/).

The degree of graphitization of N-CQDs can be observed by X-ray diffractogram which exhibits a wide peak between 20º and 27º corresponding to irregular carbon atoms, as

shown in figure 5(b). The large characteristic peak at 2θ = 23.35º is attributed to the graphene peak, confirming surface defects in CQDs structure. By Raman, the confined electronic structure can be explored through G band, referring to the graphitic sp^2 carbon between 1200-1800 cm^{-1}, and D band, related to structural disorder of sp^3 carbon around 1370 cm^{-1}. Furthermore, the degree of crystallinity can be calculated using the ratio I_D/I_G between the two bands (ZHU et al., 2018a). A high value of $I_D/I_{G,}$ >1, indicates a high content of defects in CQDs.

For a low I_D/I_G value, <1, as shown in Figure 5(c), indicates a high graphitization or crystallinity. It is important to mention that the electronic states present in CQDs are dependent of both sp^2 and sp^3 hybridized carbons, as well as other functionalized surface defects, which must govern the multicolor emissions of CQDs, normally at blue and green regions of the visible light spectrum.

From FTIR, it is possible to identify the functional groups and the main vibrational modes present in the CQDs structure. This technique can be also used to verify changes on the surface of CQDs after post-modification reactions, since different experimental conditions might improve some desired properties. For instance, Figure 6(d) shows the presence of C=C, C=O and C-O-C groups around 1617, 1380 and 1045 cm^{-1}, respectively, related to most common vibrational modes of CQDs. However, after nitrogen doping, for example, a band in 1160 cm^{-1} referred to the presence of C – N stretching vibration is observed.

CQD shows interesting and numerous photophysical properties, such as fluorescence (ZHANG et al., 2020a), phosphorescence (FENG; XIE; ZHENG, 2020), chemiluminescence (LI et al., 2020), electrochemical luminescence (ZHOU et al., 2020) and up-conversion (HUANG et al., 2020). According to our knowledge, the origin of all observed luminescence behaviors is still unclear.

In this sense, UV-Vis and fluorescence spectroscopy are used to elucidate this property. Figure 5(e) displays the presence of two absorption peaks characteristic of CQDs at 235 and 300 nm, which correspond to transfer $\pi \rightarrow \pi^*$ and transfer $n \rightarrow \pi^*$, respectively (MA et al., 2020a).The π–π^* transition from C=C bonds and n–π^* transitions from C=O bonds, as well as the presence of functional groups, are responsible for photophysical properties of CQDs. The first occurs due to structural defects, the presence of heteroatoms or quantum confinement effect, while theanother one occurs through chemical changes, solvent polarity and pH. Furthermore, other bands at longer wavelength attributed to the π–π^* transitions can be observed, if the surface states contain C=N/C=O, C–O and C−S structures (DING; WEI; XIONG, 2014).

On the other hand, the fluorescence of CQDs can be explained by one of three theories:

- ***Defects on surface states*:** The defects on surface states are related to the functionalizing groups present on the surface of CQDs, once these groups have different levels of energy, they generate energy traps that contribute to the photoluminescence of the material(VASHISHT et al., 2020).
- ***Chromophore groups*:** The chromophore groups are related to small molecules of fluorophores that are consumed during the carbonization process and consequent formation of the carbonic nucleus of CQDs.
- ***Effect of quantum confinement:*** The quantum confinement effect is related to the size of the nanomaterial, where a smaller particle size provides a greater energy band gap. Thereby, the main energy band gap of CQDs is determined by the particle size range (KHAN et al., 2020). Bai and colleagues (BAI et al., 2020) determined the size of different CQDs using TEM, found mean values around 1.9, 2.8, 4.3 and 5.8 nm presenting bandgap values of 3.17, 3.13, 3.07 and 2.94 eV, respectively.

Besides, fluorescence spectra can be exhibited at different excitation wavelengths, which can result in an emission spectrum dependent or independent of the fluorescence. The spectrum of excitation dependents states exhibits different energy levels in the energy gap, where the displacement of the emission band at different excitation wavelengths is related by the surface defects, as shown in figure 6(f). This behavior directly affects its quantum yield (ϕ), which is low when compared to molecular chromophores. However, CQDs stability against photobleaching is improved, making advantageous for applications when compared to molecular fluorophores. ϕ is a property directly proportional to the amount of emission, and can be calculated using the following Equation:

$$\Phi = \Phi_{ref}\left(\frac{I}{I_{ref}}\right)\left(\frac{A_{ref}}{A}\right)\left(\frac{n}{n_{ref}}\right)^2 \quad \textbf{(1)}$$

Where I is the integrated area of the emission spectrum, A is the absorbance at the excitation wavelength, n is the refractive index of the solvent and the subscript *ref* is assigned to the values of the standard fluorophore (CARNEIRO et al., 2019b). It is important to highlight that the quantum yield can be modified by the presence of doping atoms in the structure. For example, a study mixing different proportions of phenylalanine and citric acid resulted in a significant increase in the quantum yield with the increase in the amount of nitrogen atoms present in the structures of CQDs(CHAHAL; YOUSEFI; TUFENKJI, 2020).

The value of Φ depends on another photophysical property of the CQDs, the lifetime (τ), which is a function of the rate of radiative decay and can be mathematically described by Equations **(2)** and **(3)**, respectively:

$$\Phi = \frac{k_r}{k_r + \Sigma k_{nr}} \quad \textbf{(2)}$$

$$\tau = \frac{1}{k_r + \Sigma k_{nr}} \quad \textbf{(3)}$$

and relating Equations **(2)** and **(3)**, Equation **(4)** is obtained:

$$\Phi = k_r \cdot \tau \quad \textbf{(4)}$$

where k_r is the rare constant of radiative decay, Σk_{nr} is the sum of all rate constant of nonradiative decay. The equations above show that the increase in Φ together with longer decay times are dependent of the k_r value.

Therefore, some functional groups anchored on CQDs surface can act as nonradiative traps to quench the photoluminescence. For example, an increase in photoluminescence, from 5.4 to 12.7%, and longer lifetime values, measured for the green and red components, was obtained when the -COOH group was anchored on the surface of CQDs, which normally act as nonradiative traps, interacting with cetyltrimethylammonium bromide. Then, the functionalization of CQDs surface was performed with addition of a cationic surfactant. In this case, interactions between $–COO^-$ and $CH_3(CH_2)_{12}N^+(CH_3)_3$ groups promoted an increase in green and red emissions(ZHU et al., 2017).

Additionally, lifetime of CQDs can be useful for a better understanding of the quenching mechanism, when used in sensing strategies(GUO; ZHAO, 2020). Zhu and collaborators(ZHU et al., 2020) obtained N-CQDs with a lifetime of 6.61 ns, whose value has not been changed when applied to the detection of the ions Hg^{2+} and Fe^{3+}, suggesting a static quenching mechanism. On the other hand, Jiang and collaborators(JIANG et al., 2020) obtained CQDs with a lifetime of 12.62 ns, varying to 11.83 ns after the addition of ClO^-, suggesting a dynamic quenching mechanism.

The optical properties of CQDs determined from their absorption and emission energies provide optical signals that allow their use in sensing strategies. Briefly, CQDs assume the role of fluorescent probes as chemical interactions occur to the analytes, which depend on the functional groups present on the surface of the nanoparticles and the analyzed molecules.

This results in changes in the fluorescence spectrum of CQDs: quenching or enhancing of fluorescence, displacement of the emission wavelength or even fluorescence lifetime (LUO et al., 2020). Then, variations in the optical properties of CQDs are easily observed, and from this data set, a rich data array is constructed. This database is used to build a recognition pattern (fingerprint) and to propose a sensing strategy, confinable, fast and sensitive to low concentrations of analytes.

1.4 OBJECTIVES

1.4.1 General

- To synthetize and characterize the non-doped and doped CQDs with N (nitrogen), S (sulfur) and P (phosphorus).

1.4.2 Specific

- To characterize photoluminescent properties the CQDs for UV-vis and fluorescence spectroscopy.
- To characterize a structural and morphological properties of the CQDs for X-ray photoelectron spectroscopy (XPS), Raman spectrum, Fourier-transform infrared spectroscopy (FTIR) and Atomic Force Microscopy (AFM).

1.5 EXPERIMENTAL

1.5.1 Materials

All reagents used in this work were of analytical grade and used as such without further purification. Citric acid anhydrous (99.5%, Sigma Aldrich), urea (99.5%, Aldrich) and N,N-Dimethylformamide (DMF, 99.5%, Aldrich), Sodium phosphate monobasic (NaH_2PO_4, 99%, Vetec) and sodium phospate dibasic heptahydrate (Na_2HPO_4, 99%, Vetec), phosphoric acid P.A (99,0%,Vetec), mercaptosuccinic acid (99,0%, Sigma Aldrich), ethylenediamine (98%, Vetec), dialysis membrane (0.5-1.0KDa, Spectrum Laboratories) and ultra-high Milli-Q water (resistivity of 18.2 $M\Omega.cm^{-1}$).

1.5.2 Synthesis of CQDs

The CQD-OH nanoparticle was synthesized following the work from Wang et al. (DONG et al., 2012) through the thermolysis of citric acid (CA). Briefly, 500 mg of citric acid (CA) were added into a 10 mL beaker. Then, it was leaded to the muffle, previously heated at 180°C, where remained for a period of 30 minutos After this step, the recipient was allowed to naturally cool down and the product was solubilized in Milli-Q water (resistivity of 18.2 $M\Omega$ cm^{-1}). Subsequently, the dispersion was purified by dialysis membrane for 24 hours. The final solution was lyophilized for further characterization and application.

The experimental aproach for CQD-X (X = S, N or P) synthesis was the same as that used for the CQD-OH nanoparticle. However, the following functionalizing agents were added to change the structure of the CQD: 500 mg of mercaptosuccinic acid, 500 μL of ethylenediamine and 500 μL of phosphoric acid to obtain CQD-S, CQD-N and CQD-P, respectively.

For CQD-$CONH_2$, the synthesis was carried out following *Chen et al*.(CHEN et al., 2016) by solvothermal method. Briefly, 1.0 g of the CA and 2.0 g of the urea precursors were dissolved in 20 mL of DMF and stirred to form a transparent solution. Then, the solution was transferred into a 25 mL Teflon-lined stainless autoclave. The sealed autoclave vessel was heated at 200 ºC and held for 6 hours. After that, the mixture was held in rest until be colled to room temperature. The material was purified by dialysis using membrane cut-off tubing in the range of 1 kDa, provided by Spectrum Laboratories, for 48hs. The final solution was lyophilized for further characterization and application.

1.5.3 CQDs Characterization

The optical properties of the CQDs were confirmed by using Uv-Vis spectrum in the spectrophotometer UV-Vis Shimadzu UV-2600. The fluorescence spectra of the CQDs were obtained in the Shimadzu RF-6000 spectrofluorophotometer. The structural characterization was performed in a X-ray photoelectron spectroscopy (XPS) (Physical Electronics Quantum 2000 spectrometer) using a monochromatic Al Kα excitation at a spot size of 10 mm with a pass energy of 46.95 eV. The CQDs structures were confirmed by FT-IR VERTEX 70V, (Bruker) and the Gaussian deconvolution of the Raman spectrum (LabRAM Jobin-Yvon, HORIBA) collected at λex = 785 nm. The Atomic Force Microscopy (AFM) image was obtained utilizing an Asphalt Research microscope of the MFP-3D AFM type.

1.5.4 Quantum yield

Quinine sulfate was used as a standard for determination of quantum yield of as-prepared CQDs. The fluorescence spectra of Quinine sulfate (in 0.1 M H_2SO_4) and CQDs solution as well as their absorbances were recorded at 350 nm. The following formula was used to calculate Quantum Yield. The quantum yield was calculated according to equation 1.

$$\phi = \phi_{ref} \left(\frac{I}{I_{ref}}\right) \left(\frac{A_{ref}}{A}\right) \left(\frac{n}{n_{ref}}\right)^2 \phi \quad (1)$$

1.6 RESULTS AND DISCUSSION

1.6.1 Photoluminescence property of CQDs.

The heteroatom doping effect of nonmetallic elements is a powerful approach to adjust intrinsic properties in CQD structure. The introduction of heteroatoms may alter the surface structure of electron distribution in CQDs, which is related to the energy gap between HOMO and LUMO, and thus affecting their fluorescence properties. The fluorescence efficiency of CQDs can increase and the emission peak can shift/change by adjusting of the quantities and types of heteroatom doping. In general, dopants of non-metallic elements can be used to significantly improve QY in CQDs (SONG et al., 2019). In this work, the CQDs were doping with nitrogen, phosphorus and sulfurum (CQD-N, CQD-P and CQD-S) for to significantly improve fluorescence and its optical properties of were investigated using UV–Vis and fluorescence spectrophotometers.

The UV–vis absorption and fluorescence spectra of CQDs are showed in Figure 6b. The absorption spectra of the CQD-P and CQD-S exhibited absorption peaks around at 300 nm, while for the CQD-OH and CQD-N exhibited peaks around at 340 nm and 355 nm, respectively. They can be atributted to the π-π^* transition of aromatic sp^2 domain and n-π^* transition of C=O bonds, as well as contribution from other surface groups, originated from the trapping of excited state energy by the surface states. The aqueous CQDs solution (Figure 6a) under visible light show yellow color. However, it is bright blue colour with high intensity when illuminated by UV light (DANG et al., 2019; FANG; ZHUO; ZHU, 2019; TRAVLOU et al., 2018).

The CQD-OH has an excitation dependent emission behavior because oxygen related groups (C-O, C=O and O= C-OH) producing various surface states corresponding to different energy levels below the HOMO. Thus, it induces different transition modes and a broad UV-vis absorption band. After surface doping with nitrogen, the emission can only occur via radiative transition of sp^2 carbon, leading to excitation independent fluorescence due to a switch from multiple transition modes to a single transition mode, producing a new surface state that traps electrons, increases radiative recombination and suppresses non-radiative recombination (LU et al., 2015).

Figure 6- a) photographs of CQD with daylight and UV light; b) Uv-Vis spectrum of CQD-OH, CQD-N, CQD-P and CQD-S; c, d, e and f) Emission spectra of CQD-OH, CQD-N, CQD-P and CQD-S for varying excitation wavelengths.

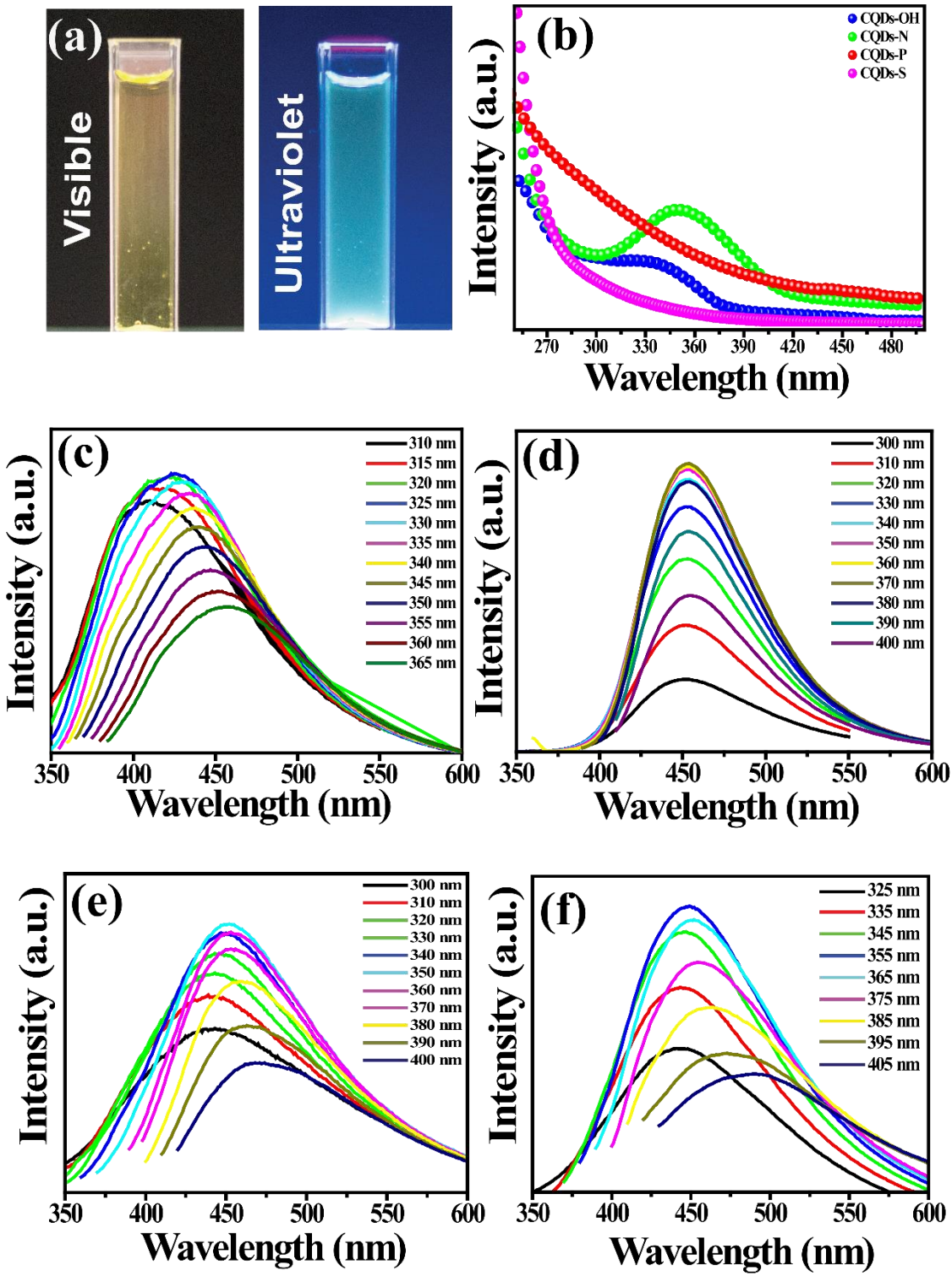

Source: author

CQD-P (Figure 6e) and CQD-S (Figure 6f) also present similar behaviour to CQD-OH (excitation wavelength dependent emission spectra). The excitation wavelengths of maximum emission intensity are about 325 nm, 350 nm, 355 nm, with an emission peak of 430 nm, 450 nm and 448 nm to CQD-OH, CQD-P and CQD-S**,** respectively. Phosphorus is located in group 15 of the periodic table, is larger than carbon. Therefore, the addition of phosphorus atoms in CQD produces more isolated sp^2 carbon clusters, increasing the bandgap into the UV-vis region and produces stronger fluorescence than individual sp^2 carbon clusters. Moreover, CQD-S showed a slight excitation dependent behavior dominated by substitution of sulfur atoms in the lattice in CQD-OH and $n-\pi^*$ transitions due to charge-injection, this arises because sulfur lattice substitutions that havelow electronegativity creating emissive trap states for photoexcited electrons, which modifies the band-gap energy (ZHOU et al., 2014)

As are shown in Figure 6d, photholuminescence emission intensity of the CQD-N did not present this property. The fluorescence emission peak at 453 nm remained unchanged when the excitation wavelength was increased from 300 to 400 nm. (DANG et al., 2019). The QY of CQD-OH, CQD-N, CQD-P and CQD-S were determined at excitation of 350 nm. The QY values using quinine sulfate as the reference were 0.75%, 25.93%, 0.54% and 0.59% for CQD-OH, CQD-N, CQD-P and CQD-S, respectively.

The QY value for CQD-N is highest than the other ones. CQD-OH has different kinds of surface states (labeled as O-states) corresponding to a relatively wide distribution of different energy levels to generate a broad UV/Vis absorption band and excitation-dependent emission spectra. The N doping gives rise to a new surface state (labeled as the N-state). Electrons trapped by this surface state are able to facilitate a high yield of radiative recombination. The QY of the CQD-N is higher than that of the CQD-OH. It seems that the introduced sulfur atoms would be able to eliminate the O-states, leading to that the original surface states nearly neglected in the CQD-S. Phosphorus doping can enhance the luminescence efficiency of CQDs, but this mechanism is still controversial (LU et al., 2015).

The high QY may be due to the coexistence of defect sites and isolated sp^2 carbon clusters, which increasing the bandgap into the UV-vis region and produces stronger fluorescence than individual sp^2 carbon clusters. The fluorescence enhancement may also arise from isolated sp^2 carbon clusters because the introduction of phosphorus into CQDs produces more isolated sp^2 carbon clusters, and the number of these clusters increases along with increasing phosphorus content. Moreover, the possibility that the formed defects produce fluorescence and that more defects intensify fluorescence cannot be eliminated. However, phosphorus doping can significantly improve the photostability of CQDs. P-related groups can

introduce a new energy-level above the HOMO of the CQDs (the so-called P-state) as these groups act as strong electron donors. Therefore, the CQD-P and CQD-S show a low quantum yield. The results suggest that N doping increased the QY of CQDs and the P and S doping reduced it (BIN et al., 2019).

1.6.2 Structural properties of CQDs.

Figure 7 illustrates Raman spectra of samples CQD-OH, CQD-N, CQD-P and CQD-S. The CQDs characteristic bands were easily observed with deconvoluted spectra. Clearly, both samples reveal D and G peaks in CQDs, with diferrence in peak positions, which is attribued to the presence of structural defects. The G band is associated with the vibration of sp^2 hybridized carbon atoms in the 2D hexagonal lattice of graphite and D band corresponds to the vibration of sp^3 hybridized carbon atoms in the termination plane of disordered grafite (KONAR et al., 2019; ZHU et al., 2015a).

As depicted in Figure 7 a, c and d the I_D/I_G = 0.66, 0.83 and 0.78 of CQD-OH, CQD-P and CQD-S, respectively, is slightly smaller than that of the CQD-N (I_D/I_G = 1.12), which indicate that the partial out plane vibrations of CQD-OH, CQD-P and CQD-S (sp^3 bond) are converted into in plane vibrations (sp^2 bonds). In relation to CQD-N, where small domains of graphitic structures are formed, the reason can be explained where CQD-N serve as both induce of the graphitic structure and extra nitrogen supplier for the N-doping (NIU et al., 2019).

Figure 7- Raman spectra of as prepared (a) CQD-OH, (b) CQD-N, (c) CQD-P and (d) CQD-S.

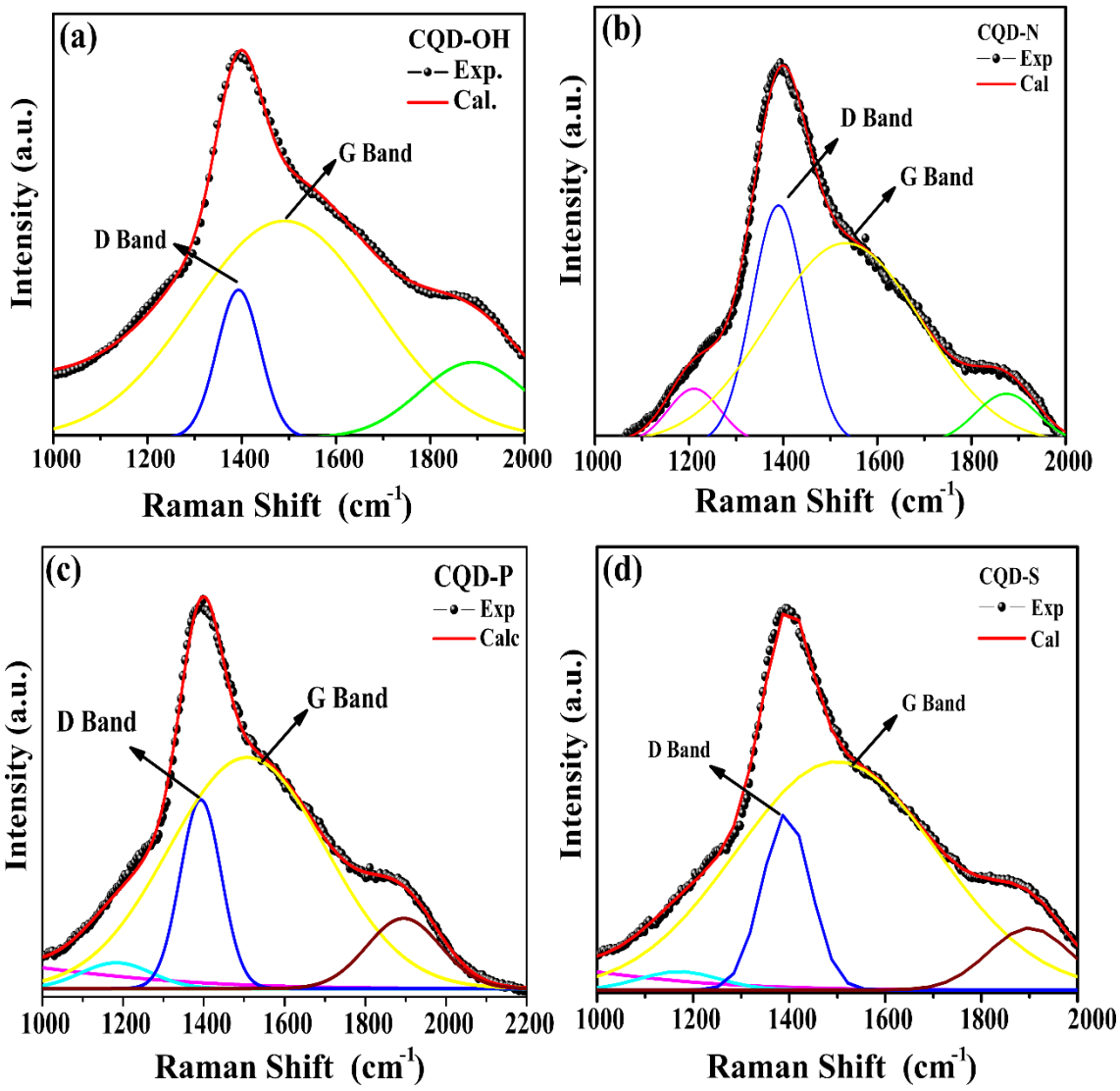

Source: author

A large I_D/I_G value indicates growing structural defects or an increasing amount of disordered carbon within CQDs, while a small I_D/I_G value reveals a highly crystalline core CQD. An I_D/I_G value of 0.7 is typical of graphite. The value to CQD-N is due to N-doping defects and exposed edge sites. The CQD-OH, CQD-P, CQD-S have values next or larger than 0.7 which indicates that the structure are graphite-like with a few disordered carbon structures. Heteroatom doping can affect the location and intensity of peaks in the Raman spectrum, As observed for CQD-OH, CQD-P and CQD-S, the D band is located at 1393 cm^{-1} and the G band at 1495 cm^{-1}, 1506 cm^{-1} and 1503 cm^{-1}, indicating that the G band has shifted when atoms of P and S were incorporated. However, for CQD-N there was a shift of the D band which is located in 1389 cm^{-1}, as well as the shift of band G in 1548 cm^{-1}.

X-ray photoelectron spectroscopy (XPS) measurements were carried out, to investiged which chemical bonds are present in CQDs, spectral deconvolutions were performed, obtaining bands whose binding energies are quantified and identified. In this perspective, the full-range XPS spectrum of CQD-OH shown C1s and O1s peaks corresponding to the binding energy values of 285 eV and 533eV, respectively (Figure 8a).

Figure 8- (a) XPS survey, (b) high-resolution XPS of C1s and (c) high-resolution XPS of O1s spectra of the CQD-OH.

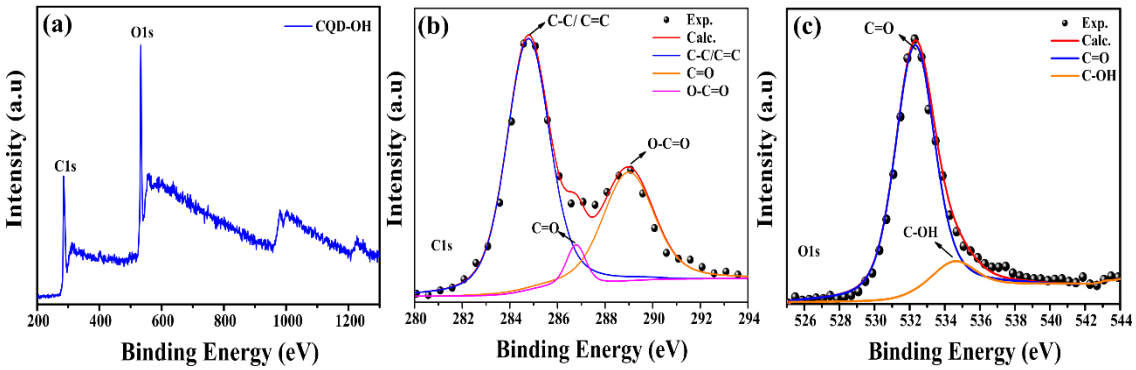

Source: author

XPS elemental analysis shows the composition of CQD-OH as C 59.96 % and O 34.48 %. The Figure 8b shown spectrum of C1s the peaks 284.6, 286.8 and 289 eV can be assigned to carbon in the form of C-C (sp^3), C=O (sp^2) and O-C=O (sp^2) (FREIRE et al., 2018; ONLINE, 2014; YU et al., 2016), respectively. The O1s spectrum (Figure 8c) can be deconvuled into two peaks of C=O at 532.7 and C-OH around 534.6 eV (MANIOUDAKIS et al., 2019; REN et al., 2018).

The full range XPS spectrum of CQD-N shown C1s, N1s and O1s peaks corresponding to the binding energy values of 285eV, 398ev and 530eV, respectively (Figure 9a). XPS elemental analysis shows the composition of CQD-N as C 68.03, N 7.9, O 24.06 %. In the high resolution C1s (Figure 9b), the binding energy peak at 284.6 eV confirms the graphitic structure sp^2 (C—C and C=C). The peak at about 286.3 eV suggests the presence of C—N, while the peak around 288.0 eV could be assigned to C=O (LIU et al., 2016; YOU; BE; IN, 2016). The high resolution N1s (Figure 9c) show two peaks 399.8 and 401.6eV were assigned to the absorption of C-N-C and N-H groups, respectively (LIAO et al., 2019; LIU et al., 2019; QU et al., 2014; YUAN et al., 2019). The O1s spectrum exhibited two peaks at 530.8 and 532.0 eV (fig. 10d), which can be assigned to the C=O and C-O-C/C-OH groups, respectively (LIM; SHEN; GAO, 2015).

Figure 9- (a) XPS survey, (b) high-resolution XPS of C1s, (c) high-resolution XPS of O1s and (d) high-resolution XPS of N1s spectra of the CQD-N.

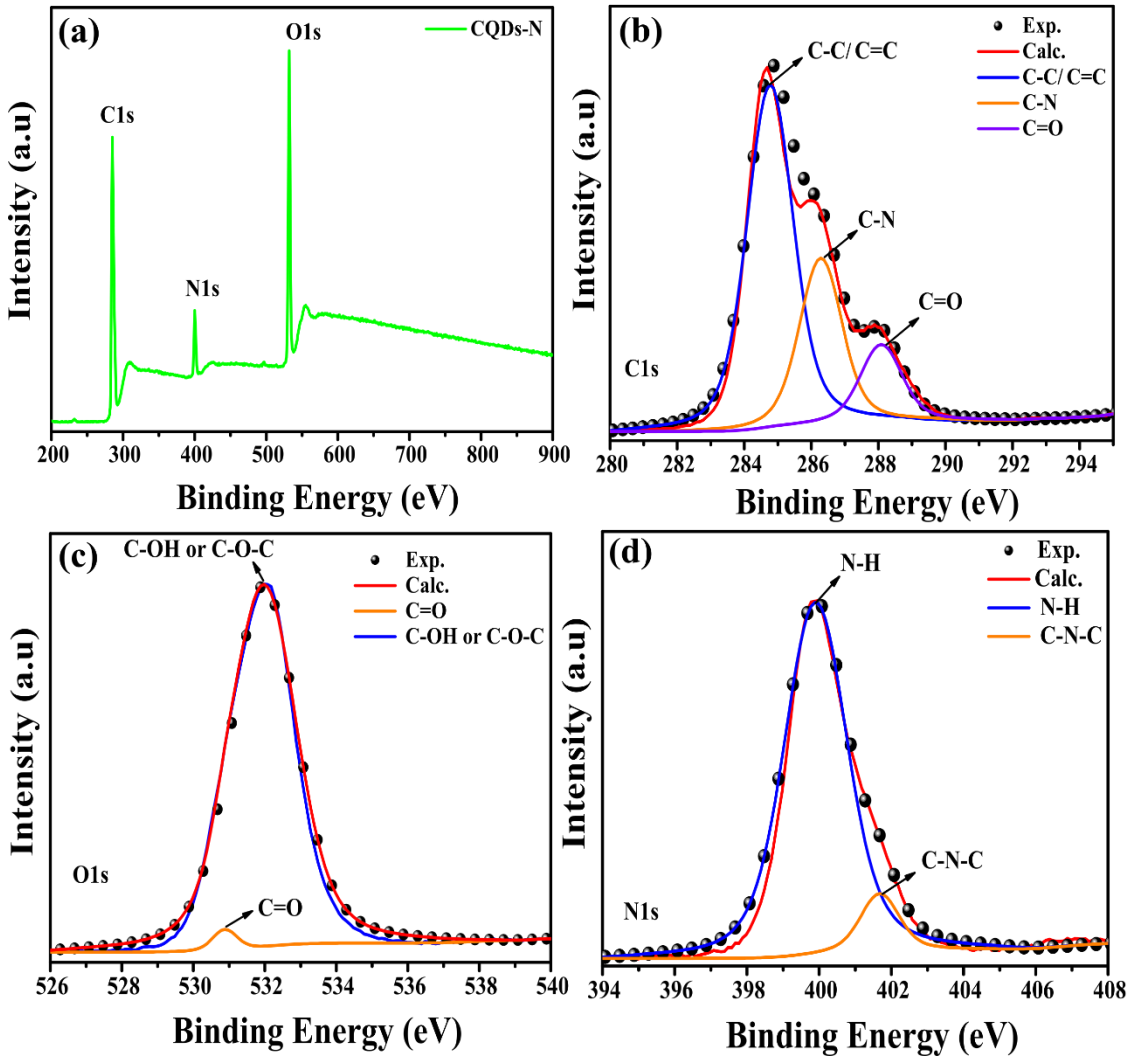

Source: author

As depicted in Figure 10a, the XPS spectrum CQD-P exhibits three obvious elemental signals, predominant C1s peak at 288.86 eV, O1s peak at 533.96 eV and P2p peak located 135.4 eV.

Figure 10- (a) XPS survey, (b) high-resolution XPS of C1s, (c) high-resolution XPS of O1s and (d) high-resolution XPS of P2s spectra of the CQD-P.

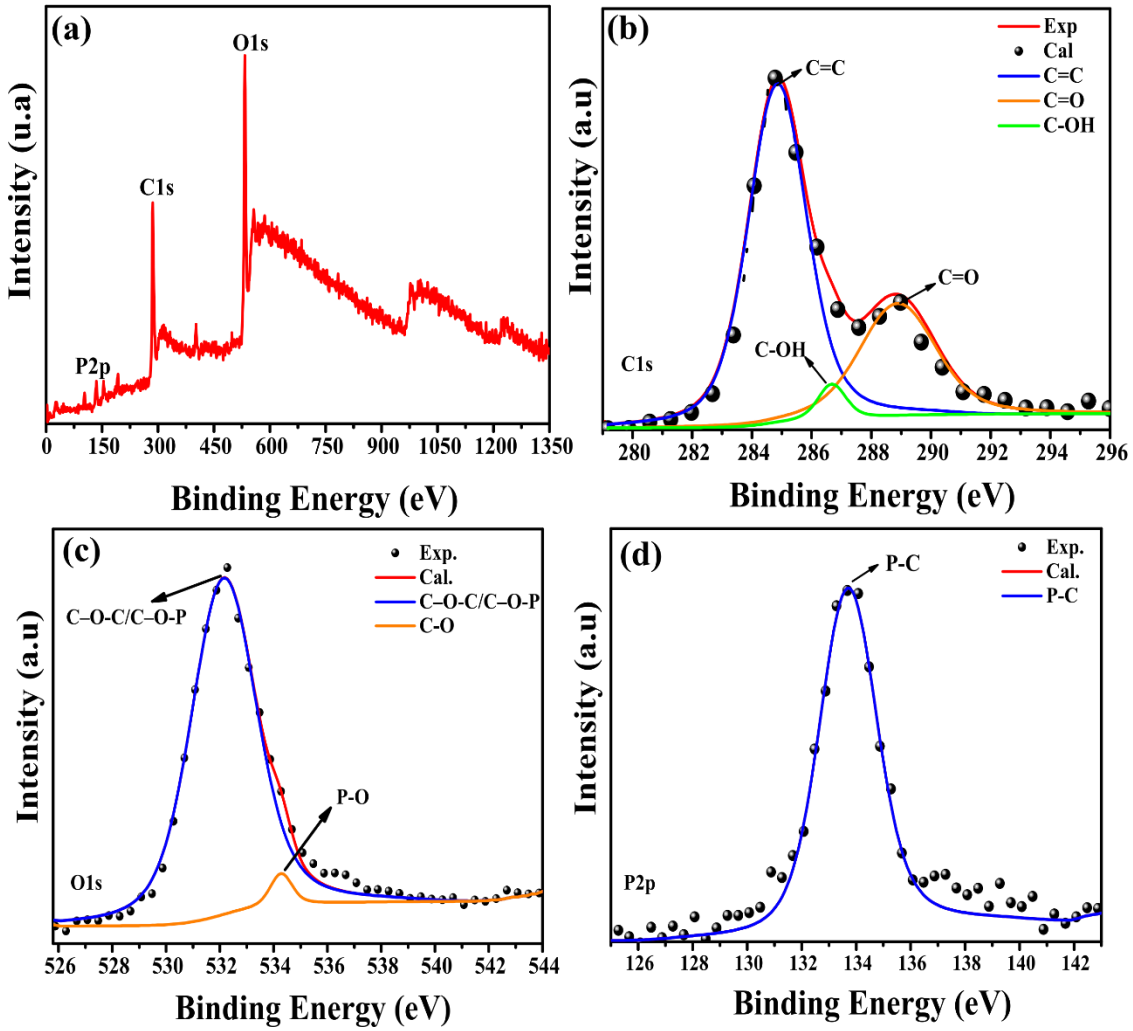

Source: author

The elemental analysis shows the composition as C 17.36 %, P 2.51 %, O 10.65 %. In particular, the deconvolution XPS range of carbon (1s) (Figure 10b) indicates three peaks at 284.8, 286.6, 289.0 eV, which are assigned to the C–C, C–OH, and C=O groups, respectively. In addition, the deconvoluted spectrum of oxygen (1s) is split into two peaks, at 532.1, and 534.3 eV (Figure. 10c) which are assigned the C-O and C-O–P groups, respectively (CHANDRA et al., 2016; ZHI et al., 2018; ZHOU et al., 2014). Similarly, The P2p short scan after deconvulation shows peak at 133.7 eV corresponding to the presence P–C (fig. 11d) (BHATI, 2019; FU et al., 2018).

The Figure 11a displays the XPS survey spectrum of the CQD-S, which shown O1s, C1s and S2s peaks at about 534, 285 and 164 eV.

Figure 11- (a) XPS survey, (b) high-resolution XPS of C1s, (b) high-resolution XPS of O1s, and (b) high-resolution XPS of S2p spectra of the CQD-S.

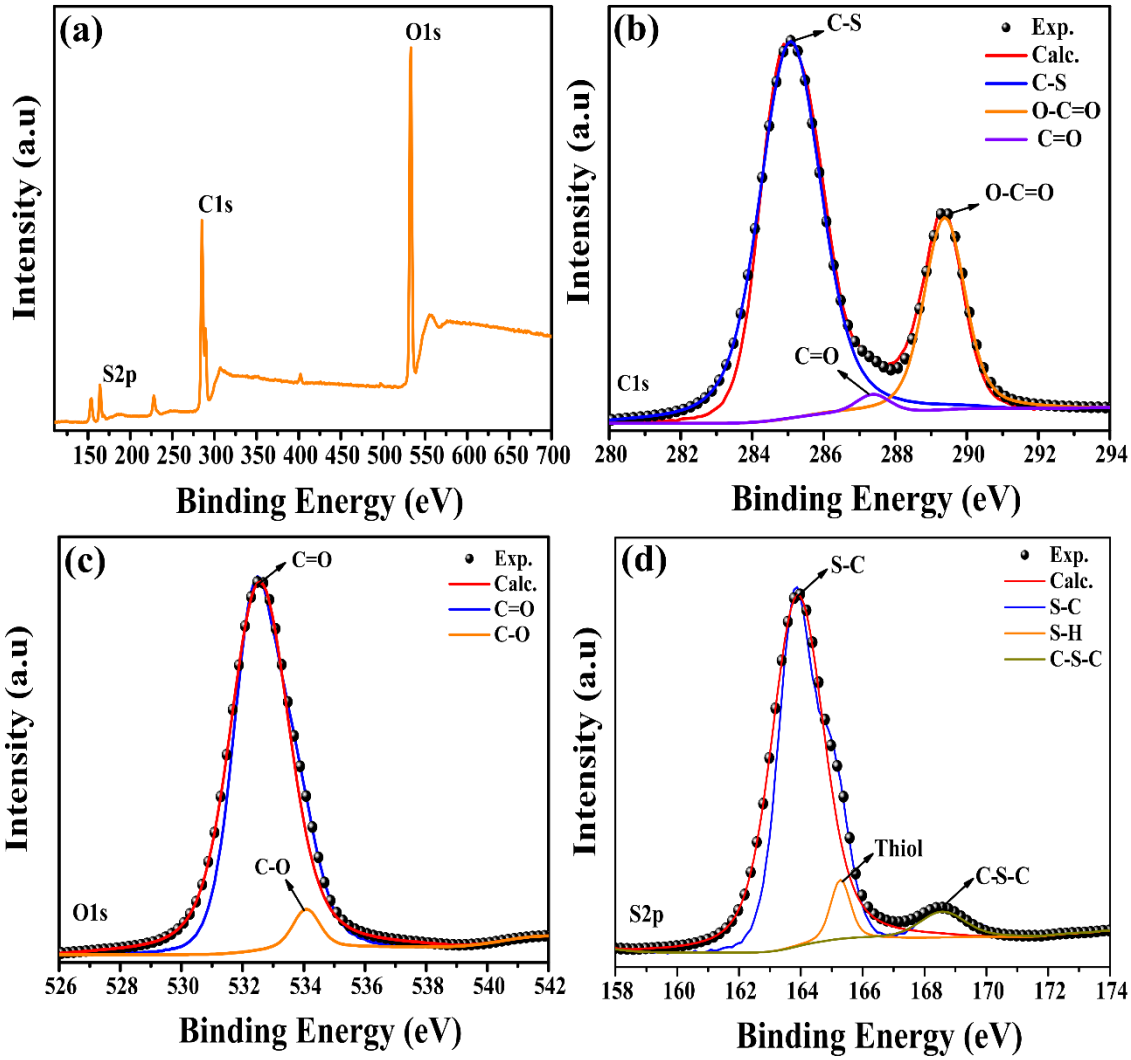

Source: author

The elemental analysis shows the composition as C 51.87 %, S 4.22%, O 31.11%. The high resolution XPS the C1s (Figure 11b) can be deconvoluted into a dominated componente for C-S at 285 eV, along with other bands associated with O-C=O at 287.3 eV and C=O at 289.4 eV, respectively (SONG et al., 2018; WU et al., 2019). Deconvolution of the O1s peak (Figure 11c) shows two components at 532.5 and 534eV for C=O and C-O, respectively (BAI, 2019; WANG et al., 2019; ZHANG; ZHANG; TANG, 2019). All of the S2p XPS spectra (Figure 11d) can be deconvoluted into three peaks, which correspond to S-C bonds at around 164 eV, S-H bonds at 165.3 eV and C-S-C bonds at 168.6 eV (JU et al., 2019; QU et al., 2019; RAFI, 2019; WEI et al., 2019; ZHAO et al., 2019).

In addition, more structural information on the CQD samples was obtained from FTIR spectra, which are presented in Figure 12 and revealed the presence of characteristic surface chemical groups of CQDs.

The spectrum CQD-OH show broad absorption features at around 3500 cm^{-1}, confirming the presence of hydroxyl groups (−OH). The 2930 cm^{-1} peak is the alkyl stretch, the main component of the carbon network. Strong signal at 1731 cm^{-1} is associated with C=O stretching vibrations and reveal several carbonyl and carboxyl functionalities, the peaks at 1586 cm^{-1} stretch of C=C bond indicating skeletal vibration of aromatic rings.

In addition, the peaks at 1386 cm^{-1} assigned to bending mode of C-O (PENG et al., 2012; SCHNEIDER et al., 2017). The CQD-N (Figure 12) spectrum contain broad bands around 3.268 cm^{-1} and 3405 cm^{-1} are attributed to the stretching frequencies of N-H and O-H bonds, respectively. There is also stretching and bending vibrations of methylene ($-CH_2$) groups at 2918 cm^{-1}. The stretching vibrations bands at 1709, 1642 and 1553 cm^{-1} are assigned to C=O, C=C and C=N. The bands around 1405 cm^{-1} is ascribed to C-N bond stretching. The bands around 1179 cm^{-1} maybe assigned C-O (JIA et al., 2019; KIM, 2019). Moreover, The FTIR spectrum of CQD-P (Figure 12), is observed peak at 1088 cm^{-1} is ascribed, P-O-C in aromatic and peaks at 970 cm^{-1} is associated P-OH (DONG, 2016a; FU et al., 2018). The FTIR spectrum CQD-S (Figure 12) it can be observed that there is an obvious band at 2431cm^{-1} was attributed to the –SH vibrations and the broad band at 1320 cm^{-1} were due to the stretching vibrations C-S-C bond, which indicated the sulfur have been doped to the CQD-S (CHENG et al., 2019; DAI et al., 2017).

Figure 12- FT-IR spectra of CQD-OH, CQD-N, CQD-P, CQD-S and Citric Acid (CA).

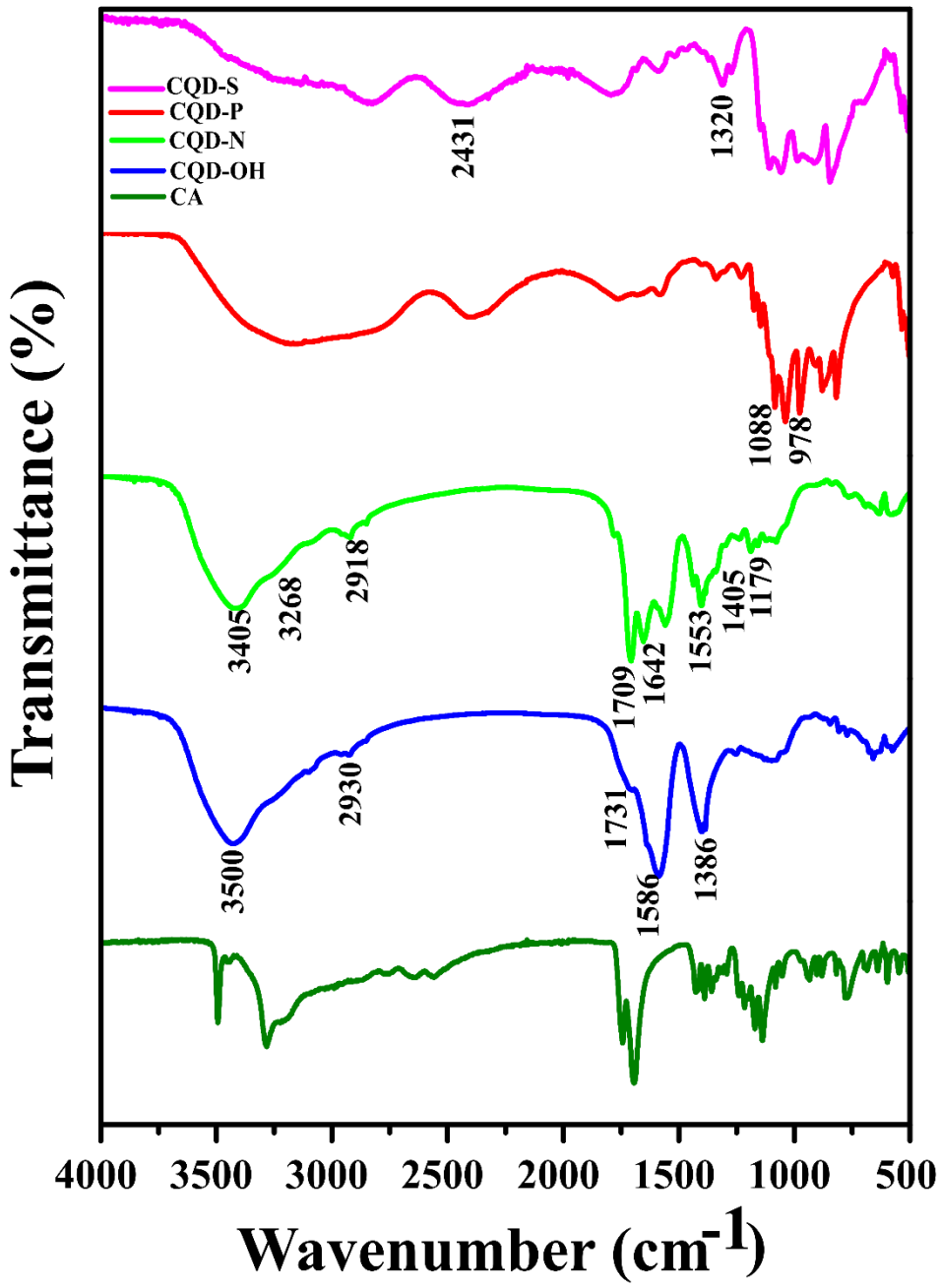

Source: author

The CQDs XPS spectra demonstrate the presence of carboxylic, amine, thiol and phosphate groups on the surface of the CQDs, indicating the successful incidence of N, P and S in the CQDs, as indicated by the FTIR results. Thus, it was possible to suggest what the structure of the synthesized CQDs would be like, as observed in Figure 13.

Figure 13- Suggested chemical structure for CQDs: (a) CQD-OH, (b) CQD-N, (c) CQD-P and (d) CQD-S.

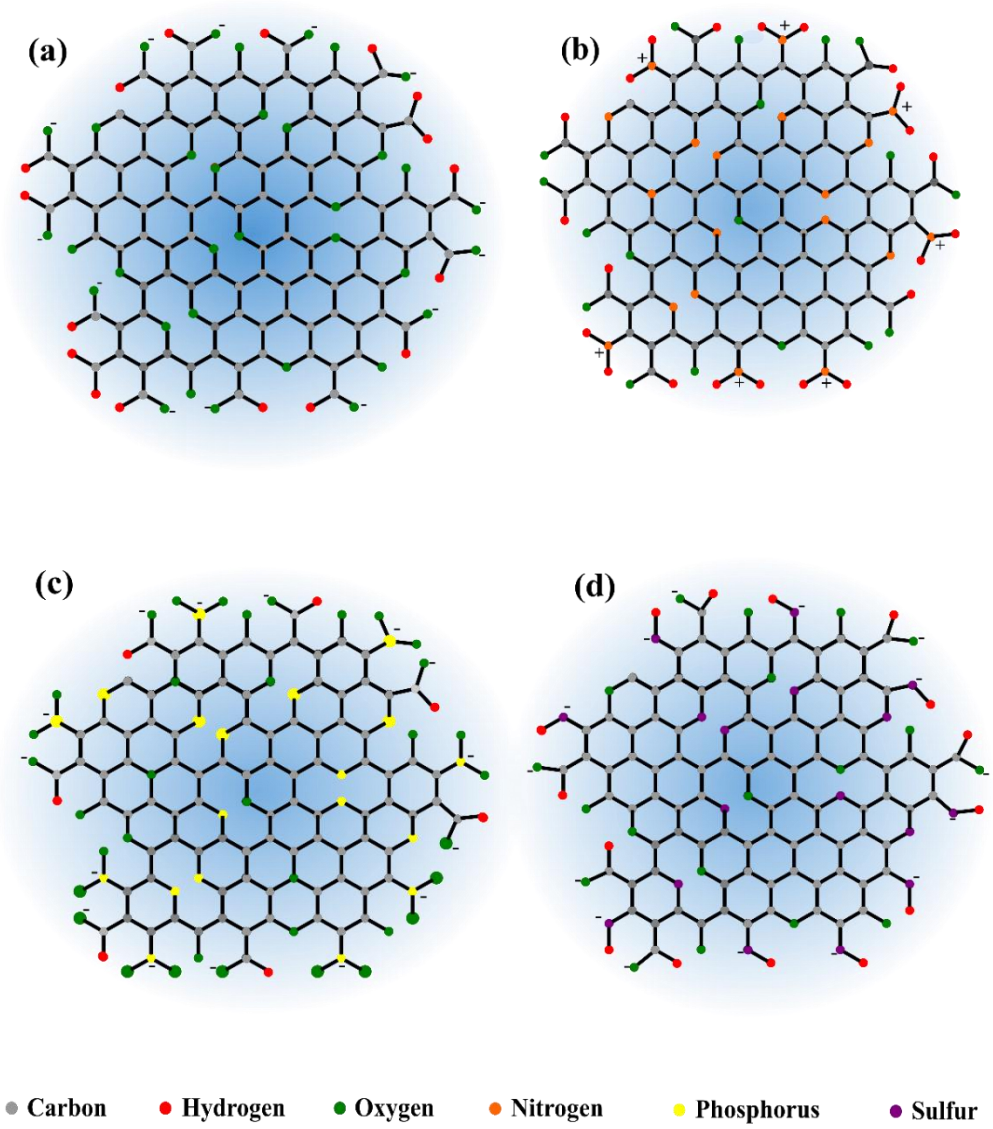

Source: author

1.6.3 Morphology properties of CQDs.

The morphology of CQDs was characterized by atomic force microscopy (AFM). Figure 14 depicts the AFM image of CQDs samples. The results in Figure 14 a, b, c and d showed that possessed of quasis-spherical morphologies.

Figure 14- Height AFM images (a, b, c and d) of the CQD-OH, CQD-N, CQD-P and CQD-S.

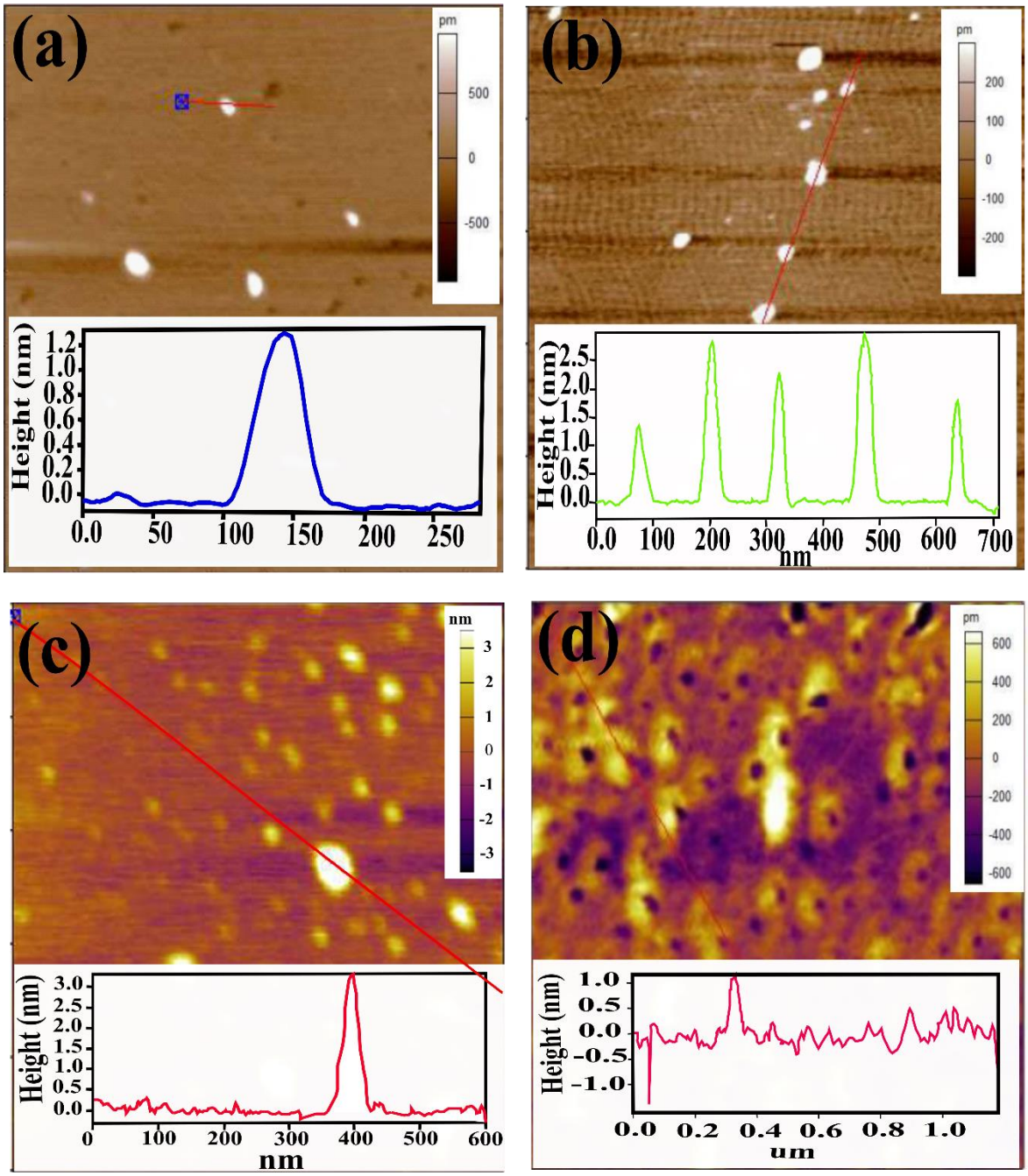

Source: author

The particle diameter of CQD-OH, CQD-P and CQD-s was distributed in the range of 1–3 nm (Figure 14a, c and d (inset))(NI et al., 2019; SHAMSIPUR et al., 2018). However, sample CQD-N in phase figure (Figure 14 b (inset)) show nanoparticles core-shell abaout 4 nm (SHI et al., 2019b). After the structural characterization of the doped CQDs, it was possible to observe that the N-doped CQDs obtained better quantum yield. However, the photoluminescent properties and analyzing the AFM, the CQD-N has an organized structure, almost without surface defects. Thus, in order to obtain CQDs in other emission ranges, N was chosen to dope

the new CQDs to be synthesized. However, changing the dopant precusor, the following are the characterizations of multicolor CQD.

1.7 Nitrogen doped Carbon dots (CQD) with intense multistate absorption and different luminescence emission.

1.7.1 Photoluminescence property of CQDs.

The CQD-$CONH_2$ prepared was doped with Nitrogen (N) by solvothermal route using CA and urea as C and N sources could assemble into N-rich nanoparticles and dimethylformamide (DMF) as the solvent, results in the production of abundant organic functional groups, such as C=O, C=N and COOH. These functional groups confer the CQDs with excellent dispersibility in diverse solventes (tetrahydrofuran, acetone, dimethylformamide, ethanol, metanol and water), intense visible absorptions and blue, yellow, red full color emissions (CHEN et al., 2016).

Figure 15- (a) UV-Vis spectrum of CQD-$CONH_2$ (b) Emission spectrum of CQD-$CONH_2$ for varying excitation wavelengths.

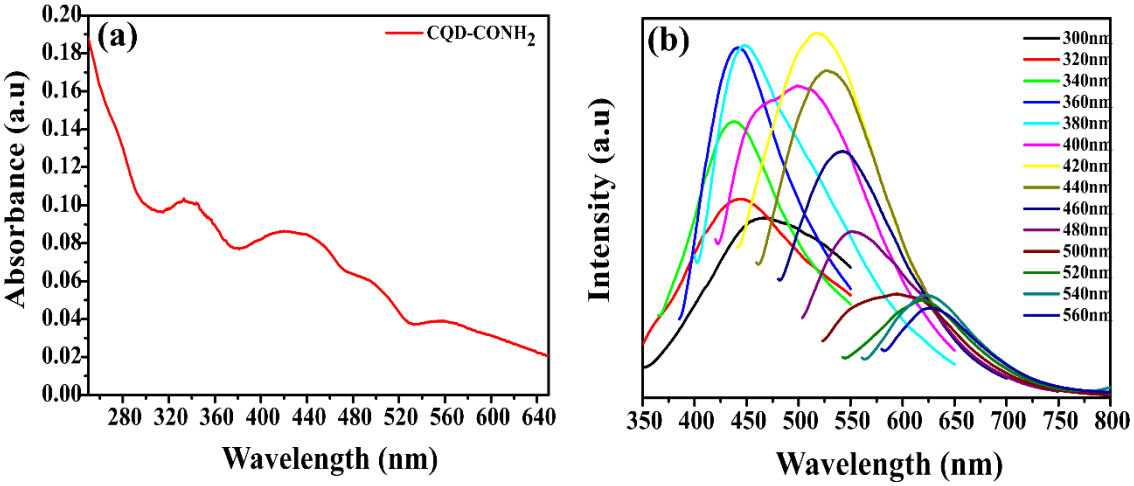

Source: author

As revealed by the UV-Visible absorption spectra (Figure 15 a), four strong absorption bands centered at 335, 431, 510 and 561 nm are attributed to the to the π-π* (HOMO-LUMO) transition of C=C bonds of the sp^2 C domain in the sp^3 C matrix n-π* transitions of C=O and C=N bonds, respectively, as well as the transitions from the n states to defect states on the surfaces of the CQD. Therefore, N doping will induce N-related defect states located in

the gap between the HOMO and LUMO. As a result, shifting of the photoluminescence band into red light region will occur when the electrons in N-related defect states return to the HOMO (OTYEPKA; ZBOR, 2017; ZHANG et al., 2017). The spectrum photoluminescence (Figure 15b) shown Strong emission in 448 nm, 520 nm and 620 nm, blue, yellow and red regions, when excited in 360 nm, 420 nm and 520 nm with quantum yields (QYs) for these blue was determined to be 6.02%. All these results indicate that this CQD sample possess both multistate absorption and emission features, which contribute to the variation in the emission spectra (SHAMSIPUR; BARATI; KARAMI, 2017).

1.7.2 Structural and morphology- properties of CQDs.

The raman spectra (Figure 16a) were utilized to characterize the intrinsic structure of the CQDs. Common features were observed in the 1000–2000 cm^{-1} region, where the G band (E_{2g} mode) at 1590 cm^{-1} can be related to the vibration of sp^2-bonded carbon atoms in a two-dimensional (2D) hexagonal lattice. The D band (A_{1g} mode) centered at 1386 cm^{-1} mainly arises from disordered sp^3 carbon atoms. Moreover, the I_D/I_G ratio can be used to evidence structural features since the D-band intensity can be associated to the extent of defects in the NPs. For the CQDs synthesized, the I_D/I_G ratio was found to be ∼1.62, indicates the existence of disorder structures or defects in the carbon quantum dots.

Figure 16b shown, all the FT-IR spectrum of CQD-$CONH_2$ demonstrate absorption bands around 3325 cm-^{1}, which correspond N-H groups in amide, the bands 3173 cm^{-1} attributed to O-H stretching vibrations. The bands at 2780 and 2922 cm^{-1} ascribed to –C-H bonds in aldehydes and –C-H in aliphatic groups $–CH_2$ and $–CH_3$, respectively. In addition, stretching vibrations of C=C (1594 cm^{-1}) attibued domains aromatic, C-N(1368 cm^{-1}), C-O(1117 cm^{-1}) attribued ether groups, C-N (1188 cm^{-1}), aliphatic groups and C=O (1714 cm^{-1}) carboxilic group (WANG, 2018; ZHU et al., 2018b).

Figure 16- (a) Raman spectra of as prepared CQD-$CONH_2$. (B) FT-IR spectra of CQD-$CONH_2$ (c) XPS survey, (d, e and f) high-resolution XPS of C1s, O1s and N1s spectra of the CQD-$CONH_2$.

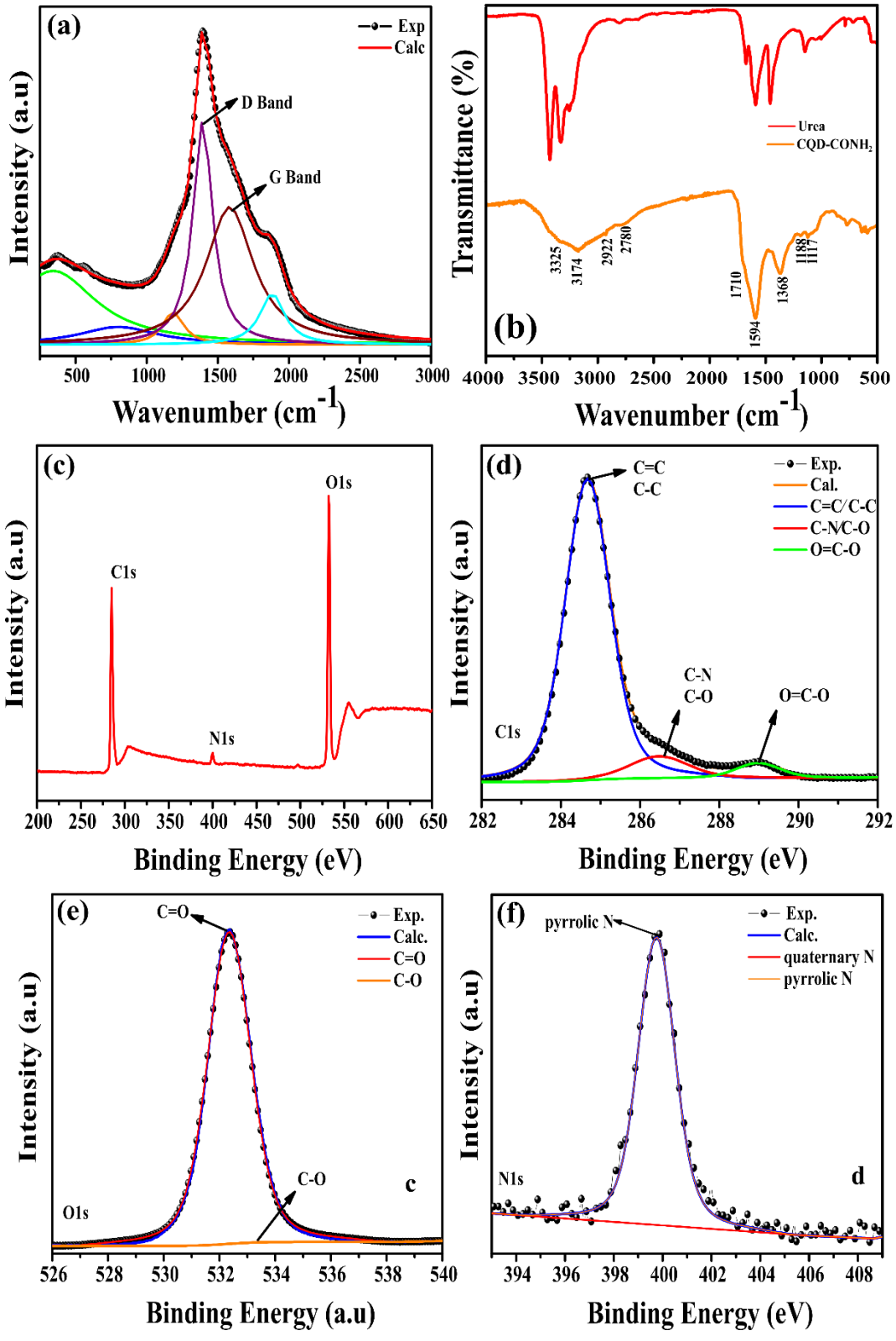

Source: author

The analysis X-ray photoelectron spectroscopy (XPS) shown compositions of the C1s, N1s and O1s peaks at about 284 eV, 400 eV and 532 eV, respectively, are observed in the XPS full survey spectra (Figure16 c). The XPS elemental analysis shows the composition of CQD-$CONH_2$ as C 60.98 %, N 2.47 %, O 36.55 %. The C1s band can be mainly deconvoluted into two peaks (Figure 16d), which represent graphitic sp^2 carbons (C=C/C–C, 284.6 eV) and carbonyl carbons (C=O, 286.5 eV). The O1s band can be resolved into two peaks (Figure 16e), which are assigned to C=O (532.3 eV) and C–O (533.4 eV). The N1s band can be fitted into two Gaussian peaks (Figure 16f), which correspond to pyrrolic N (399.5 eV) and quaternary N (401.2 eV). Obviously, the relative amount of pyrrolic N is bigger than quaternary N (CHEN et al., 2016). AFM image (Figure 17a) indicates that these CQDs are monodispersed, quase-espherical with a height of about 1–3nm (Figure 17a (inset)) (ZHENG; XIE, 2019).

Figure 17- (a) Height AFM images of the CQD-$CONH_2$, Heigth of CQDs (inset) and (b) Suggested chemical structure for CQD-$CONH_2$.

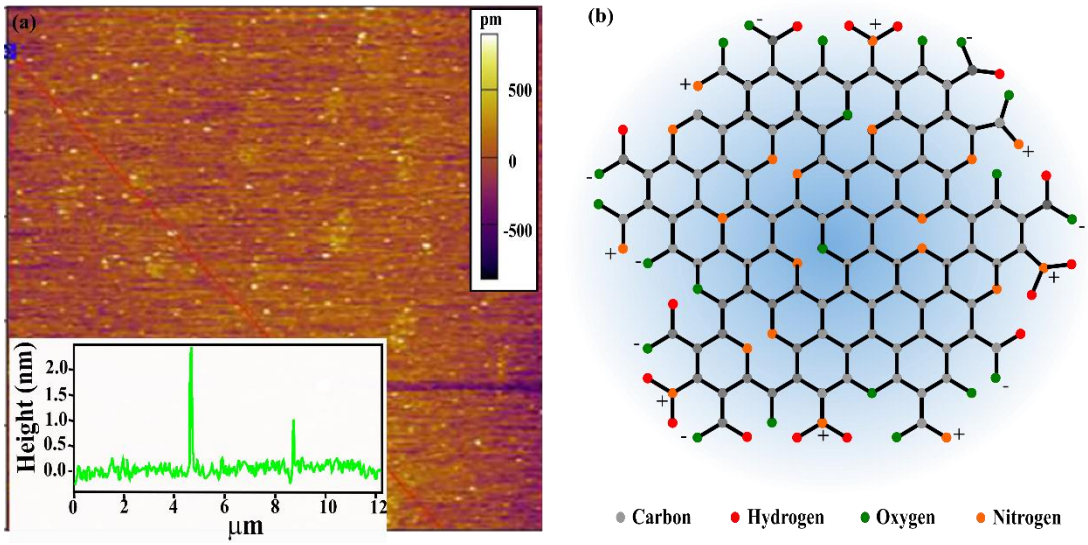

Source: author

In summary, N-doped CQDs were prepared by an easy solothermal route using CA as source C, urea as N source and DMF as solvent. These CQDs exhibit visible absorption in various states and blue, yellow and red color emissions under excitation wavelengths of 360 nm, 420 nm and 560 nm, respectively. XPS, FTIR and Raman spectra observations confirm that these three emissions originate from three different emitting states, that is, sp^2-related defect states C, C=O and C=N, respectively, on the surfaces of the CQDs. From these results it was possible to propose a chemical structure for CQD-$CONH_2$, as shown in Figure 17d. The doped

and non-doped CQDs have abundant oxygen-nitrogen functional groups, which give them the ability to combine with various analytes. Through the internal fluorescence filter effect (IFE) or electron, energy transfer effect, the fluorescence intensity of CQDs changes quantitatively.

1.8 CONCLUSION

Given the above, it can be inferred that thermolysis and solvothermal routes are viable alternatives for synthesizing CQDs using citric acid. In addition, N, P and S CQDs doping study was performed. The FTIR and XPS techniques confirmed the presence of functional (carbolic, amine, amide, thiols and phospate) groups on the surface of the CQDs. Raman spectroscopy evidenced the chemical structure of CQDs. Through AFM it was possible to determine the size of CQDs in the 1-4nm range. The CQD obtained with the best quantum yield was N-doped around 22%. N-doped CQD with multiple emission state was also obtained.

2. CARBOHYDRATES IDENTIFICATION BASED ON CARBON QUANTUM DOTS AND THE LECTIN FROM Canavalia Brasiliensis (ConBr).

2.1 INTRODUCTION

The carbohydrates present on cell surfaces play an important role in a wide range of biological and pathological processes like the interaction between cells and their environment, inflammations and cancer metastasis. In addition, carbohydrates are commonly used as biomarkers of pathological changes occurring during several diseases (ABREU et al., 2017). However, conventional procedures for the analysis of glycoproteins, for example high performance liquid chromatography (HPLC), capillary electrophoresis (CE), mass spectrometry (MS) or their combinations, require prior release of the glycans bound to their central proteins. Furthermore, due to the lack of adequate UV absorption in the released glycans, they are generally fluorescently labeled for the purpose of improved HPLC detection and separation and improved ionization efficiency in MS. For these reasons, the identification process is complicated (HIRABAYASHI, 2008). Therefore, it is necessary to develop an easy, fast and cost-effective methodology. An alternative to detecting glycans is sensor arrays.

2.2. Sensors arrays

Sensor array is known as the chemical nose/tongue approach, in which each analyte-sensor interaction will generate a specific response pattern coupled with statistical treatments form a potential technology for the success of analyte discrimination(CAO et al., 2020). The array sensor is a relatively fast technique for quantitative and qualitative analysis with low cost chemical sensors, recently used for determinations of heavy metals (ZHANG et al., 2020b), peptide (JING et al., 2017), monitoring of microbial processes(YOUSEFI-DARANI et al., 2020), and others.

The multisensor system inspired by human taste and olfactory strategies, consists of array of chemical sensors with low selectivity coupled with multivariate data processing tools. The chemical sensors differ in selectivity and sensitivity in relation to the different analytes producing unique response patterns for each target, where multidimensional information is generated from patterns-response and pattern recognition (Figure 18), provided by the treatment using chemometric tools in the intelligent recognition of targets present in the mixtures.(GEANĂ et al., 2020)·(CHEN et al., 2020a).

Figure 18 – Scheme of sensing strategy of sensor array in-brief.

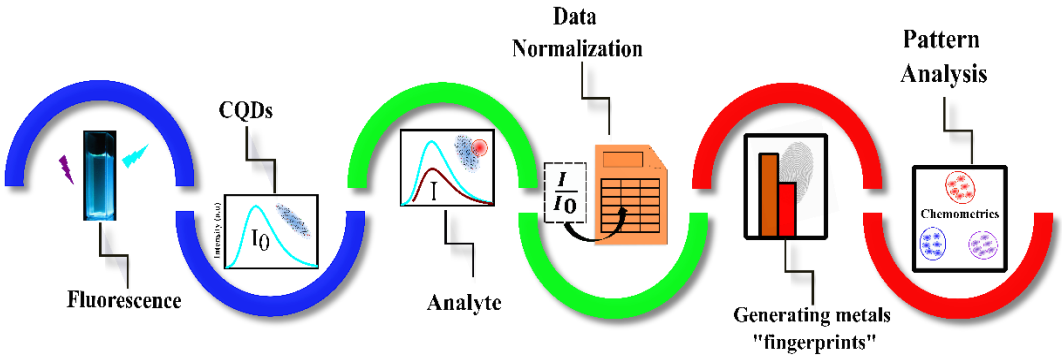

Source: Author.

Some nanomaterials are used in the production of sensors such as nanofibers, nanoparticles, microspheres, nanoplates(HU et al., 2021), also including materials such as gold nanoparticles, complexes based on lanthanides, graphene and carbon quantum dots (CHEN et al., 2020c).

The sensitivity and ability to discriminate analytes in sensor array of CQD are strongly related to the different sensor elements, promoting a necessary searching for advanced materials that neither post-modification or conjugations are needed. Such sensors act extensively and can be prepared on a large scale and with specific recognition properties (WANG et al., 2017). Sometimes more complex materials are needed for a more robust sensor array, as reported by Ma and colleagues using CQDs and silver nanoclusters to detect dopamine and glutathione with multichannel matrix through a lab on a electrochemical chip device using biological samples(MA et al., 2020b). 1.2.1 Methods of data preprocessing

To explore the full range of instrumental data, there are some algorithms of multivariate techniques for processing and modeling spectroscopic data (ELSONBATY et al., 2020). The information presented in fluorescence spectra, for example, consists of variables with great influence on the compound under study. In addition, noisy or irrelevant variables can also be found. Chemometric analysis plays an important role in preventing any incompetence resulting from these variables or presence of interferences (DHAULANIYA et al., 2020; PINTO; STECHI; BREITKREITZ, 2019). Therefore, different preprocessing methods are applied in order to improve the performance of mathematical models. This procedure is relevant in optical analysis once reduces the interference from light scattering (LENG et al., 2020). This treatment is relevant for data from absorption spectra in the ultraviolet and visible (UV-Vis), fluorescence, near infrared (NIR) and Raman (CAMPOS; REIS, 2020). Figure 19 summarizes

the main methods of data preprocessing, which it will be further described in this section.

Figure 19 – Preprocessing of data for multivariate analysis.

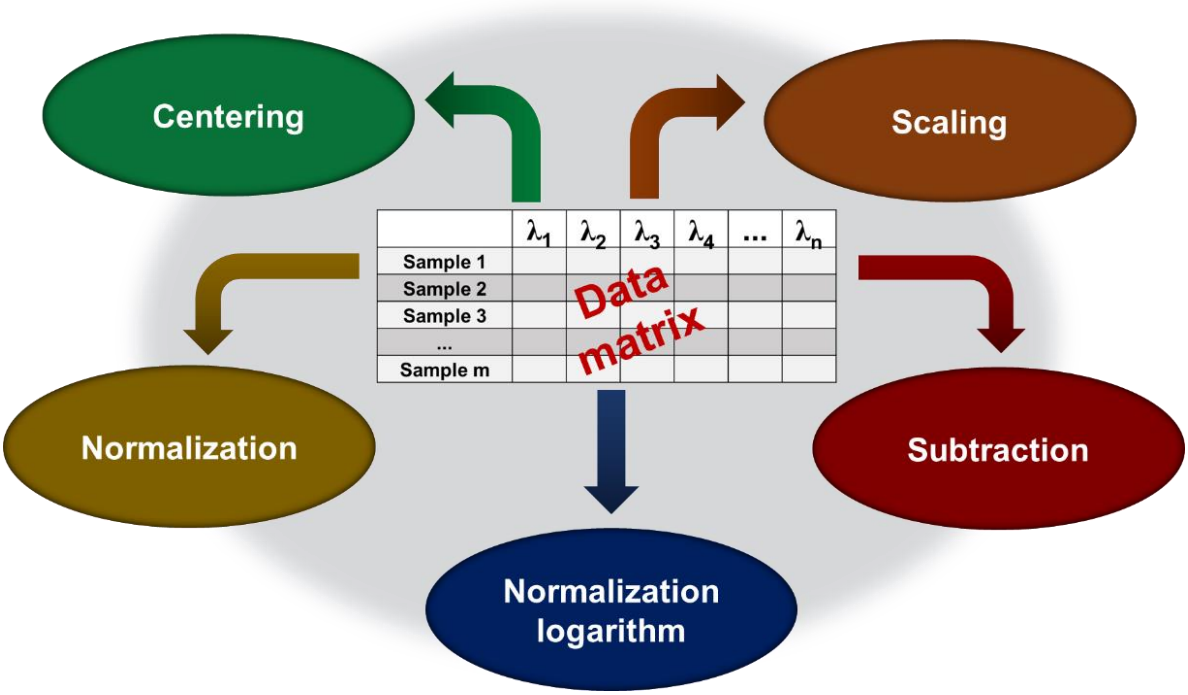

Source: (CRUZ et al., 2021)

The normalization is a pretreatment that divides each spectrum by an estimation of its spectral intensity. This can be done using the following properties: area (area normalization), maximal peak (maximum normalization), a specific spectral point (peak normalization), length (unit vector normalization), or the sum of the spectral values (CAMPOS; REIS, 2020). Normalization is very efficient, essential to allow the use of the linear tools of chemometrics (RABATEL et al., 2020). In sensing strategies based on CQDs, normalization can be applied by ratio between the fluorescence intensity value after addition of the analyte (I) and the fluorescence signal obtained from CQDs only (I_0). These values can be obtained for the entire analyzed spectral range. This means that if a scan is performed from 380 to 600 nm, with data intervals of 1 nm, 220 values of I/I_0 ration will be recording. For example, Freire *et al* used fluorescence normalized data (ratio I/I_0) for identification of proteins for chemometric tools (FREIRE et al., 2018). Figure 20 schematically illustrates the procedure that can be performed to normalize the data before applying chemometric identification and quantification tools.

Figure 20 – General procedure for treatment of full set data by normalization. In this example, the wavelengths were used as independent variable in a data interval of 20 nm.

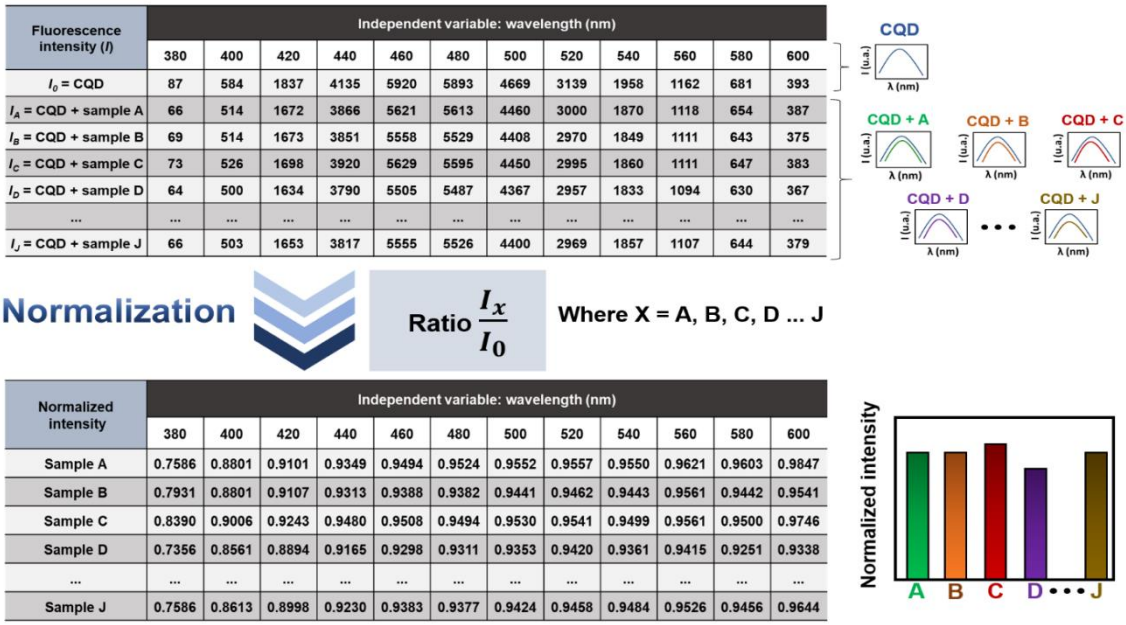

Fluorescence intensity (I)	Independent variable: wavelength (nm)											
	380	400	420	440	460	480	500	520	540	560	580	600
I_0 = CQD	87	584	1837	4135	5920	5893	4669	3139	1958	1162	681	393
I_A = CQD + sample A	66	514	1672	3866	5621	5613	4460	3000	1870	1118	654	387
I_B = CQD + sample B	69	514	1673	3851	5558	5529	4408	2970	1849	1111	643	375
I_C = CQD + sample C	73	526	1698	3920	5629	5595	4450	2995	1860	1111	647	383
I_D = CQD + sample D	64	500	1634	3790	5505	5487	4367	2957	1833	1094	630	367
...	...	...	...	...	...	...	...	...	...	...	...	...
I_J = CQD + sample J	66	503	1653	3817	5555	5526	4400	2969	1857	1107	644	379

Normalized intensity	Independent variable: wavelength (nm)											
	380	400	420	440	460	480	500	520	540	560	580	600
Sample A	0.7586	0.8801	0.9101	0.9349	0.9494	0.9524	0.9552	0.9557	0.9550	0.9621	0.9603	0.9847
Sample B	0.7931	0.8801	0.9107	0.9313	0.9388	0.9382	0.9441	0.9462	0.9443	0.9561	0.9442	0.9541
Sample C	0.8390	0.9006	0.9243	0.9480	0.9508	0.9494	0.9530	0.9541	0.9499	0.9561	0.9500	0.9746
Sample D	0.7356	0.8561	0.8894	0.9165	0.9298	0.9311	0.9353	0.9420	0.9361	0.9415	0.9251	0.9338
...	...	...	...	...	...	...	...	...	...	...	...	...
Sample J	0.7586	0.8613	0.8998	0.9230	0.9383	0.9377	0.9424	0.9458	0.9484	0.9526	0.9456	0.9644

Source: (CRUZ et al., 2021)

Furthermore, we can also consider those that are pretreatment procedures to be applied for each column of the data matrix. This routine procedure is relevant in any chemometric analysis (FERREIRA, 2015). The two most used methods in multivariate analysis will be described in next section: centering and scaling. Briefly, centering the data results in the translation of the variables axes to the average value of each one, which the data structure is fully preserved (FERREIRA, 2015). Scaling is applicable to remove differences in magnitude between variables or samples, when all data set is used. For three-way data, scaling must be done on the rows of a matrix and not across the columns like in centering. For example, to remove differences in magnitude intensity between the emission wavelengths of a set of spectra, one can scale the three-way array within the emission mode. To do this, the three-way array has to be unfolded in such a way that emission wavelength is in the rows and then the rows are scaled. This is because all the columns, where the variable occurs, have to be scaled (MARTÍ; BALDRICH, 2015).

2.3 Exploratory data analysis and classification methods

The search for regularities has always been a challenge, principally in chemistry. For instance, Mendeleev developed the periodic table based on empirical data, i.e. building a

characteristic patterns (FERREIRA, 2015). In chemometrics, patterns can be recognized from component models. These methods aim to reduce the dimensionality of the data while retaining as much as possible information by summarizing the information in a set of low dimensional components. Component models can handle collinear data and missing values as those arising from throughput measurement techniques like NMR, Mass Spectroscopy and Fluorescence Spectroscopy (SACCENTI; CAMACHO, 2020).

Pattern recognition methods can be classified into unsupervised and supervised. Unsupervised methods do not use any prior information about classes. They are then said to provide neutral (unguided) information that will help to understand the differentiation between analytes in a complex system. These methods are also known as multivariate statistical analysis exploratory of data. Some examples of these methods are Principal Component Analysis (PCA) and Hierarchical Cluster Analysis (HCA)(MESSAI et al., 2016). Sun and colleagues developed a multi-channel sensor based on carbon dots-metal ions ensembles to discriminate phosphate anions. As shown in Figure 21, the authors used PCA and HCA once CQDs showed excellent capabilities for the detection of phosphate anions. Furthermore, the proposed sensor array was validated by the successful identification of phosphate species in serum. This system manifested numerous advantages, such as simple fabrication process and flexible adjusting detection ranges (SUN et al., 2017a).

Figure 21 – (a) Principal component analysis (PCA) and (b) hierarchical cluster analysis (HCA) plots for the discrimination of five phosphate anions (all at 10 μM) in the presence of fetal bovine serum based on the PL signal changes of the as-developed triple-channel sensor array (SUN et al., 2017a).

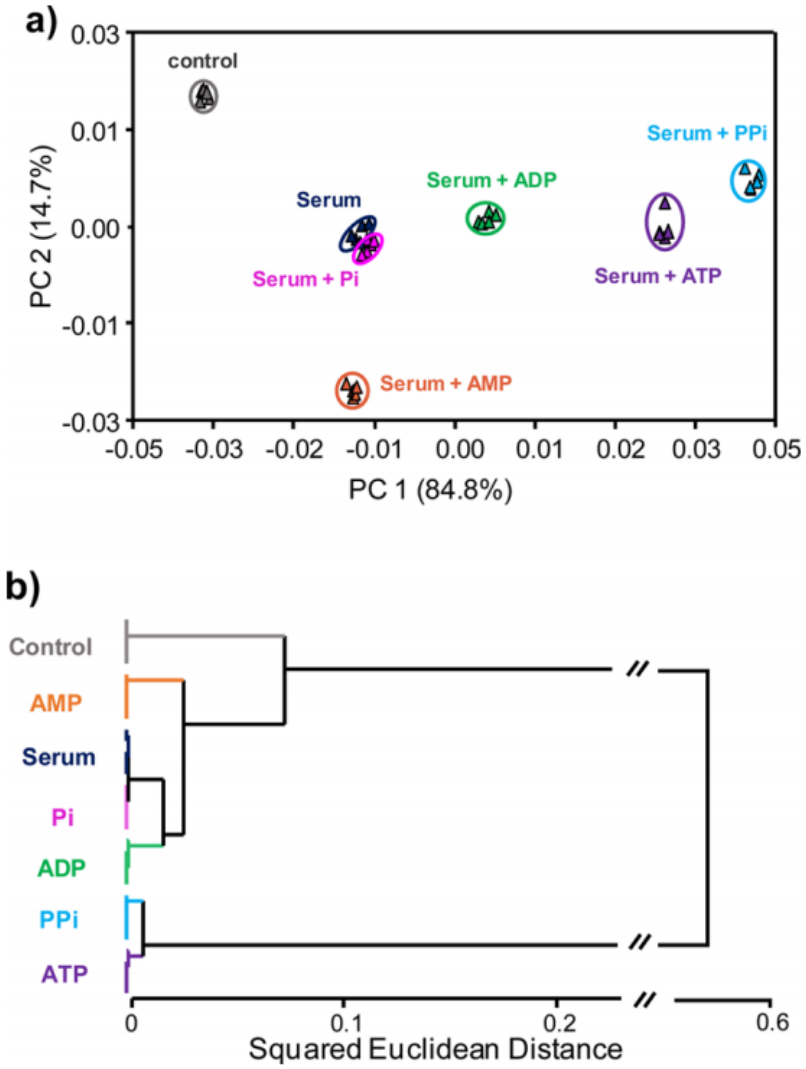

Source: Reprinted with permission from Sun et al (2017). Copyright (2020) American Chemical Society.

Supervised methods (classification methods), in turn, are defined by two sets of data called objects (inputs) and classes (target). These methods aim to discover the relationship between objects and classes, where a mathematical model is constructed. For this, in supervised methods, it is necessary to know the classes previously. This information represents the set of features that define the classification process. Linear discriminant analysis (LDA), Soft Independent Modelling of Class Analogies (SIMCA), and K-Nearest Neighbors (KNN) are examples of supervised method of pattern recognition (MONCAYO et al., 2015). The Figure

22 lists the main methods of exploratory data analysis and classification methods. It is important to noticed that in both methods, mathematical algorithms include two different approaches. Then, the models can be classified as linear and non-linear. Linear chemometric methods use linear combination of variables to estimate the classification model; whereas non-linear methods apply more complex algorithms, increasing the sophistication and the classification capacity of the method (MONCAYO et al., 2015).

Figure 23 – Exploratory data and classification methods as chemometric tools applied in sensing strategies: (A) example of score plot of PCA; (B) example of canonical factors plot of LDA.

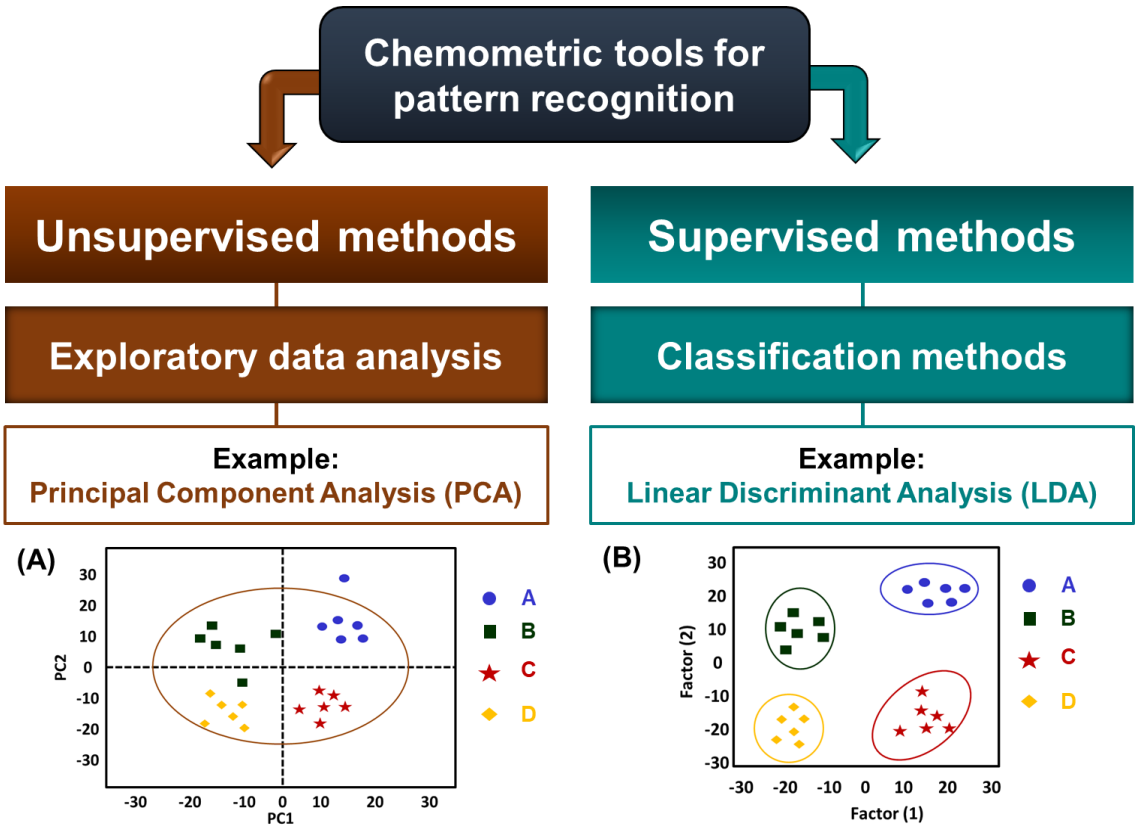

Source: (CRUZ et al., 2021)

2.3.1 Principal Components Analysis

Principal component analysis (PCA) is probably the most commonly used multivariate technique (HOTELLING, 1933; PEARSON, 1901) In PCA, the correlated original variables are transformed into sets of linearly uncorrelated variables called principal components. This procedure reduces dimensionality of data with a minimum loss of

information (KEERTHI VASAN; SURENDIRAN, 2016). Given an *n x p* data matrix ***X***, the PCA model follows the Equation **(5)**:

$$\boldsymbol{X} = \boldsymbol{T_K P_K^T} + \boldsymbol{E_K} \quad (6)$$

Where $\boldsymbol{T_K}$ is the *n* x *K* score matrix containing the projection of the observations into the K-dimensional space defined by the first *K* principal components, $\boldsymbol{P_K}$ is the *p* x *K* matrix of the loadings, which are the coefficients of the linear combination of the original variables defining each principal component, and the *n* x *p* is the matrix $\boldsymbol{E_K}$ that contains statistic residuals (SACCENTI; CAMACHO, 2020).

In a typical PCA analysis, two results are generated, loadings and scores plots. The loading vectors describe the direction of the principal components in relation to the original variables, whereas the score vectors describe the direction of the principal components in relation to the observations. Therefore, the maximum amount of information is retained in the smallest number of dimensions (SUN et al., 2020). These dimensions are denominated Principal Components (PCs). To represent the projection of the data, two or three PCs that represent the maximum variance of the data are generally used, obtaining two or three-dimensional graphs, respectively. The first PC accounts for the maximal variation of data, while each successive PC does not correlate with the previous PCs and expresses as much of the remaining information as possible (WOLD; ESBENSEN; GELADI, 1987). PCA is a helpful data visualization technique: since each object gets a score value on each PC, objects can be presented in score plots. Score plots can reveal patterns, trends and outliers in the data (MONAKHOVA; GORYACHEVA, 2016).

Gao and co-workers developed a sensing platform using a single CQD-type and six different metal ions and successfully identify all of natural amino acids in bovine fetal serum samples. The response pattern (6 signals × 20 amino acids × 5 replicates) generated by the sensor array were statistically analyzed by PCA method. This statistical procedure converted a set of observations of possibly correlate variables into a set of values of linearly uncorrelated PCs. Then, the percentages of variance captured by PCs represent the projection of the original data information PC 1 and PC 2, accounting for more than 90% of the total variability, were taken as the horizontal and vertical coordinates to plot the PCA two-dimensional graph (GAO et al., 2019). All of the amino acids show a high level of data dispersion in the PCA score plot, which can be attributed to the high cross-reactivity given by the sensing system.

2.3.2 Linear Discriminant Analysis

When only the effective reduction or even most economical representation of high dimensional data is desired, the PCA is adequate. However, to determine a vector basis that best discriminates samples, Ronald A. Fisher proposed a criterion for maximizing the separation between two or more classes of samples that became known as Linear Discriminant Analysis (LDA) (BELHUMEUR; HESPANHA; KRIEGMAN, 1997), which it searches for a linear function of the variable in multivariate space. When the number of variables is larger than the number of observations in multi-dimensional data, the directly use of LDA is limited. In that case, first PCA is applied for data compression to transform the original variables into a reduced new set of variables (KUMAR et al., 2014). Then, LDA makes a discriminate function for each group according to the following equation:

$$\boldsymbol{F(G_i) = k_i + \sum_{j=1}^{n} w_{ij} p_{ij}} \quad (7)$$

Where i represents the number of groups (G), k_i is the constant of each group, n is the number of parameters used to classify a data set into a given group and w_j is the weight coefficient assigned by LDA to a selected parameter (p_i) (KUMAR et al., 2014).

LDA is an algorithm commonly applied in sensor array. Therefore, Xu and co-workers developed a facile one-step strategy to discriminate proteins at nanomolar concentration (XU et al., 2017a). In this work, multiple proteins could be well-identified without any overlap in the presence of human urine (Figure 24 (a)). Cruz *et al* used chemical-nose' strategy based on CQDs and metallic cations to discriminate proteins at concentration as low as 50 nmol L^{-1} (CARNEIRO CRUZ et al., 2019a). LDA plots were generated based on the fluorescence-responses obtained from interaction between CQDs, Cu^{2+}, Ni^{2+} ions and analytes. Carneiro *et al* used a similar strategy to identify pesticides in rice samples (Figure 24(b)). The analyzed pesticides were discriminated with 100% accuracy, using CQDs and functionalized silver nanoparticles (AgNPs) (CARNEIRO et al., 2019b). In this case, LDA also proved to be an efficient tool to detect pesticides in real samples, with a concentration as low as 250 ng mL^{-1}.

Figure 24 – (a) Canonical score plot for the discrimination of eight proteins in the presence of human urine by using CQD-based sensor array (XU et al., 2017a). (b) Canonical score plot obtained from LDA of real sample extracts using CQDs and silver nanoparticles(CARNEIRO et al., 2019b);

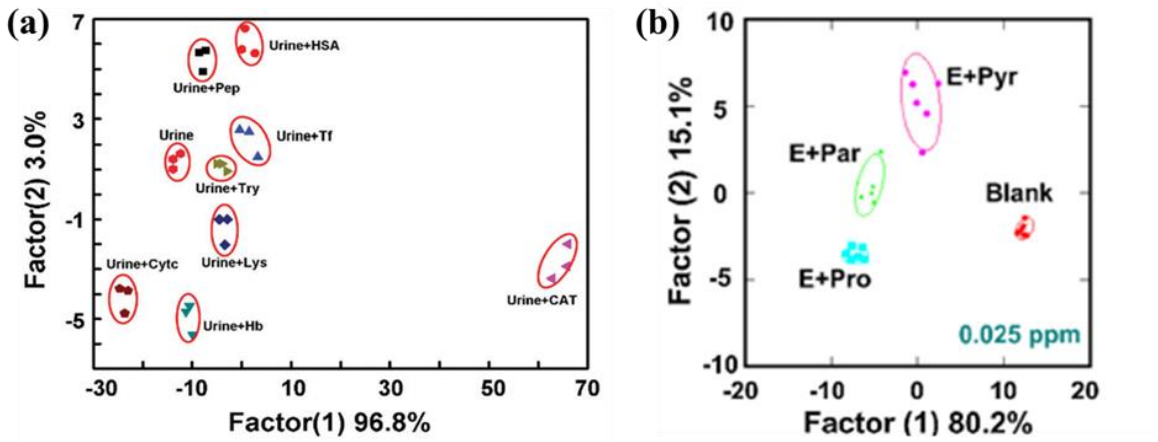

Source: (a) Republished with permission of Xu *et al* (2017); permission conveyed through Copyright Clearance Center, Inc.; (b)Reprinted from Carneiro *et al* (2019); Copyright (2020), with permission from Elsevier.

Thereby, fluorescence intensities of CQDs can be used as an analytical signal to determine several analytes. The advantages of fluorescence spectroscopy compared to other spectroscopic techniques include its “four S's”: sensitivity, simplicity, speed and selectivity (RAMAMURTHY; PONNUSAMY; CHELLAPPAN, 2019). Depending on the purpose, different methods can be applied in order to extract as much information as possible from the analyzed variables. In this context, the prediction of the presence or quantity of a certain compound in a sample can be obtained by appropriate chemometric tools (ALGETHAMI et al., 2020; GUIMARÃES et al., 2018).

PCA and LDA is a grouping technique in which point groups (or clusters) are created in a multidimensional space using some kind of distance metric. Thereby, three types of metric proximity measurements are used: Euclidean, Mahalanobis and Manhattam. In Eucludian distance it is an invariant measure, but it assumes equal covariance between classes, the problem related to this distance is the dependence with the scale change, however, it still being the most used metric proximity measurement. The Manhattan distance is a simplification of the Eucludian distance, known as the straight distance used to calculate the distance between pairs of samples. Nevertheless, Mahalanobis considers that the surfaces of each class are ellipsoids centered on the mean, and as the Mahalanobis distance is adimensional, it is also

called statistical or generalized distance. In addition, with respect to scale, it is considered to be univariant, very useful in the case of multivariate data since the caries are measured in different units(LI; ASKIM; SUSLICK, 2019).

2.3.3 ConBr lectins and carbohydrates

Lectins are proteins able to interact specifically and reversibly to carbohydrates, inside the lectins one can find *ConBr* (Figure 9a), a lectin extracted from *Canavalia brasiliensis* seeds, also known as Cow Bean, a native legume of Brazil and South America (WOLIN et al., 2021). A native legume of Brazil and South America is constituted of multimeric structures made up of identical monomers that contain 237 amino acids with approximately 25 kDa that exhibit a pH-dependent dimer or tetramer equilibrium. The union between amino acids is consolidated by non-covalent forces such as hydrogen bonds, hydrophobic and electrostatic interactions. Numerous studies have shown various biological actions of *ConBr* on different targets, including immune and nervous system cells(BATISTA et al., 2017; CANAVALIA, 2019; CAVADA et al., 2019). Besides, *ConBr* exerted antiproliferative effects on leukemia(FAHEINA-MARTINS et al., 2012) and melanoma cell lines (SILVA et al., 2014), even though the mechanisms involved in ConBr anticancer effects remain un-known. Prior studies from our group have also demonstratedantidepressant-like effects of ConBr on animal models, which seems to involve induction of Brain-derived neurotrophic fator (BDNF) expression *in vivo*, as well as neuroprotective responses of ConBr *in vivo* and *in vitro* (BARAUNA et al., 2017; JACQUES et al., 2013; RIEGER et al., 2014a, 2014b, 2017; RUSSI et al., 2012).

In addition, the monomer molecules have carbohydrates in their structure, being considered glycoproteins and metalloproteins, because have Ca^{2+} and Mn^{2+} ions in their structure, to stabilize the binding sites and fix the positions of amino acids that interact with the binding sugars. The calcium coordination fixes the side chains of the protein providing a more effective sugar binding, the cations stabilize the general architecture of the site, fixing the position of the structural elements. Thus, Mn^{2+} does not coordinate any residues that directly interact with the protein, but rather corrects the position of Ca^{2+} (CANAVALIA, 2019; SOUSA et al., 2019).

Carbohydrates are by far the most abundant organic molecules found in nature, and nearly all organisms synthesize and metabolize carbohydrates. The term carbohydrate arose

from the fact that most simple sugars have the empirical formula $C_nH_{2n}O_n$, where n is ≥ 3, suggesting that carbon atoms are in some way combined with water. However, the complex heterogeneity of carbohydrates in living systems is a direct result of several carbohydrate characteristics: the ability of different types and numbers of sugar residues to form glycosidic bonds with one another, the structural characteristics of these molecules, the type of anomeric linkage, the position and the absence or presence of branching. The Figure 25, shown estrutures three diferents carbohydrates.

Figure 25- (a) structure of *ConBr* lectin, (b) structure of glucose, (c) structure Methyl-α-D-mannopyranoside, (d) mannose carbohydrate.

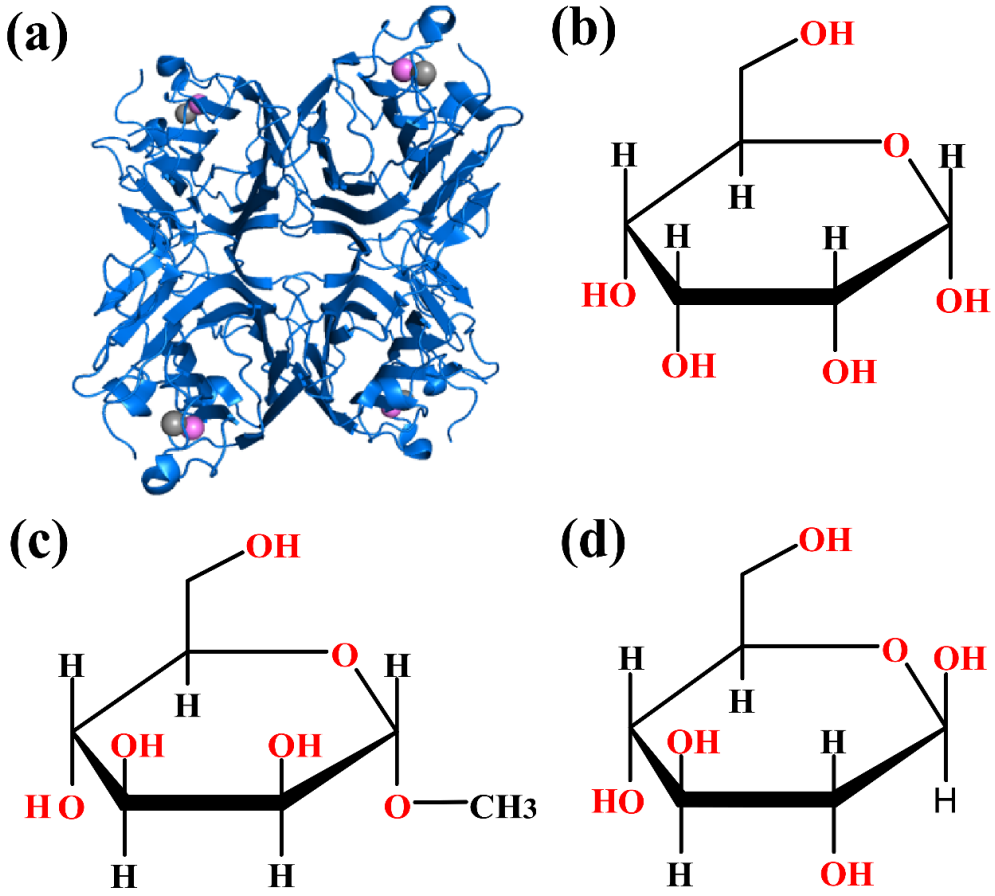

Source: Author

Glucose is a monosaccharide is one of the most important carbohydrates in biology. Cells use it as an energy source and metabolic intermediate, contain six carbon atoms and an

aldehyde group and are therefore referred to as an aldohexose. The glucose molecule can exist in an open (acyclic) and ring (cyclic) (equilibrium) form, the latter being the result of an intramolecular reaction between the aldehyde C atom and the C-5 hydroxyl group to form an intramolecular hemiacetal. In aqueous solution the two forms are in equilibrium, and at pH 7 the cyclic form is predominant.

Since the ring contains five carbon atoms and one oxygen atom, which is reminiscent of the pyran structure, the cyclic form of glucose is also referred to as glucopyranose. In this ring, each carbon is attached to a side hydroxyl group except for the fifth atom, which binds to the sixth carbon atom outside the ring, forming a CH_2OH group. D-Mannose is glucose isomer, differing only in the position of the hydroxyl group on the second carbono, in the case, the methyl-α-D-mannopironoside contain 7 carbon (HAIKE GHAZARIAN, BRIAN IDONI, 2012; ZHAO et al., 2008).

Herein, we proposed a sensing platform for carbohydrates based on sensor array. This nose-tongue system was designed using CQDs, which act as sensors to emit detection signals, combined with *ConBr* lectin which act as the system's receivers. This array sensor has as its initial proposal to discriminate three types of sugars: glucose, mannose and methyl-α-D-mannopyronoside.

2.4 OBJECTIVES

2.4.1 General

- To develop a sensing strategies by using different doped-CQDs to identify carbohydrates.

2.4.2 Specific

- To evaluate *Canavalia Brasiliensis* (ConBr) lectin interaction with synthesized with doped CQDs;
- To evaluate the interaction of carbohydrates directly with doped CQDs;
- To evaluate interaction ensemble CQD-doped-ConBr lectin with carbohydrates;
- To propose a single-channel carbohydrate sensing strategy using the CQD-doped-ConBr lectin suite based on the chemical nose-tongue system;

2.5 EXPERIMENTAL

2.5.1 Lectin extracted from the seed Dioclea sclerocarpa (LD)

Lectins ConBr (*Canavalia Brasiliensis*) was obtaining from the seeds, following methodology described by Moreira and Cavada (SILVA et al., 2016). Briefly, 110mL of total extract obtaneid by extraction with NaCl 0,15M (1:20;w;v) for 4h was submitted to a single-step affinity chromatography using sephadex G-50. The nonretained peak were eluted from the columm with the same equilibration solution (0,15M NaCl) where retained peak was eluted with glucose 0,1M in NaCl 0,15M. Retained peaks were freeze-dried and subjected to polyacrylamide gel electrophoresis 12.5% (SDS-PAGE). The gel was stained with coomassie brilliant R-250 and unstained with glacial acetic acid. Then, the lectins were dissolved in 100 nM NaCl phosphate buffered saline pH 7.2 (PBS) and used for all biological assays.

2.5.2 Design of 'nose'-type receptors: CQD-doped-Lectin ensemble.

In order to develop a sensing strategy based on a chemical 'nose' approach, the first step was to choose the elements would be doped to the compound the CQD-doped-Lectin ensemble, in the case was chose then elements N, P and S. In this regard, 2 mL of a CQD non doped (CQD-OH), CQD doped with N, P and S (CQD-N, CQD-P and CQD-S, respectively) dispersion (5.86 mg.mL-1, 0.544 $mg.mL^{-1}$, 0.230 $mg.mL^{-1}$ and 0.956 $mg.mL^{-1}$, respectively) were added in a quartz cuvette and fluorescence emission was recorded in the range of 370 – 600 nm using an excitation wavelength of 350nm. Subsequently, a sequential addition of aliquots containing the chosen *ConBr* lectin solution of adequante concentration was performed. Upon addition of each aliquot, the fluorescence spectrum was recorded using the conditions already reported. All the titration curves were carried out in triplicate.

2.5.3 Carbohydrates sensing study.

Initially, stock solutions of CQDs, ConBr lectin and sugars were prepared. Then, a stock solution of CQDs was firstly prepared in phosphate buffer (PB, 5 mM, pH 7.4). The absorbance of this solution was measured at 340 nm and the concentration of the CQDs was accurately obtained based on the calibration curve. It was ConBr lectin solutions of adequate concentration regarding the ratio optimization through titration curves were prepared using PB. Afterwards, a stock solution of each analyte sugar was also prepared in PB. Afterwards, the

sensing experiments were performed. For this purpose, 2 mL of the CQD-OH, CQD-N, CQD-P and CQD-S solution (5.86 $mg.mL^{-1}$, 0.544 $mg.mL^{-1}$, 0.230 $mg.mL^{-1}$ and 0.956 $mg.mL^{-1}$) and 20 μL of the metallic ion solution were added to the cuvette in order to form the *'nose'*-based receptor. After, the fluorescence spectrum (350 – 650 nm) was measured using the excitation at 350 nm. This measurement was considered to be the blank value and it was used to identify the CQDs.

Subsequently, 10μL of sugar solution of the analyte carbohydrate was added in order to obtain diferent concentration carbohydrate in the cuvette. The fluorescence spectrum in the range of 350 – 650 nm was recorded again using the 350 nm as excitation wavelength. This procedure was carried out for Glucose, Mannose and Methyl-α-D-mannopyranoside and three replicates were performed for each one of them. Therefore, 3 sugars were tested against the four CQDs – doped ensembles three times, which generates a training data matrix of 4 *'nose'*-based receptors x 3 sugars x 7 concentrations x 3 replicates. The same process was done for the CQD-doped-ConBr ensemble. In this step, the considered fluorescence response was the ratio $И_0$, where I and I_0 denote the final and initial fluorescence intensity at 450 nm (maximum emission intensity), respectively.

Upon careful analysis of the obtained fluorescence response for each concentration sugar, it was done the fingerprint for CQD–doped and CQDs-Doped-ConBr ensemble. Although, it is important to emphasize the whole spectrum was assigned as a response. Therefore, the raw data matrix has a huge number of variables (40 variables per CQDs–Doped and CQDs-Doped-ConBr ensemble). The whole generated data was then processed using statistical tools through an open-surce software called systat ("Systat Introduction", [s.d.]). Subsequently, this pre-processed data was further analysed using through linear discriminant analysis (LDA) to discriminate the analyte diferents concentrations sugars.

2.6 RESULTS AND DISCUSSION

2.6.1 ConBr lectin-based receptors: proportion optimization.

Once the sensor array is based on concurrent ConBr lectin interactions with doped CQDs and analytes, appropriate concentrations of Lectin ConBr and CQDs are critical for the formation of ConBr-CQD-doped assemblies.

Figure 26- Fluorescence titration performed at room temperature for *ConBr lectin*. Fluorescence intensity was investigated at 450 nm using an excitation wavelength of 350 nm and normalized using ($^{I}/_{I_0}$), where I_0 and $I-$ denote the intensity before and after the *ConBr* addition, respectively.

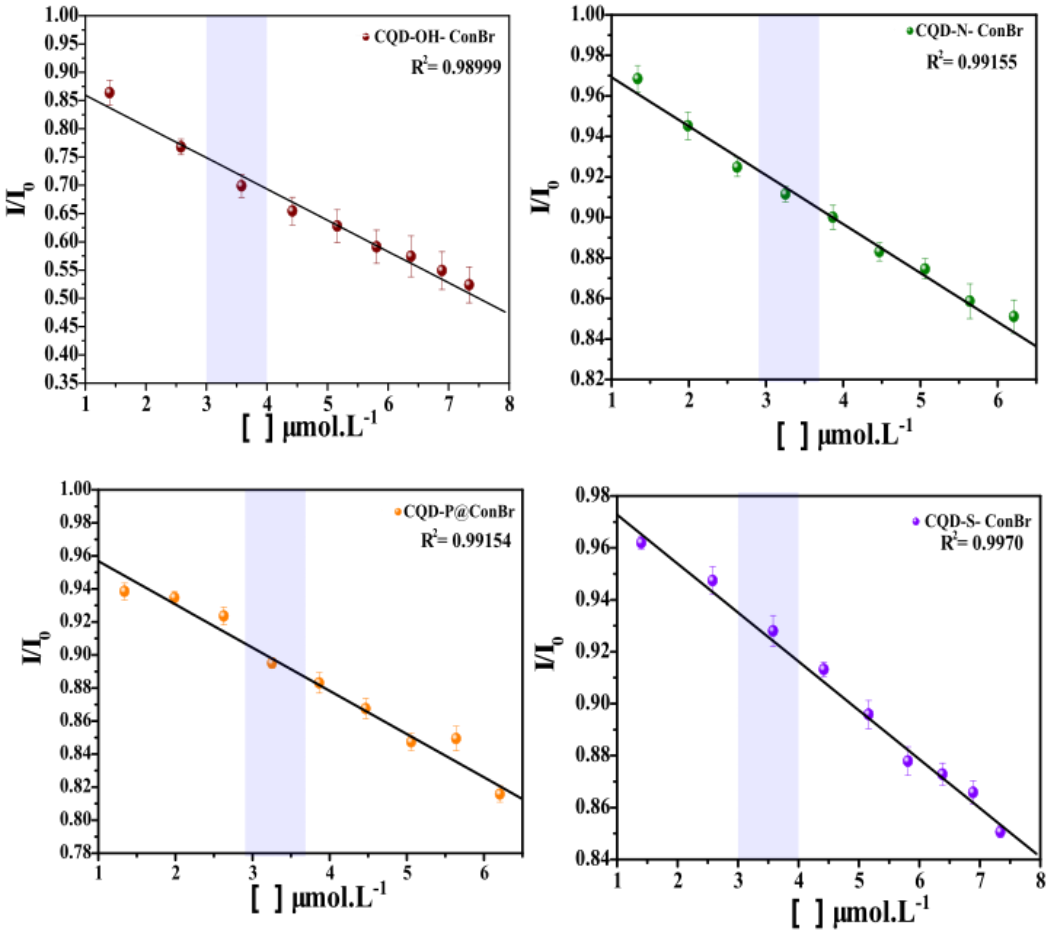

Source: author

Therefore, titration experiments were performed to determine the fluorescence response of the doped CQDs (pH = 7.4) to ConBr lectin. As shown in Fig. 26, the slope of the curves for CQD-OH, CQD-N, CQD-P and CQD-S with ConBr lectin was more pronounced in the concentration range of 1 to 8 mmol L^{-1}, indicating that the ConBr quenching efficiency for fluorescence CQD is the best in this concentration range.

The titration resulted in marked fluorescence quenching of CQDs, with surface saturation with the addition of ConBr, indicating that ConBr was quantitatively bound to the surface of CQDs. Thus, revealing the high affinity of ConBr with each CQDs, so that the binding profiles of each ConBr vary significantly, suggesting that fluorescence differential responses would be generated. Considering this information, the binding capacity and sensitivity ConBr lectin with analyte, 3.58mmol L^{-1} were selected. The haemagglutination assay is used to promote easy visualization of this red cell binding property by lectins, Figure 27 shows the ConBr-CQD-doped pool agglutination test in rabbit blood. Thereby, we can confirm that the choice of lectin concentration in the sensor assembly can be used because, by the hemagglutination test, it has active sites.

Figure 27- hemagglutination test in rabbit blood.

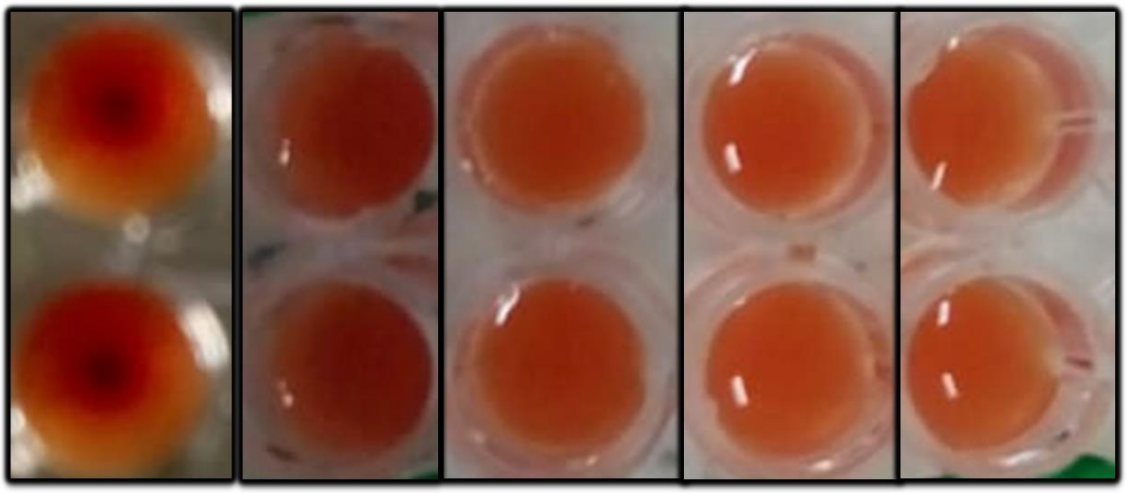

Source: author

2.6.2 Sensing of sugar.

After four ensembles of doped-ConBr CQDs have been constructed, Figure 28. 12 shows a schematic illustration of our nose-based strategy. First, the four receptors would provide distinct binding events for a given target carbohydrate. As a result, a unique fluorescence response pattern would be generated for each carbohydrate.

Figure 28- Schematic Illustration explaining the four-channel Sensor array to discriminate carbohydrate.

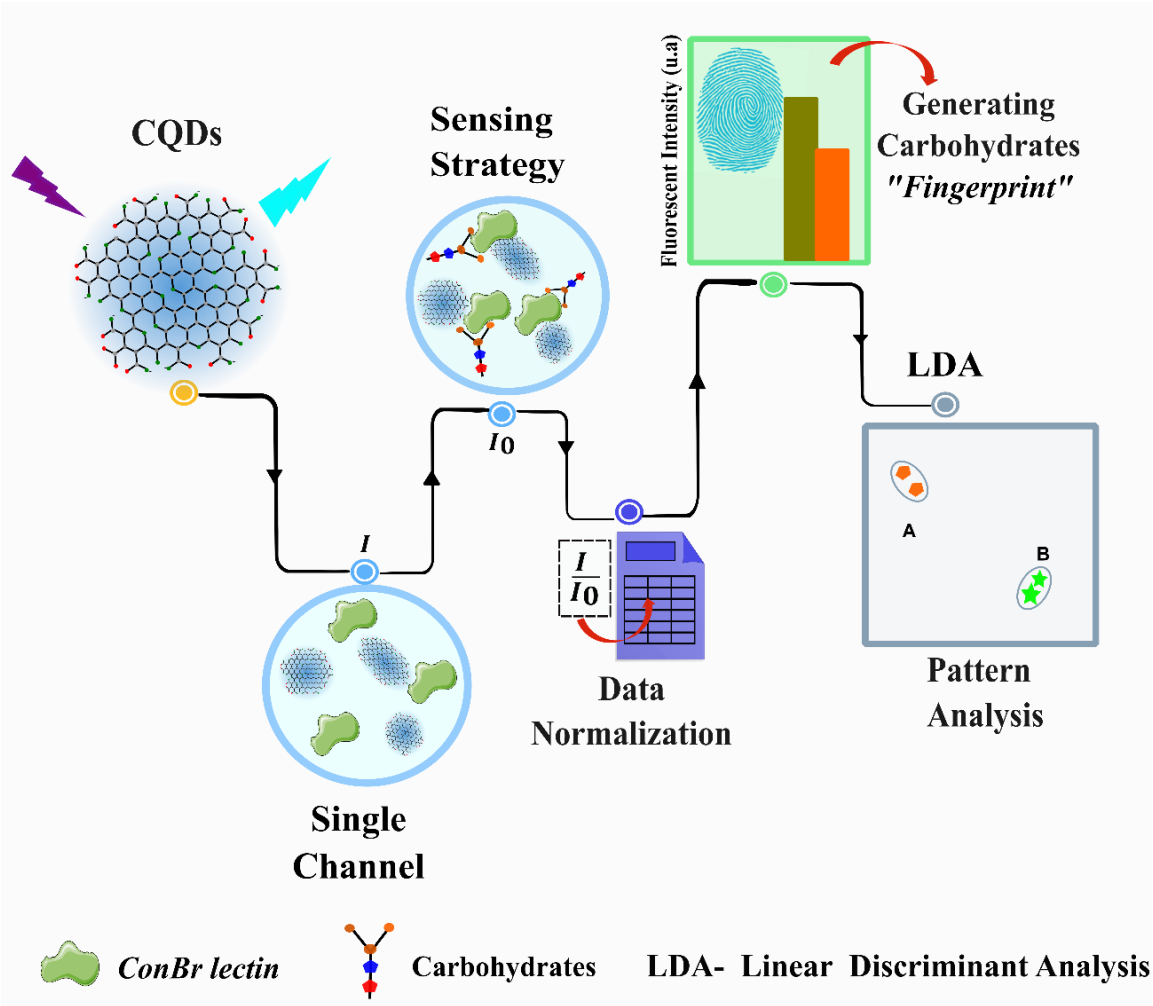

Source: author

Since the interaction between the receptors and a target carbohydrate would be different from each other. In this case, sugars interact with the active sites of lectin in different ways, so our hypothesis is that lectin may function as a surface modulating agent to alter the CQDs-carbohydrate interaction. In addition, the CQDs have different structures, so they have different interactions with lectin. Consequently, the four CQDs-doped-lectin ensemble would

have a different surface property, which further contributed for the differential binding events. So, this may improve the identification of each carbohydrate investigated through analysis of the respective fluorescence pattern using LDA.

To verify the differentiating power of our strategy, we first studied the effects of sugars on the CQD fluorescence intensity, forming a sensor array, the CQD fluorescence intensity varies in the presence of carbohydrates, indicating that these analytes have a significant effect. Then, solutions of the same carbohydrates were added to solutions of the four types of CQDs (CQD-OH, CQD-N, CQD-P and CQD-S) with lectin forming another set. Each mean value and standard deviation were calculated based on twelve repetitions. In this step, the fluorescence spectrum in the 380 - 650 nm range was acquired using 350 nm as the excitation wavelength. Therefore, a training matrix was created (4 nose recipients x 3 sugars x 12 repetitions). The relative fluorescence variation, I/I_0, induced by each carbohydrate against the sensor matrix was recorded to construct a fingerprint-specific map. The fingerprints contain relevant information about the carbohydrate sensor and CQD-doped-ConBr response to these carbohydrates.

Based on these data, Figure 29 shows the fluorescence response patterns (considering the fluorescence response at 450 nm) at different concentrations for each carbohydrate. Clearly, different patterns were observed, which may indicate the ability of our strategy to identify analyte carbohydrate. However, the statistical treatment of the training matrix was later performed with the LDA through Systat software to ensure discrimination.

Figure 29- Fluorescence response pattern of the analyte (a) Four CQD-doped-*ConBr*-Methyl-

α-D-Manopyranoside, (b) Four CQD-doped-*ConBr*-Glucose, (c) Four CQD-doped-*ConBr*-Mannose, (d) Four CQD-doped-Methyl-α-D-Manopyranoside, (e) Four CQD-doped--Glucose and (f) Four CQD-doped--Mannose.

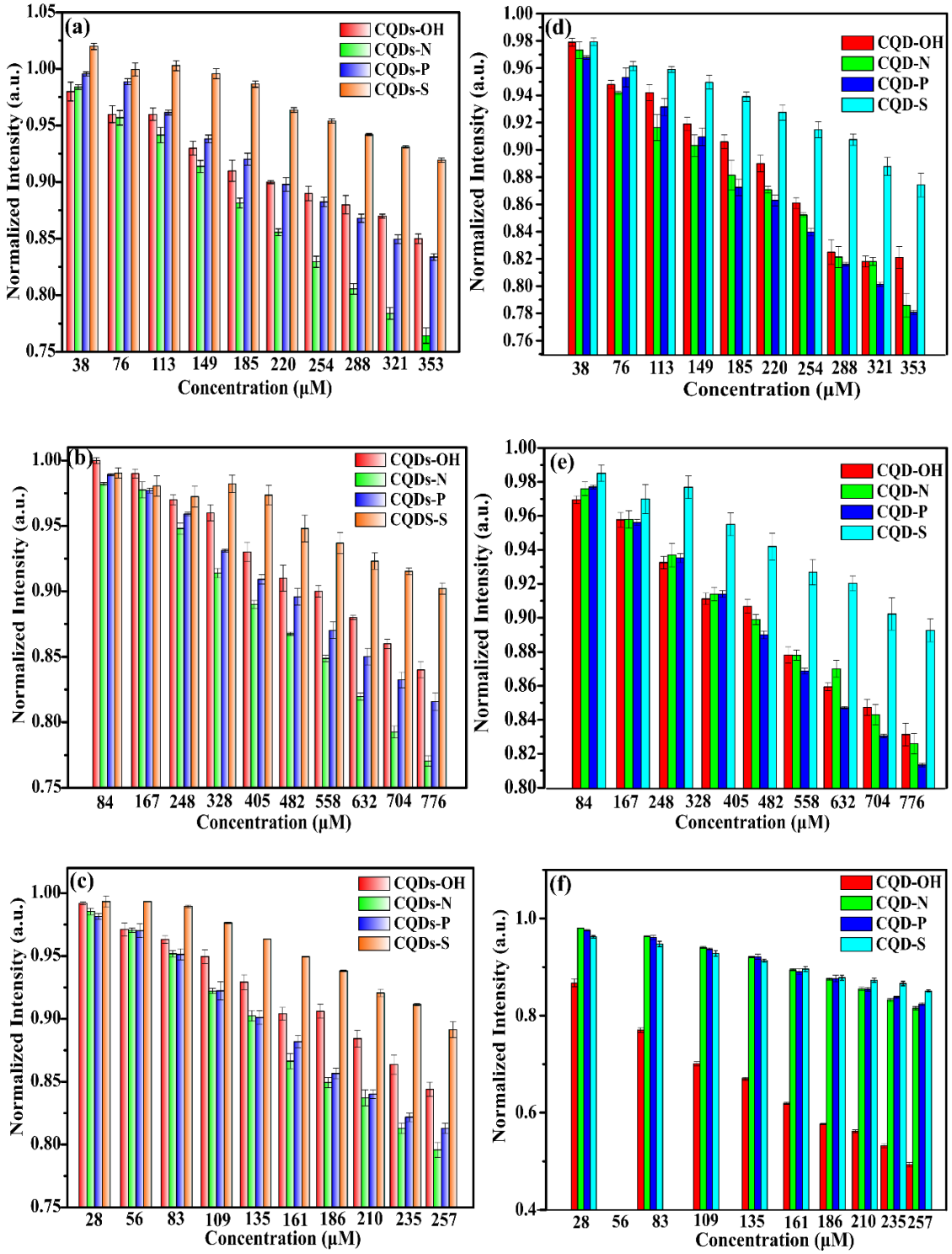

Source: author

In LDA, a linear model is constructed modeling set samples with known groups. In

the next step, samples with unknown group can be predicted based on the model. Considering two types of variation in the data, between-group and within-group variations, LDA proceeds to find linear models which maximize the former relative to the latter variation. In all cases, the separation of the aggregates is based on the standard Mahalanobis distance: the greater the distance between the aggregates, the greater the likelihood of correct identification of the investigated analytes.

The Figure 30a shows a 2D graph generated using the two main canonical factors (97.4% and 1.6%) for glucose samples with the CQD-doped array sensor. Comparatively, figure 30b shows the 2D graph of the two major canonical factors (47.8% and 43.5%) for the CQD-doped-ConBr array sensor. In the first case, it is possible to clearly visualize the separation of the ten analyte concentrations. Then, in the CQD-doped-ConBr sensor assembly, it is possible to discriminate concentrations and larger spaces. In addition, greater separability occurs between groups.

Figure 30- Canonical score plot for the fluorescence patterns obtained from LDA utilizing the two most significant factors generated considering (a) *CQDs-Doped* and (b) the four *CQDs – Doped-ConBr* ensembles with diferents concentrations glucose in µmol, respectively.

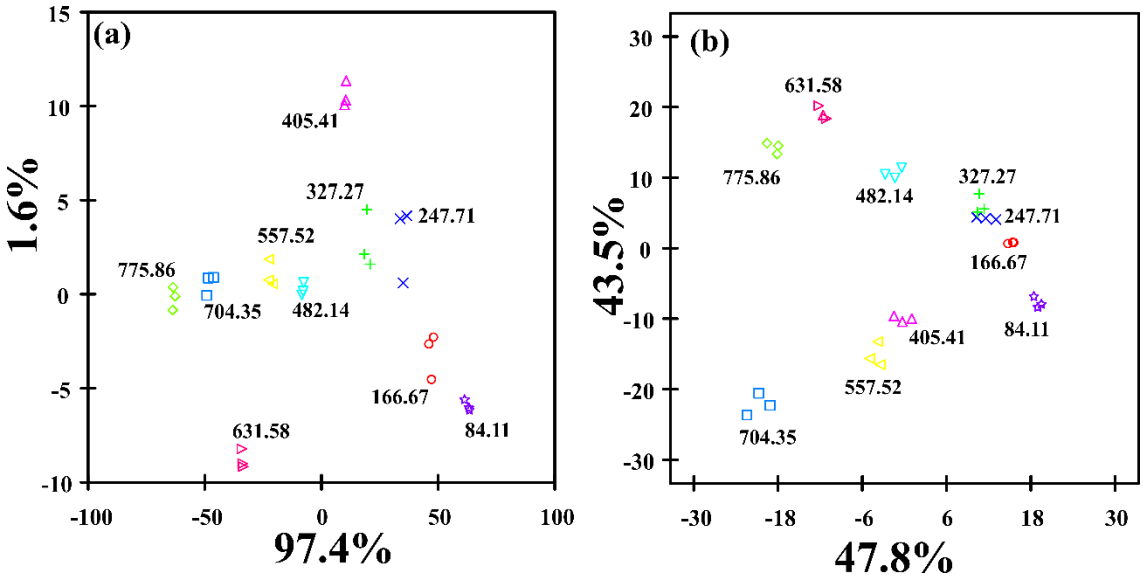

Source: author

Figure 31a represents the 2D graph of the main canonical factors (83.2% and 2.9%) for the array sensor CQD-doped interacting with mannose. The separability of the analyte concentration groups is clearly observed, but with the dimensional increase it is not possible to discriminate the groups. However, when the CQD-doped-ConBr ensemble is possible to

differentiate all groups and the increase of the lower dimensional range shown in the 2D graph (figure 31b) of the canonical factors (83.2% and 2.9%).

Figure 31- Canonical score plot for the fluorescence patterns obtained from LDA utilizing the two most significant factors generated considering (a) *CQDs-Doped* (b) the four *CQDs – Doped-ConBr* ensembles with diferents concentrations mannose in µmol, respectively.

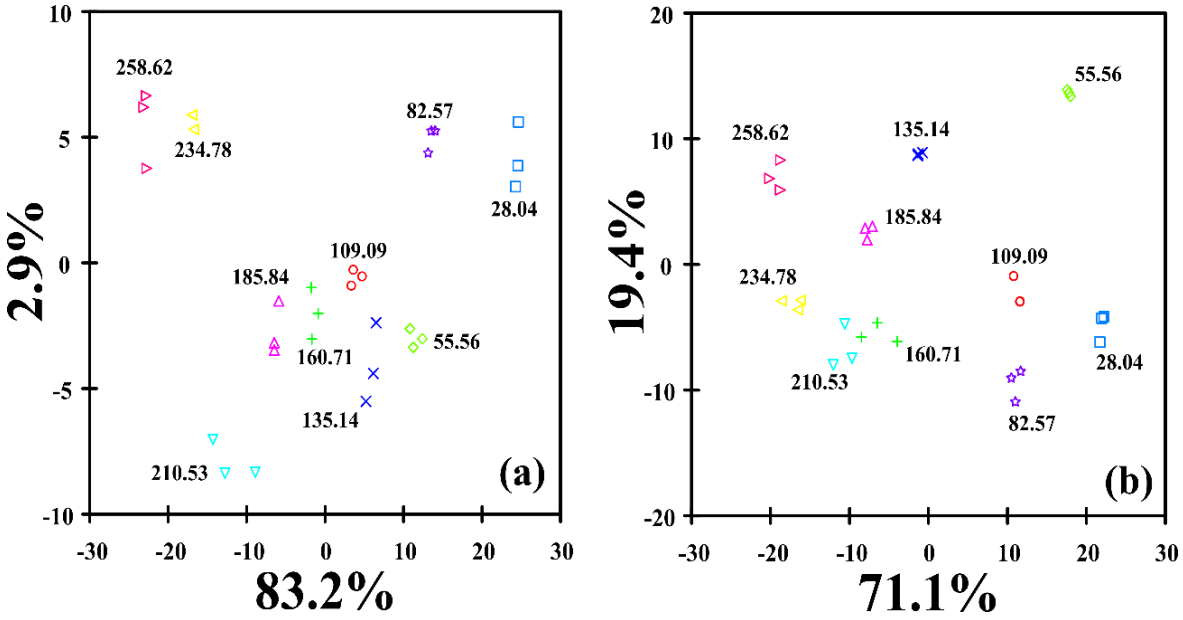

Source: author

Analyzing Figure 32a of the two canonical factors (94.6% and 2.9%) for the CQD-doped ensemble interacting with Methyl-α-D-mannopyronide, a separability between groups can be observed. Figure 16b represents the 2D graph of the two main canonical factors (93.7% and 3.9%) of the CQD-doped-ConBr set interacting with the same analyte. Again, the groups were found to be distant form one another, which evidences the discrimination power. However, the distribution of the cluster over the 2D space of the Figure 32b is quite distinct compared to the Figure 32a. Interestingly, the groups obtained by treating the data matrix acquired to build the Figure 32b showed a shift to lower and upper regions. This was not observed in the Figure 32a, which may indicate a different behavior of the analyte on the surface of the CQD. This difference might pointed out for the modulation of the CQDs surface by the ConBr lectin, which changed the interaction between the analyte and the carbon-based nanostructure.

Figure 32- Canonical score plot for the fluorescence patterns obtained from LDA utilizing the two most significant factors generated considering (a) *CQDs-Doped* (b) the four *CQDs – Doped-ConBr* ensembles with diferents concentrations Methyl-α-D-mannopironoside in μmol, respectively.

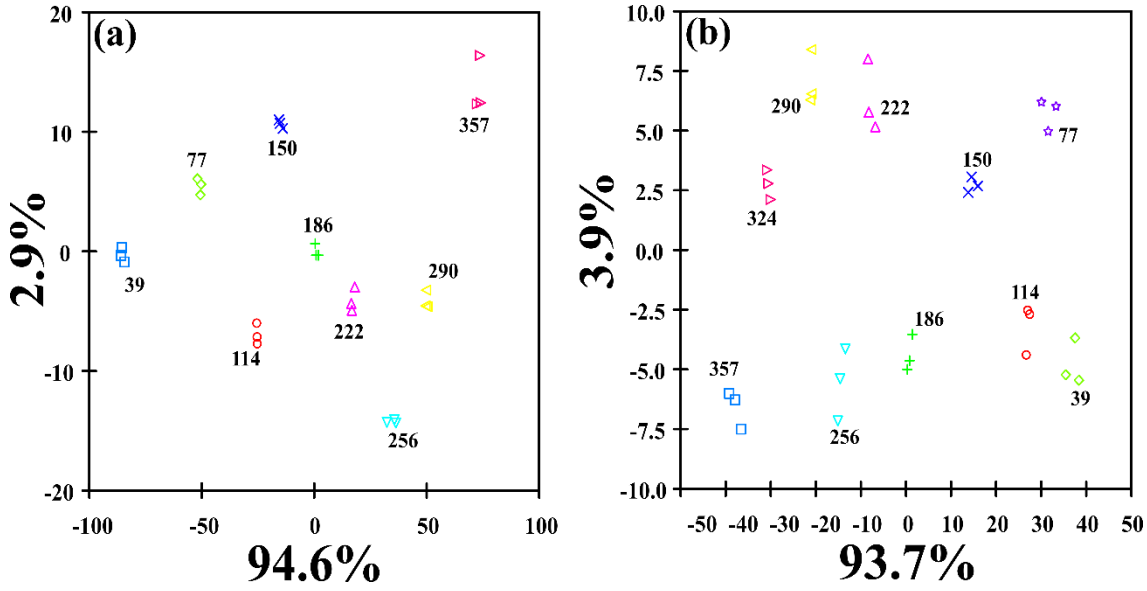

Source: author

Figure 33a represent the two main canonical factors of the CQD-doped ensemble for the lowest, intermediate, and highest concentrations analyzed (97.4% and 2.6%, 97.9% and 2.1%, 99.8%, and 0.2%, respectively). The Figure 33b represent the two main canonical factors for the corresponding CQD-doped-ConBr ensemble (81.8% and 18.8%, 97.0% and 3%, 99.6% and 0.4%), respectively. In all cases, the separability occurs, but when the interaction with the CQD-doped-ConBr ensemble occurs, it is possible to observe an inversion of groups, the group shifts to a smaller dimension in the treatment of LDA.

Figure 33- Canonical score plot for the fluorescence patterns obtained from LDA utilizing the two most significant factors generated considering (a) *CQDs-Doped* and (b) the four *CQDs – Doped-ConBr* ensembles with low (fig a and b), intermediate (fig. c and d) and larger (fig.e and f) concentrations carbohydrates in μmol, respectively.

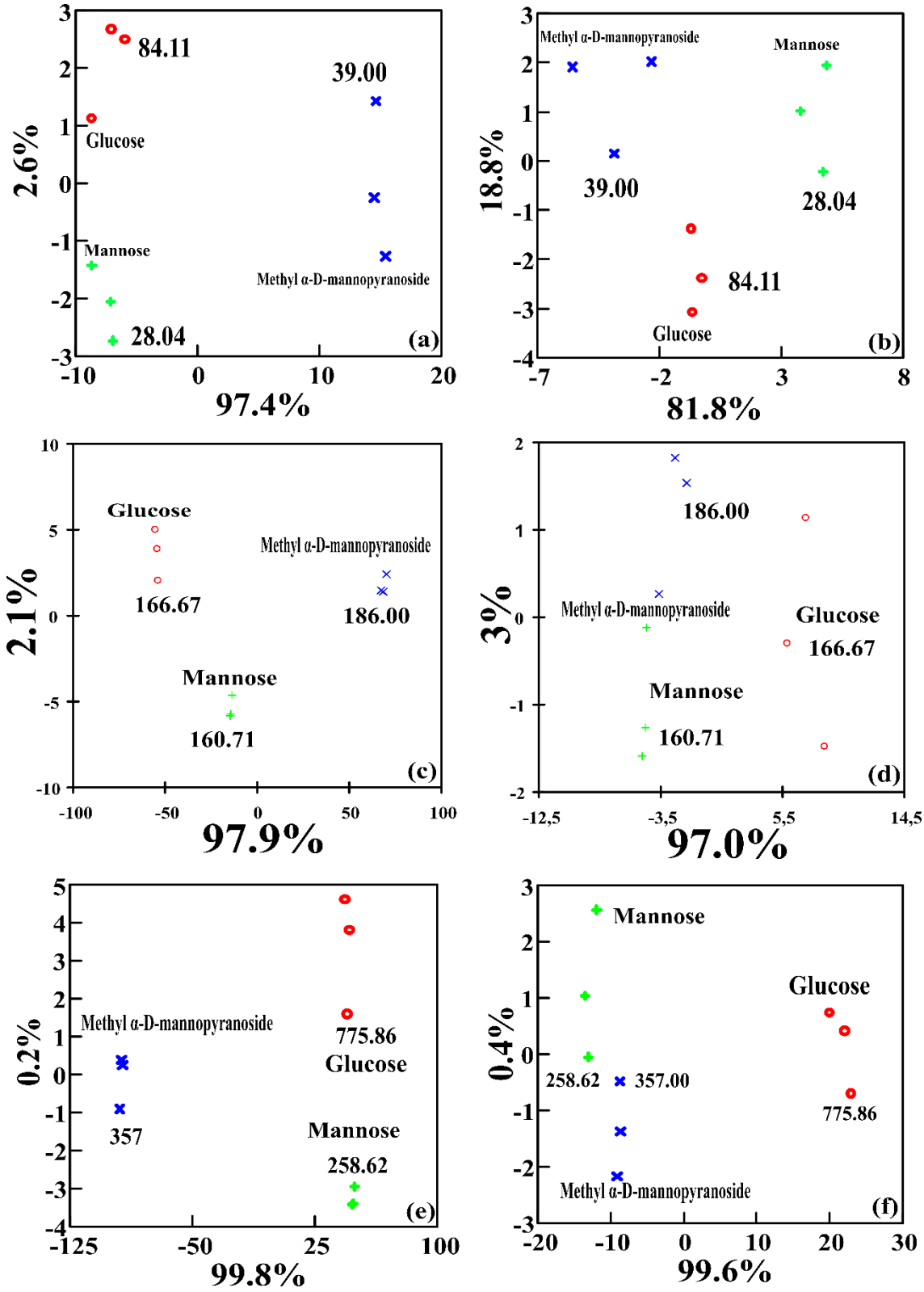

Source: author

It is widely accepted that ConBr are specific for mannose, glucose and derivatives, the most specific monosaccharide being methyl-α-D-mannopironoside. Interactions between lectins occur by hydrogen bonds by the active sites. In the case of Methyl-α-D-mannopironoside, in addition to hydrogen bonding, hydrophobic interactions also occur, helping, on the differentation process. In addition, the amount of binding in glucose is much higher than in mannose, which explains why there is greater separability between groups when interacting carbohydrates with the CQD-doped-ConBr ensemble. As it can be seen, the cases were grouped into three distinct groups. According to the classification matrix, 100% accuracy was obtained, it can be observed that the addition of ConBr lectin increases discriminating carbohydrates, demonstrating the ability of our language-based strategy to target carbohydrate.

2.7 CONCLUSIONS

Given the above, it was developed from a sensor array strategy in which CQD was used as a signal and *ConBr* lectin as a receptor. Additionally, it was possible to discriminate three types of carbohydrates (glucose, mannose and Methyl-α-D-mannopyronoside) in a concentration range between 30 -800 μmol L^{-1} using linear discriminant analysis (LDA). Besides it was possible to observe that after the interaction of the CQDs the lectins became active. Thus, it was demonstrated the development of a nose-tongue strategy that can be used for sugar identification and quantification, but it is important to emphasize that the tests were performed as a training matrix. To prove the efficiency of the strategy developed, it will be necessary to conduct experiments with real samples. The proposed sensor was successfully obtained with great potential for carbohydrate sensing applications in cancer cells.

3. DOPED CARBON QUANTUM DOTS: INTERECTION WITH CONBR FOR IDENTIFICATION MYELODYSPLASIC SYNDROME (MDS).

3.1 INTRODUCTION

Myelodysplastic syndrome (MDS) is one of the five main categories of myeloid neoplasms according to the World Health Organization (WHO) classification system (A. ARBER; ORAZI, 2016). As its name implies, MDS is not a single entity, but consists of a collection of conditions conferring the heterogeneous nature of these disease. Ineffective hematopoiesis, morphological dysplasia in the bone marrow, peripheral cytopenia and genetic instability are some characteristics present in MDS patients. In addition, about a third of these patients progress to acute myeloid leukemia (AML)(RAZA et al., 2010; RAZA; GALILI, 2012) .

MDS can be divided into the following subtypes: (1) Single Lineage Dysplasia MDS (MDS-SLD) and (2) Multiple Lineage Dysplasia MDS (MDS-MLD), (3) Single Lineage Ring Sideroblast MDS (MDS-RS-SLD) and (4) Multiple Lineage MDS (MDS-RS-MLD), (5) MDS with excess blasts 1 and 2 (MDS-EB 1 and 2), (6) unclassifiable MDS (MDS-U) and (7) MDS with isolated del5q(HASSERJIAN, 2019) .

MDS most often affects older adults with a mean age of 65 to 70 years at diagnosis. About 86% of MDS cases are diagnosed at age ≥ 60 years and less than 10% of patients are younger than 50 years old. Thus, its prevalence increases with age and is significantly increased in males (ADÈS; ITZYKSON; FENAUX, 2014; RAZA; ALI; IVERSON, 2014). As it is a disease that has clinical symptoms that are related to peripheral cytopenias and are very similar between the different subtypes (anemia, thrombocytopenia, neutropenia). Due to nonspecific symptoms and signs, the laboratory diagnosis is determinate as: evaluation of the bone marrow and peripheral blood reveals the characteristics of the disease and excludes other pathologies that are manifested through peripheral cytopenias (ADÈS; ITZYKSON; FENAUX, 2014). Therefore, considering the higher prevalence in elderly patients and the aging of the world population, as well as greater diagnostic awareness, the incidence of MDS is expected to increase substantially in the coming decades(WINTER et al., 2020).MDS is undoubtedly a challenging disease, supported by a complex and dynamic pathogenesis. Thus, new testing strategies can offer advances in management, medical decisions, diagnosis, and possible prognostic association (ADÈS; ITZYKSON; FENAUX, 2014; WINTER et al., 2020).

In recent years, biorecognition molecules from natural sources with diagnostic and therapeutic potential has been studying. The identification of carbohydrate moieties on the cell

surface and glycoconjugates have been performing using lectins, a widely known heterogeneous group of proteins (glycoproteins) of non-immune origin. Lectins can bind carbohydrates through molecular sites, with high affinity and specificity (AYAZ AHMED; MOHAMMED; VEERAPPAN, 2015; COELHO et al., 2017) and can be used as a molecular tool to recognize antigens and to differentiate cancer cells from normal cells (CAVADA et al., 2020).

Selective array-based sensing methodologies provide potential alternatives to specific recognition approaches, relying on the differential affinities for analyte identification. Sensors have been developed utilizing this approach for identification of cancer cells, using fluorescent polymers, magnetic glyco-nanoparticles, and non-covalent conjugates of gold nanoparticles and fluorophores (LIU et al., 2013).

In order to further broaden these advantages, CQDs are considered for the manufacture of single-channel sensor arrays. Due to their simple synthesis, low toxicity, good biocompatibility and ease of surface modifications with functional groups (for example, hydroxyl, carboxyl, epoxy, amino, amides, etc.) (SUN; LEI, 2017). In addition, these nanoparticles can be doped (e.g. P and S) by altering the fluorescent emission as well as their reactivity and sensitivity (MIAO et al., 2020; SUN et al., 2017b), enabling the sensing of several analytes such as toxic metals ions (WANG et al., 2017), proteins (CARNEIRO CRUZ et al., 2019a; FREIRE et al., 2017) and pesticides (CARNEIRO et al., 2019b).

Herein, we developed a detection strategy using fluorescent array sensors based on doped CQDs based on phosphorus and sulfur to identify and classify the different types of MDS using the *ConBr* lectin as a ligand. Using our standard methodology, all MDS types investigated generated a different fluorescence response pattern, which allowed discrimination of MDS types through a protocol using principal component analysis (PCA) and linear discriminant analysis (LDA).

3.2 OBJECTIVES

3.1 General

To develop sensing strategies by using diferrent doped-CQDs to identify and classify the different types of MDS.

3.2 Specific

- To propose a MDS sensing strategy using the CQD-doped-ConBr lectin suite based on the chemical nose-tongue system;
- To evaluate interaction ensemble CQD-doped-ConBr lectin with MDS ;

3.3 EXPERIMENTAL

3.3.1 Materials

All reagents used in this work were of analytical grade and used as such without further purification. citric acid anhydrous (99.5%, Sigma Aldrich), phosphoric acid P.A (99%, Vetec), lectin isolated from seeds, dialysis membrane (0.5-1.0KDa, Spectrum Laboratories, ultra-high Milli-Q water (R = 18.2 MΩ.cm^{-1} at 25 ° C).

3.3.2 CQDs Characterization

The use of characterization techniques is able to identify optical, structural and chemical properties. Therefore, the absorption spectra of the CQDs were recording in the spectrophotometer UV-Vis Shimadzu UV-2600. The fluorescence spectra of the CQDs were obtained in the Shimadzu RF-6000 spectrofluorophotometer and cytation 3 microplate reader, biotek. X-ray photoelectron spectroscopy (XPS) analysis was performed on a Physical Electronics Quantum 2000 spectrometer using a monochromatic Al Kα excitation at a spot size of 10 mm with a pass energy of 46.95 eV. Subsequently, the structure of the CQDs were confirmed by Gaussian deconvolution of the Raman spectrum (LabRAM Jobin-Yvon, HORIBA) collected at λ_{ex}= 785 nm. The Atomic Force Microscopy (AFM) image was obtained utilizing an Asphalt Research microscope of the MFP-3D AFM type.

3.3.4 Patients

27 patients with MDS diagnosed according to the World Health Organization (WHO) (A. ARBER; ORAZI, 2016) and the Revised International Prognostic Scoring System (IPSS-R)(GREENBERG et al., 2012).

Table 1- Patients Experimental 1

EXPERIMENTAL 1	
CN	CONTROL
P1	MDS-SLD
P2	MDS-SLD
P3	MDS-RS-SLD
P4	MDS-EB2
P5	MDS-EB1
P6	MDS-EB2

Table 2- Patients Experimental 2

EXPERIMENTAL 2	
P1	Control (CN)
P2	MDS-EB2
P3	MDS-MLD
P4	MDS-EB1
P5	MDS-LMC
P6	MDS-EB2
P7	MDS-MLD
P8	MDS-EB2
P9	MDS-SLD
P10	MDS-MLD
P11	MDS-EB2
P12	MDS-RS-SLD
P13	MDS-MLD
P14	MDS-HIPO
P15	MDS-EB2
P16	MDS-EB2
P17	MDS-LMA
P18	Control (CN)
P19	MDS-EB2
P20	MDS-RS-SLD

3.3.5 ConBr-based receptors: proportion optimization.

Once the sensor array is based on concurrent *ConBr* interactions with doped CQDs and analytes, appropriate concentrations of *ConBr* and CQDs are critical for the formation of *ConBr*-CQD-doped assemblies. Therefore, titration experiments were performed to determine the doped-CQD fluorescence response (pH = 7.4) to *ConBr* lectin. As shown in figure 26, the slope of the curves for CQD-OH, CQD-P and CQD-S with *ConBr* was more pronounced in the concentration range of 1 to 8mmol L^{-1}, indicating that the ConBr quenching efficiency for fluorescence CQD is the best in this concentration range. Each average value and standard deviation were calculated based on six replicates. The highlight in each graph denotes the chosen concentration to compound the CQDs – *ConBr* ensemble. The titration resulted in marked fluorescence quenching of CQDs, with surface saturation with the addition of *ConBr*. Thus, revealing the high affinity of *ConBr* with each CQDs, so that the binding profiles of each *ConBr* vary significantly, suggesting that fluorescence differential responses would be generated. Considering this information, the binding capacity and sensitivity *ConBr* with analyte, 3.58 mmol L^{-1} were selected.

3.3.6 MDS sensing study.

Initially, a stock solution of CQD-OH, CQD-P and CQD-S was prepared in solution-P (PB, 5 mM, pH 7.4). The absorbance adjusted in 350nm solutions were made with CQD accuracy based on the curvature of adjustment. Afterwards, a Lectin *ConBr* stock solution was also prepared for the detection experiments. Solutions were acquired by measurements of absorption at 280 nm. As for CQDs, focus on the lectin was formerly using Beer-Lambert's law ($C = A280/(\varepsilon_{280} \cdot l)$). For the initial detection experiments, 200 µL of the solution of each CQDs, CQD-OH (5.86 mg mL^{-1}), CQD-P (0.230 mg mL^{-1}), CQD-S (0.956 mg mL^{-1}) strips were added to wells in a 96-well plate (300 µL Thermoscientific black bottom microplate), and 10 µL of the *ConBr* selection solution was added to each plate and the intensity value followed by fluorescence was average at 370-550 nm using a 350 nm. This value was considered an initial intensity (I_0). Then, 10 µL of MDS blood plasma was added. After 1 min, the fluorescence intensity was recorded again (I). Therefore, 27 blood plasmas were tested against the three sets of CQDs-ConBr three, which generates a training data matrix of 3 times more repetitions in 'nose' x 27 blood plasma x 3 replicates. In this step, the fluorescence response was the I/I_0 ratio, where I and I_0 denote the final and initial fluorescence intensity at 450 nm (maximum emission intensity), respectively. After analyzing the fluorescence response made for each blood plasma,

a fingerprint was built for the CQDs-ConBr set. However, it is important to emphasize that the entire spectrum was assigned as a response. Therefore, a raw data matrix has a large number of variables (180 CQDs-Doped-*ConBr* ensemble variables). All generated data was then processed using statistics through an open-surce software called systat. Subsequently, these different pre-processed data were studied using linear analysis (LDA) to discriminate the types of MDS in blood plasma.

3.4 RESULTS AND DISCUSSION

As proposed in the previous chapter, the CQD-ConBr ensemble has great potential to detect the diagnosis of some diseases, among which we highlight MDS.. However, our proposal is to develop a sensor array methodology using the CQD-ConBr set interacting blood plasma samples from peripheral blood, as illustrated in figure 34.

Figure 34- Schematic illustration of response sensor array based on CQD-ConBr.

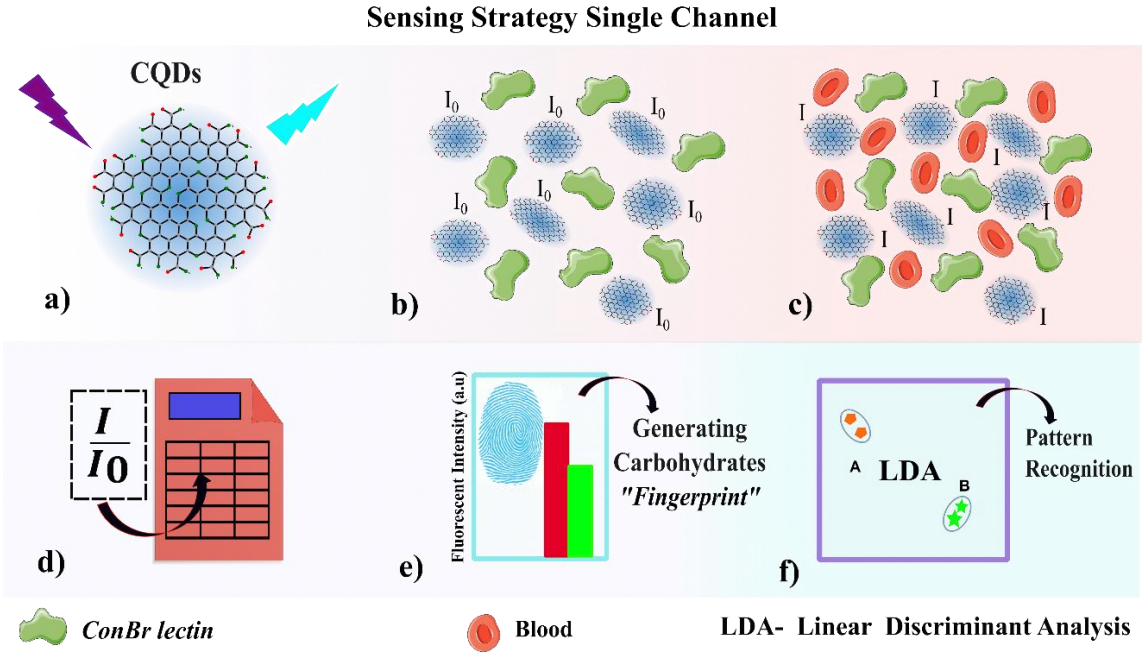

Source: Author

In this case, the lectin concentration was adjusted to 3.58 mmol L^{-1} and initially, the study was carried out with 7 patients, 1 control patient without a diagnosis of MDS and sample taken from peripheral blood and 6 patients with a diagnosis of MDS, 5 samples taken from bone marrow and 1 sample from peripheral blood. Since the interaction between the receptors and the target MDS sample would be different from each other. In this case, the MDS samples interact with the active sites of the lectin in different ways, which works as a surface modulating agent to alter the CQDs-MDS interaction. In addition, CQDs have different structures, therefore, they have different interactions with the lectin and the lectin easily binds to carbohydrates as previously studied, with that the MDS samples have among their characteristics high concentrations of carbohydrates, due to contributions of cytopenias and alterations genetics. Consequently, the ensemble of three doped-CQDS interacting with lectin would have a different surface property, which further contributed to differential binding events.

Thus, this can improve the identification of each investigated MDS by analyzing the respective fluorescence pattern using LDA.

To verify the differentiating power of our strategy, we studied the effects of MDS by adding samples to solutions of the three types of CQDs (CQD-OH, CQD-P and CQD-S) with the lectin forming the set. Each mean value and standard deviation were calculated based on twelve replicates. In this step, the fluorescence spectrum in the range of 380 - 650 nm was acquired using 350 nm as the excitation wavelength. Thus, a training matrix was created (3 nasal receptors x 7 samples x 3 repetitions). The relative fluorescence variation, I/I_0, induced by each MDS sample against the sensor array was recorded to build a fingerprint. Fingerprints contain relevant information about the MDS sensor and the CQD-ConBr response to these samples.

Based on these data, figure 35a shows the fluorescence response patterns (considering the fluorescence response at 450 nm) for different samples. Clearly, different patterns were observed, which may indicate the ability of our strategy to classify the different types of MDS. However, the statistical treatment of the training matrix was performed later with the LDA using Systat software to ensure discrimination.

Figure 35- Fluorescence response pattern of the analyte (a) Three CQD-doped-*ConBr*-Patient MDS (b) Canonical score plot for the fluorescence patterns obtained from LDA utilizing the two most significant factors generated considering three CQD-doped-*ConBr*-Patient MDS.

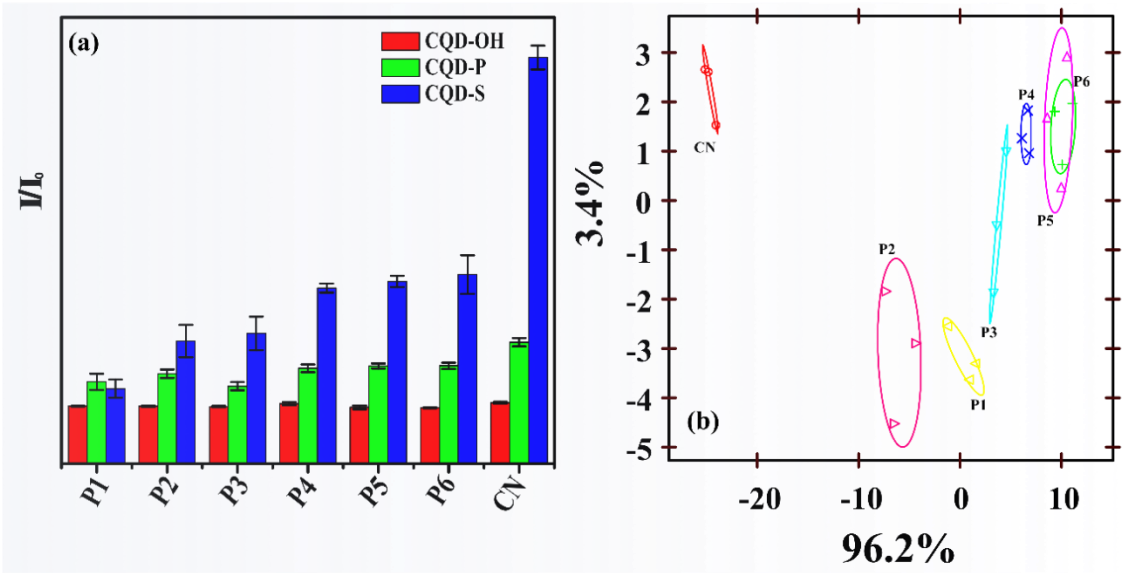

Source: Author

Figure 35b represents the two main canonical factors (96.2% and 3.4%) of the CQD-*ConBr* doped set for the analyzed MDS samples. It is possible to observe that the

separability of the control sample (CN) is distant from the other samples diagnosed with MDS. The Samples P1 were diagnosed with MDS-SLD which has as characteristics the count of at least two types of blood cells (red blood cells, leukocytes or platelets) are low. Ring sideroblasts may (or may not) be present. The number of blasts in the bone marrow is less than 5%. Blasts are rare or absent in blood. P2 were diagnosed with MDS-SLD, patients who have this type of MDS have low numbers of one blood cell type, but normal numbers of the other two types. Examples: refractory anemia (most common), refractory neutropenia, and refractory thrombocytopenia. In the bone marrow of patients at least 10% of the cells are initially affected, but other cell types are normal. There is a normal number (less than 5%) of blasts.

P3 were diagnosed with MDS-RS-SLD this type of MDS has a condition similar to refractory anemia except that 15% or more of red blood cells in the blood or bone marrow contain circles of iron deposits around the nucleus. From 10% to 15% of patients with myelodysplastic syndrome have this type. P4 and P6 were diagnosed with MDS-EB2 which are characterized as one or more cell types are low in the blood and appear abnormal in the bone marrow. The number of blasts in the bone marrow is between 10 to 20% blasts. P5 were diagnosed with MDS-EB1, characterized by one or more cell types that are low in the blood and appear abnormal in the bone marrow. The number of blasts in the bone marrow is higher, but still less than 10%.

Samples P1, P2, P3 are classified as low risk MDS because the probability of developing leukemia is low, we can see that these samples are close, but in the same region. Samples P4, P5 and P6 are types of MDS classified as high risk, they are very likely to become leukemia, we can see that they are close in the same region, but it is possible to observe that samples P4, P5 and P6 are close. It is already possible to observe that our sensing system can distinguish high and low grade SMD. In the case of samples P4 and P6, which are the same type of MDS, but are separated, a point to be discussed is that they are samples taken from different regions, P4, is a bone marrow sample and P6, a sample taken from peripheral blood. One of the main difficulties in quickly identifying the type of MDS is that the bone marrow exam is invasive and painful for the patient, which is possible to observe that we can identify this type of MDS only by peripheral blood samples.

To improve our method, new analyzes were performed regarding the consistency of the method, a training matrix (3 nasal receptors x 12 samples x 6 repetitions) with peripheral blood samples were analyzed. The relative fluorescence variation, I/I_0, induced by each MDS sample against the sensor array was recorded to build a fingerprint-specific map. Clearly, different patterns were observed, indicating once again the ability of our strategy to classify the

different types of MDS. Figure 36a shows the fluorescence response patterns (considering the fluorescence response at 450 nm) for different samples.

Figure 36- Fluorescence response pattern of the analyte (a) Three CQD-doped-*ConBr*-Patient MDS (b) Canonical score plot for the fluorescence patterns obtained from LDA utilizing the two most significant factors generated considering three CQD-doped-*ConBr*-Patient MDS.

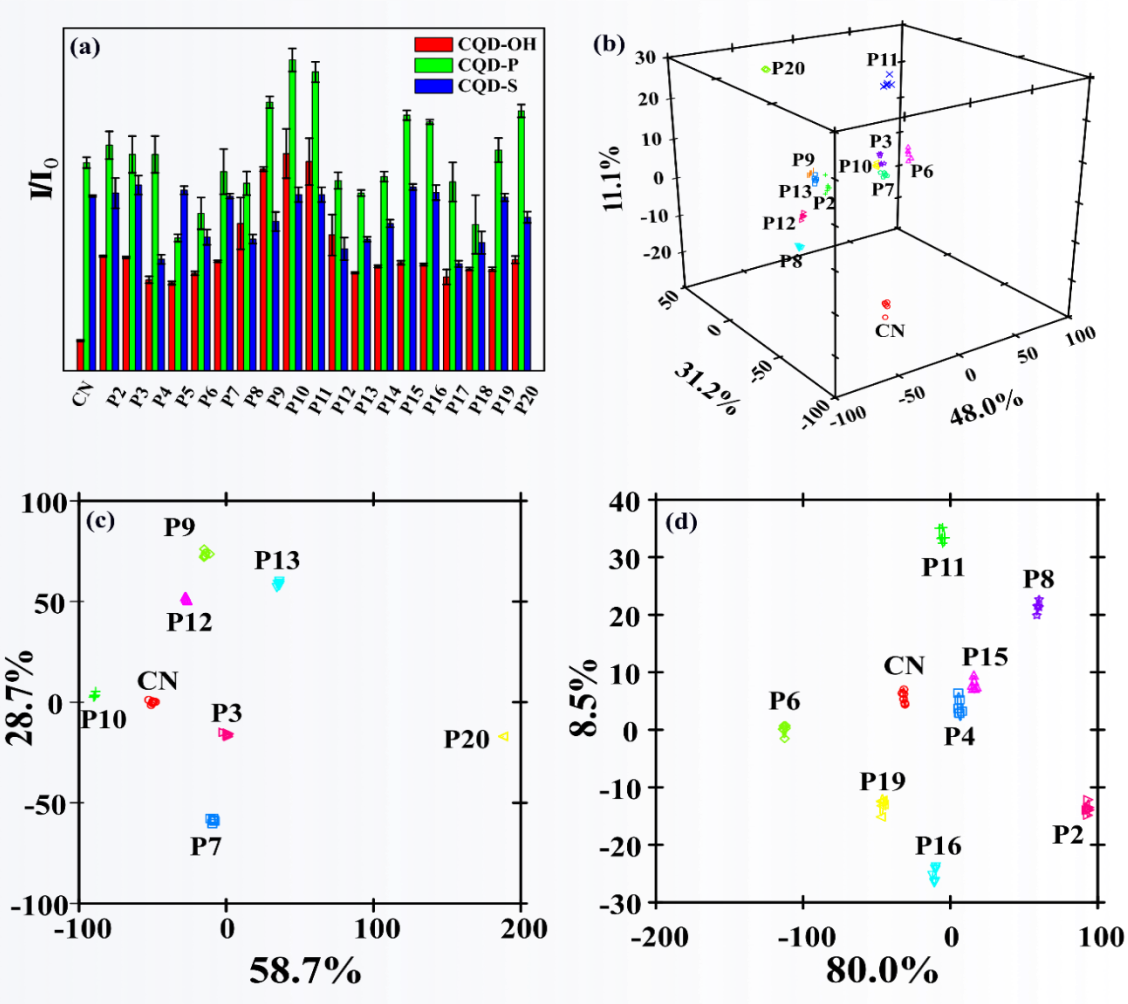

Source: Author

Analyzes were performed with 20 different samples, from these 20 samples were chosen 12 samples that have some similar characteristic in the set of laboratory data, being the chosen factor the amount of blasts. These samples have a percentage of blasts less than 5%. However, they were diagnosed with different MDS. The samples chosen were P3, P7, P10, P13 diagnosed with MDS-MLD, P9 diagnosed with MDS-SLD and patients P12 and P20 diagnosed with MDS-RS-SLD, these are classified as low risk MDS. In addition, patients P2, P6, P8 and P11 were chosen as samples of high risk MDS patients diagnosed with MDS-EB2 type. Figure

36b represents three canonical factors (48%, 31.2% and 11.1%) of the doped-CQDs-ConBr ensemble for the analyzed samples. It is possible to observe the separability of the control sample (CN) in relation to the other samples.

In addition, it is possible to observe the separation between patients considered low and high risk, however, analyzing patients P3, P7 and P10 are close to a diagnostic region with high risk MDS. These patients are diagnosed with MDS-MLD this type of MDS is considered intermediate since in about 10% of patients it turns into leukemia. It is important to note that the P12 and P20 patients within the low risk group are samples that have the same type of MDS, however, they are in separate regions. In addition, samples from P9, P12 and P13 patients are close together and are diagnosed with different types of low-risk MDS. Possibly, this is due to factors such as: the stage of the disease, types of cytopenias and changes in karyotype.

In order to observe the behavior of the samples within the group, figure 36c represents two canonical factors (58.7% and 28.7) for the low risk samples. It is possible to observe the separability between samples P3, P7 and P10, as well as the separability of sample P20 in relation to other samples, this sample in its clinical diagnosis shows a change in karyotype, which would explain this separability.

Also, an analysis of the two canonical factors was performed for the high-risk samples. Figure 36d represents two factors (80% and 8.5%) which shows the separability between the samples diagnosed with the same type of MDS, however, it is possible to observe that sample P6 is distant in relation to the others, this sample has in its clinical diagnosis is a change in karyotype in relation to high risk samples. However, samples P6 and P20 that are diagnosed with high and low risk MDS, respectively, have a change in karyotype and analyzing figure 36b are in different regions, which despite having the same similarity in the percentage of blasts and in their diagnoses clinicians have a change in karyotype separability occurs. Finally, the sensor array strategy can be a methodology to be used to classify MDS into low and high risk. However, more detailed studies will be necessary to make the method more robust.

3.5 CONCLUSIONS

Given the above, it was developed from a sensor arrangement strategy in which CQD was used as a signal and the lectin ConBr as a receptor. In addition, it was possible to discriminate the types of MDS and classify them into high and low risk using linear discriminant analysis (LDA). In addition, it was possible to observe that after the interaction of the CQDs, the lectins became active. Thus, the development of a nose-tongue strategy that can be used to identify MDS and classification into high and low risk was demonstrated, but it is important to emphasize that the tests were performed with real samples that did not undergo any treatment process, with it is necessary to adjust the parameters to improve the methodology and with this, it is possible, in addition to classifying its degree of complexity, to identify the type of MDS detected. The proposed sensor was successfully obtained with great potential for MDS detection applications.

4. NITROGEN BASED CARBON QUANTUM DOTS-ENSEMBLES: A MULTICHANNEL SENSOR TO DISCRIMINATE TRACE ELEMENTS

4.1 INTRODUCTION

Essential trace elements develop necessary roles in different physiological functions. Some examples are copper (Cu), cobalt (Co) and molybdenum (Mo). Copper is essential for many living organisms plays an important role in some physiological and pathological processes, such as bone formation and cellular respiration (WANG et al., 2016). Cobalt is a trace element that plays an essential role in the human body. However, excessive intake of Co^{2+} poses a serious threat to human health, such as causing the pulmonary syndrome, neurodegenerative diseases, thyroid damage and cardiac disease (TIAN et al., 2019). Mo functions as an enzymatic cofactor of three enzymes (aldehyde oxidase, sulfite oxidase, xanthine oxidase dehydrogenase), which catalyze the hydroxylation of several substrates (MAYNAR et al., 2018). However, there are many methods have been developed to detect trace elements, such as inductively coupled plasma mass spectroscopy (ICP-MS), atomic absorption spectroscopy/emission spectroscopy, potentiometry and voltammetry. However, these techniques tend to be costly, technically complicated, time-consuming and require expensive instruments. Compared with these methods, fluorescent sensors for metals detection have been widely applied and have attracted increasing attention owing to their simplicity, high sensitivity, good selectivity and rapid response (AN KIM et al., 2020; WANG et al., 2016).

The carbon quantum dots (CQDs) are a new class of fluorescent nanoparticles that have attracted the interest of researchers around the world. These kinds of carbon-based nanomaterial, display biocompatibility, chemical stability, easy synthesis, as well as and surface modifications with different functional groups (DAS et al., 2019; GHOSH et al., 2019; ZHANG et al., 2018). Furthermore, it is possible to adjust their structural compositions to improve spectral properties (SUN et al., 2015), regarding the applications of CQDs in a specific field. Currently, numerous reports have been focused on nitrogen, boron, sulfur, phosphorus or silicon doped-CQDs (MENG et al., 2018; SHI et al., 2019a). By introducing atomic impurities into CQDs their electronic structure can be adjusted, generating *n*-type or *p*-type carriers (MIAO et al., 2020). Therefore, due to the versatility of the CDQs, their applications have broadened in the area of nanomedicine (DONG, 2016b), drug delivery (YANG et al., 2016), bioimaging (GUO et al., 2018), sensing organic molecules (e.g. quinolinic acid in human serum)(SINGH et al., 2018) or inorganics (boric acid and hydroxylamine hydrochloride)(LIU et al., 2017),

metallic ions (eg. Fe^{3+} and Cu^{2+})(CHEN et al., 2017; YADAV et al., 2019) and anionic ions (NO_2^- in water)(ZHANG et al., 2016).

In order, CQDs are considered for the manufacture of sensor arrays. Array sensing detection has numerous advantages, including accuracy, diversity, and the ability to simultaneously detect and distinguish a series of analytes with similar structures and properties. Sensors arrays are based on the "chemical nose-tongue" system defined as an array ensemble that uses synthetic molecules and/or materials to mimic mammalian olfactory systems (GENG; PEVELER; ROTELLO, 2019). Thereby, the same chemical nose can detect several analytes with relatively few sensor elements, generating signals with different patterns from the matrix (WU et al., 2017). Therefore, the interpretation of the nose tongue sign data ensemble is performed using multivariate statistics, for example principal component analysis such as (PCA), linear discriminant analysis (LDA) (BALDWIN et al., 2011; LEGIN; RUDNITSKAYA; NATALE, 2005). In recent years, array-based chemical “nose-tongue” has been mainly developed based on optical signals, and their applications are focused on drug discovery(ASKIM; MAHMOUDI; SUSLICK, 2013), diagnostics (DANIEL E SHUMER, NATALIE J NOKOFF, 2017) and chemical sensing (CHEN et al., 2020b) were used in a sensor array for different analytes including protein (CARNEIRO CRUZ et al., 2019b; FREIRE et al., 2017) and pesticides (CARNEIRO et al., 2019a).

The sensing systems, the discrimination of multi-analyte is usually based on a single-signal strategy. That is, pluralities of optical probes were adopted as the signal receptors, and their sole optical response, i.e., fluorescence or absorbance, towards different analytes are collected for the ensuing discriminations. Therefore, the fabrications of multi probes to provide various spectral responses, which usually are complicated and time-consuming, become the prerequisite for the successful discrimination.

Multidimensional sensing devices have received increasing attention because they are able to read out the target analytes with more than one transduction channel and thus offer increased accuracy and/or diversity. Generally, multidimensional sensing devices are constructed either by mechanically incorporating several different transducers (e.g. colorimetric, mass-sensitive, and capacitive) on a single-chip microsensor system (smart chip), or by chemically integrating multiple reporter units (e.g. fluorescent, absorbing, and electrochemiluminescent) in a molecule (lab-on-a-molecule). Nanoparticles typically used in sensing applications also have the potential to give multidimensional sensory information, such as the dual-channel properties, e.g: conductivity and chemiluminescence. Therefore, fluorescence is potential signal transduction modes for the construction of multimodal sensing

devices.

Herein, we developed a sensing strategy using a multichannel fluorescent sensor array based on two nitrogen-based CQDs to identify and quantify trace ions, such as Co^{2+}, Cu^{2+} and Mo^{4+}. By using our methodology pattern, all metal ions investigated generated a different fluorescence response pattern, which allowed the discrimination at distinct concentrations through a protocol using principal component analysis (PCA) and linear discriminant analysis (LDA).

4.2 OBJECTIVES

4.2.1 General

- To develop multi-channel sensing strategies by using CQDs to identify metallic ions.

4.2.2 Specific

- To evaluate the interaction of CQDs mixture for multi-channel sensor construction;
- To evaluate the interaction of different metalic ions with the CQD mixture.
- Propose a multi-channel Co^{2+} sensing strategy based on the chemical nose-tongue system.

4.3 EXPERIMENTAL

4.3.1 Metallic Ions sensing study

Initially, stock solutions of different metallic ions (Co^{2+}, Cu^{2+}, Mg^{2+}, Mn^{2+}, Fe^{2+}, Mo^{4+} and Zn^{2+}) were separately prepared in Milli-Q water taking into consideration appropriate concentrations. Then, a CQD dispersion was prepared using the two synthesized-doped carbon-based nanoparticles. To assure the concentration of the CQDs, the absorbance of CQDs solution was measured at 350 nm for CQD-NH_2 and 400 nm for CQD-$CONH_2$ and a calibration curve previously built was further used to accurately calculate the concentration. Subsequently, the fluorescence spectrum in the range in two spectra of fluorescence, firstly 380 – 650 nm using 360 nm as the excitation wavelength and second in 440 - 650 nm was again recorded using 420 nm as the excitation wavelength. These spectra were considered the blank. Afterward, the detection of each metallic cation was carried out. To perform this, 10 μL of a stock solution of the target analyte was added into the dispersion previously measured and the fluorescence spectrum was recorded again, regarding the same conditions. This procedure was repeated many times in order to get different concentrations of the metallic cation in contact to the CQDs. Also, six replicates of each experiment were obtained, and Co^{2+}, Cu^{2+}, Mg^{2+}, Mn^{2+}, Fe^{2+}, Mo^{4+} and Zn^{2+} ions were used as a target analyte.

4.3.2 Data treatment

Taking into consideration the protocol described in section 3.1, a raw data matrix of 2 nose-based receptors x 1 metal ion x 8 concentrations x 6 replicates were generated for each target analyte.Therefore, firstly, to investigate the quenching mechanism, the ratio I/I_0(where I and I0 denote the final and initial intensity of the spectrum fluorescence at 450 nm and 515 nm, respectively) was the signal investigated as a function of ion concentration. The curves were fitted using the Stern-Volmer equation and the n parameter was evaluated. Afterward, the whole raw data matrix (2 nose-based receptors x 7 metal ions x 8 metal concentrations x 6 replicates) was further evaluated using principal component analysis (PCA) in the PAST software and linear discriminant analysis (LDA) in the SYSTAT software to identify each target analyte (CARNEIRO et al., 2019b). Also, it is worth to mention in this step,

instead of taking the emission at a single wavelength, the whole spectrum was as interpreted as a fluorescence response. Therefore, the raw data matrix treated includes 480 variables per ensemble of CQDs-NH_2 and CQD-$CONH_2$.

4.4 RESULTS AND DISCUSSION

4.4.1 Doped N-CQDs receptors

Once the CQDs were fully characterized and their properties were revealed in chapter 1, the next step was to find the 'nose'-based receptors to build up a multichannel sensing methodology. First, the CQDs were mixed, observing the concentration of the CQDs in relation to the fluorescent intensity. As a result, standard solutions with defined concentration of each CQDs-N (CQD-N; 1 mg. mL^{-1}) and (CQD-$CONH_2$; 1.8 mg. mL^{-1}) were prepared. Thus, for the construction of the multichannel sensor, the fluorescence intensity was adjusted by mixing the two CQDs-N until obtaining the spectrum of the same fluorescent intensity between the two CQDs.

Figure 37(a) shows the emission behavior of the mixture when excited at different wavelengths, and the mixture of CQD-NH_2 and CQD-$CONH_2$ has demonstrated to have a strong emission at 450 nm when excited at 360 nm, and 515 nm emission when excited at 420 nm. Moreover, taking the optimized ratio conditions into consideration, seven different metal ions solutions (Co^{2+}, Cu^{2+}, Mg^{2+}, Mn^{2+}, Fe^{2+}, Mo^{2+} and Zn^{2+}) were prepared, which were the target analyte chosen to test the proposed sensor strategy.

Figure 37 b-h shows the profile of the set of recorded spectra for each metal ion. It was found that the emissions of the mixture CQDs were quenched by a variety of metal ions with different degree and with the increasing concentration of metal ions, the fluorescent intensity of mixture CQDs decreased. Electron Transfer (PET), Resonance Energy Transfer (RET), Photo-induced Charge Transfer (PCT) and Inner Filter Effect (IFE). PET is a deactivation process involving an internal redox reaction between the excited state of the fluorophore (CQDs) and another species (analytes) able to donate or to accept an electron. In PET, a complex is formed between the electron donor and the electron acceptor. This complex can return to the ground state without emission of a photon, but in some cases exciplex emission is observed. Finally, the extra electron on the acceptor is returned to the electron donor (SUN; LEI, 2017). Resonance energy transfer is another valuable phenomenon for fluorescence sensors. In Forster resonance energy transfer (FRET), an initially excited molecule (donor) returns to the ground state orbital, while simultaneously the transferred energy provides an electron on the acceptor to the excited state. FRET is due to longrange dipolar interactions through excited donor and acceptor.

Figure 37- (a) Emission spectra mixture CQD-N and CQD-$CONH_2$ for varying excitation wavelengths. (b, c, d, e, f, g and h) Emission spectra mixture CQD-N and CQD-$CONH_2$ with the addition ions metalic Co^{2+}, Fe^{2+}, Cu^{2+}, Mn^{2+}, Mg^{2+}, Zn^{2+}, and Mo^{2+}, respectivelly.

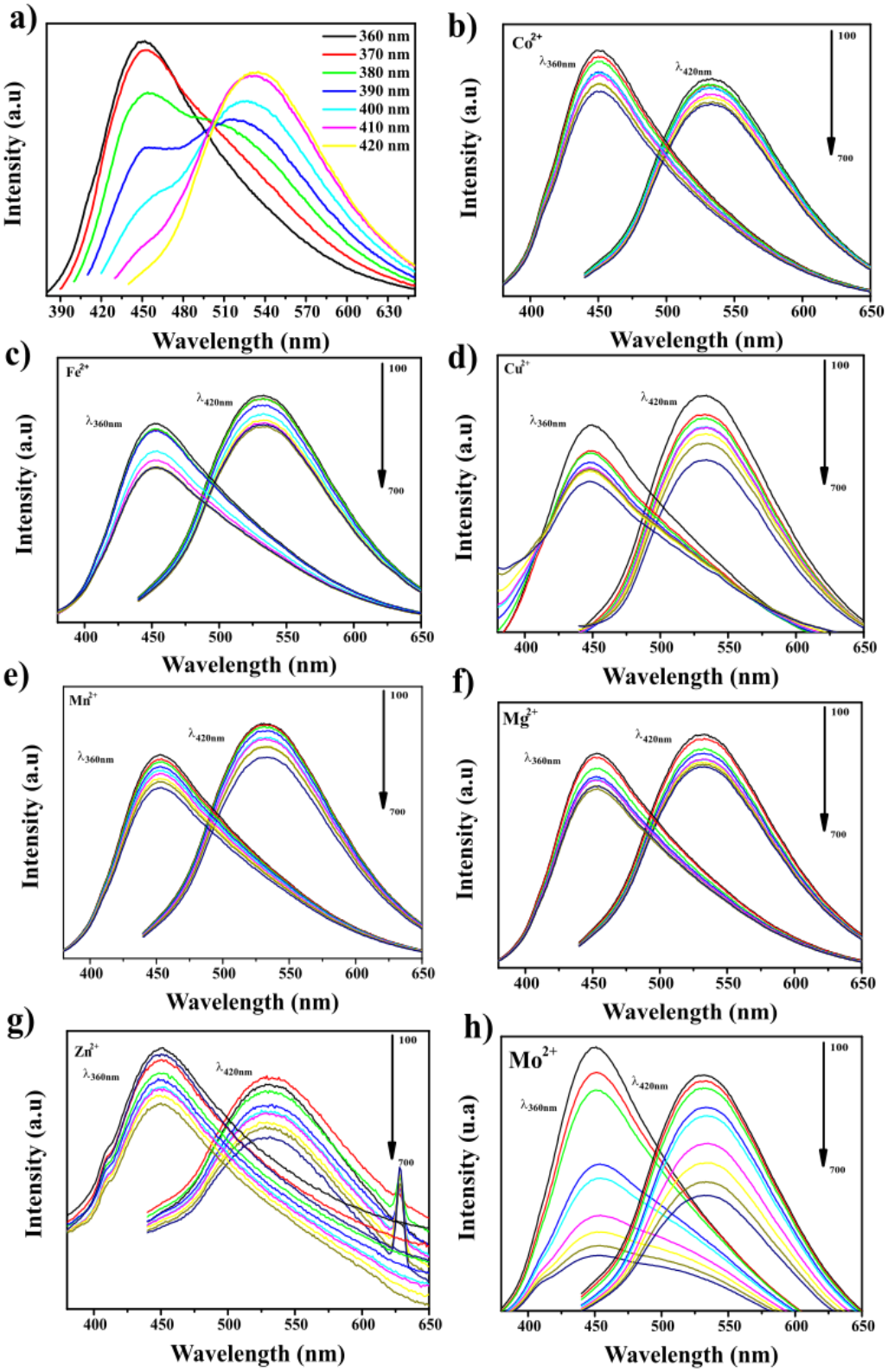

Source: author

According to FRET theory, the rate of energy transfer depends on 1) the relative orientation of the donor and acceptor dipoles, 2) the extent of overlap of fluorescence emission spectrum of the donor (the fluorophore) and absorption spectrum of the acceptor (the analyte), and 3) the distance between the donor and the acceptor. For the energy transfer, it is generally believed that dynamic quenching dominates in the quenching process, where the fluorescence lifetime decreases with increasing of quencher concentrations.

Photo-induced charge transfer (PCT), this mechanism involves the transfer of an electron between electron donor and acceptor functionalities to promote fluorescence. PCT sensors incur partial charge transfer of a fully conjugated π system. In this mechanism, the complexation of donor and acceptor leads to an alteration of electron energy levels, and causes the change of fluorescence signals. PCT sensors show an integrate receptor and fluorophore, while PET sensors have the eléctron donor moiety separated by a spacer from the fluorophore (GAO et al., 2016).

Inner filter effect (IFE), the observed fluorescence intensity is proportional to the intensity of the exciting light, and the quantum yield is somewhat less than that observed for an infinitely dilute solution. This is called as inner filter effect, which may lead to the decrease of the intensity of the excitation at the point of observation, or the observed fluorescence intensity through absorption. Attenuation due to absorption light or absorption of the emitted light are sometimes called the primary or secondary inner filter effects.

Generally, if the inner filter effects are present, the observed fluorescence intensities must be corrected. However, sometimes, inner filter effect has been exploited for sensing applications through fluorescents CQDs. Different from energy transfer, for the inner filter effect based quenching, the fluorescence lifetime is relatively independent on total intensity. According to the structural characterization performed in this work, the CQDs used a probe have positively charged amino groups and negatively charged carbonyls on their surfaces.
Nitrogen atoms have a pair of electrons that can bind to the metal ion to form a complex. Therefore, the different affinity of metal ions with the mixture of CQDs can be explained by the difference in the ability of chelate formation of metal ions with functional groups (amino, carboxyl, hydroxyl etc.) by the PCT mechanism. The responses, Figure 38 (a-e) display the fluorescence responses of CQDs mixture against seven metal ions at different concentrations in the range of 100- 700 μmol L^{-1}.

Figure 38- Relative signal intensity ratio I/I_0 in diferentts concentrations at (a) Co^{2+}, (b) Fe^{2+}, (c) Cu^{2+}, (d) Mo^{4+}, (e) Mn^{2+}, (f) Mg^{2+}, (g) Zn^{2+} according to classical Stern-Volmer formalism.

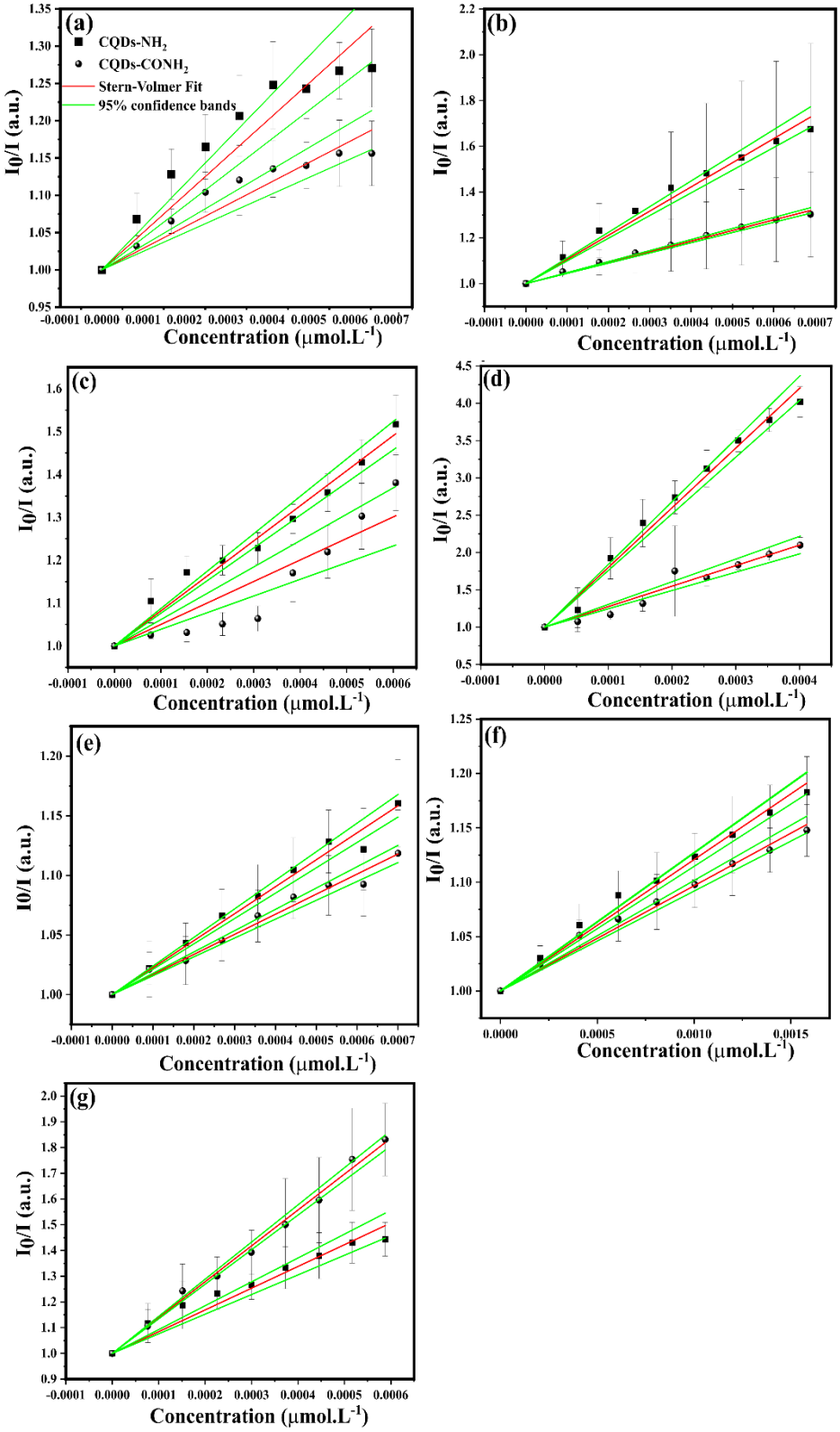

Source: author

As it can be seen, the titration experiments pointed out that each metallic cation was

able to quench both CQDs in the mixture. To properly explain the interaction, as well as the quenching mechanism, it is important to understand the structure of the carbon-based NPs synthesized in this work. In this regard, according to our XPS results, the CQDs have different functional groups on their surfaces. CQD-NH_2 was found to be rich in amine groups, while CQD-$CONH_2$ contain amide groups. Therefore, the presence or absence of these groups on the surface of N doped-CQDs can strongly affect the interactions. In order to obtain a better insight, the titration curves were described using the Stern-Volmer equation (LAKOWICZ, 2006):

$$\frac{I_0}{I} = 1 + K_{SV}\,[C] \tag{8}$$

Where I and I_0 denote the fluorescence intensity recorded with presence and absence of metallic cations, respectively, K_{SV} is the Stern-Volmer quenching constant and $[C]$ is the molar concentration of quencher. Herein, by assuming a linear relationship between $\frac{I_0}{I}$ and $[C]$ with an intercept of 1, K_{SV} can be easily obtained through graphical determination. The magnitude of this constant may help to understand why some metallic cations are more effective to quench the fluorescence intensity than other. Also, to go further, the number n of binding sites on the surface of the CQDs were calculated, utilizing a modified version of the Stern-Volmer equation (BARBERO et al., 2009). The data are summarized in the table 1.

Table 3. Values of λ_{exc}, R^2, K_{SV}, and n for each titration carried out at 298.15K.

Metal	λ_{exc} (nm)	R^2	K_{SV} (Mol.L^{-1})	n
Co	360	0.9839	$4.00 \times 10^2 \pm 9.57$	0.94 ± 0.06
	420	0.9917	$2.50 \times 10^2 \pm 4.34$	0.93 ± 0.04
Fe	360	0.9874	$4.94 \times 10^2 \pm 11.03$	1.08 ± 0.06
	420	0.9706	$2.23 \times 10^2 \pm 7.51$	1.06 ± 0.05
Mn	360	0.9806	$2.42 \times 10^2 \pm 6.27$	0.94 ± 0.03
	420	0.9794	$1.80 \times 10^2 \pm 4.78$	0.87 ± 0.06
Mg	360	0.9841	$2.92 \times 10^2 \pm 6.57$	0.85 ± 0.02
	420	0.9842	$2.34 \times 10^2 \pm 5.12$	0.84 ± 0.02
Mo	360	0.9728	$61.67 \times 10^2 \pm 214.67$	1.80 ± 0.17
	420	0.9129	$17.20 \times 10^2 \pm 115.89$	1.96 ± 0.15
Cu	360	0.9925	$8.07 \times 10^2 \pm 12.85$	0.89 ± 0.04
	420	0.9314	$5.27 \times 10^2 \pm 31.37$	1.51 ± 0.06
Zn	360	0.9935	$12.55 \times 10^2 \pm 19.36$	0.66 ± 0.02
	420	0.9354	$7.61 \times 10^2 \pm 32.11$	0.97 ± 0.03

The R^2 values for all fits were found to be in the range of 0.9129 – 0.9935. This evidences more than 90% of the data variance in y-axis (normalized fluorescence intensity) can be explained by the x-axis (quencher concentration) using a linear model. So, it is fair to assume

there is a strong linear relationship between $\frac{I_0}{I}$ and $[C]$. However, the deviation of linearity may point out for the presence of dynamic (collisional) or static (binding-related) quenching mechanism (FRAIJI; HAYES; WERNER, 1992). Once it is not possible to determine which one from a single linear Stern-Volmer plot, we carried out titrations at different temperatures (298.15 and 310.15 K) for Co^{2+}, Cu^{2+}, Fe^{2+} and Mo^{4+} ions. In this sense, to identify the mechanism that better defines the interaction between CQDs and metallic cations, it is fundamental to know if quenching is dynamic, the value of K_{SV} should increase.

On the other hand, if static is the mechanism, K_{SV} should decrease by increasing the temperature. In this sense, the predominant quenching mechanism for Co^{2+} and Fe^{2+} ions was found to be dynamic, while for Cu^{2+} and Mo^{4+} ions the static was the one observed. Additionally, *n* values for Fe^{2+}, Zn^{2+}, Mg^{2+}, Mn^{2+} and Co^{2+} are near to 1.0 for both CQDs, which indicates there is one empty site on the CQDs surface to intereact with the mentioned metals. However, the situation is different when Cu^{2+} ions are used as a quencher. In this case, the presence of amide groups on the surface of the CQDs seems to increase the number of binding sites for Cu^{2+} ions, since the *n* values were found to be 0.89 ± 0.04 and 1.51 ± 0.06 for CQD-NH_2 and CQD-$CONH_2$, respectively.

Additionally, $n \approx 2$ was observed for Mo^{4+} ions, when used as quencher for both CQDs. Compared to the other metallic cations, Mo^{4+} ions is the one with highest of K_{SV} value. Taking into consideration this ion as the quencher, the values found were $61.67 \times 10^2 \pm 214.67$ and $17.20 \times 10^2 \pm 115.89$ L mol^{-1} for for CQD-NH_2 and CQD-$CONH_2$, respectively. The other ions, when used to quench the fluorescence intensity of the same CQDs, the K_{SV} values were found to be in the range 1.80×10^2 - 12.55×10^2 L mol^{-1}. Once this constant point out for the interaction between the CQDs surface and the metallic cations, it is fair to assume the Mo^{4+} ions are the ones presenting the strongest interaction. This may be explained based on the electronic configuration of the cation, since the Mo^{4+} is the ion with the highest amount of empty d-orbitals.

In order to deppen further our study, the metal ions fingerprint response pattern of the different metal ions concentrations (100-700 μmol L^{-1}) in the sensor array were obtained. To accomplish this, the signal change value was defined as (I/I_0), where I and I_0 are the fluorescent intensity (440 nm under excitation wavelength at 360 nm and 510 nm under excitation wavelength at 420 nm) of the solution. As shown in Figure 39, for the same CQD receptor, the values (I/I_0) varied with the addition of different metal ions, it can be clearly observed that CQDs are sensitive to molybdenum metal ions.

Figure 39- Fingerprints of eight concentration seven metal ions based on the fluorescence response patterns of the two wavelength CQD multichannel sensor array.

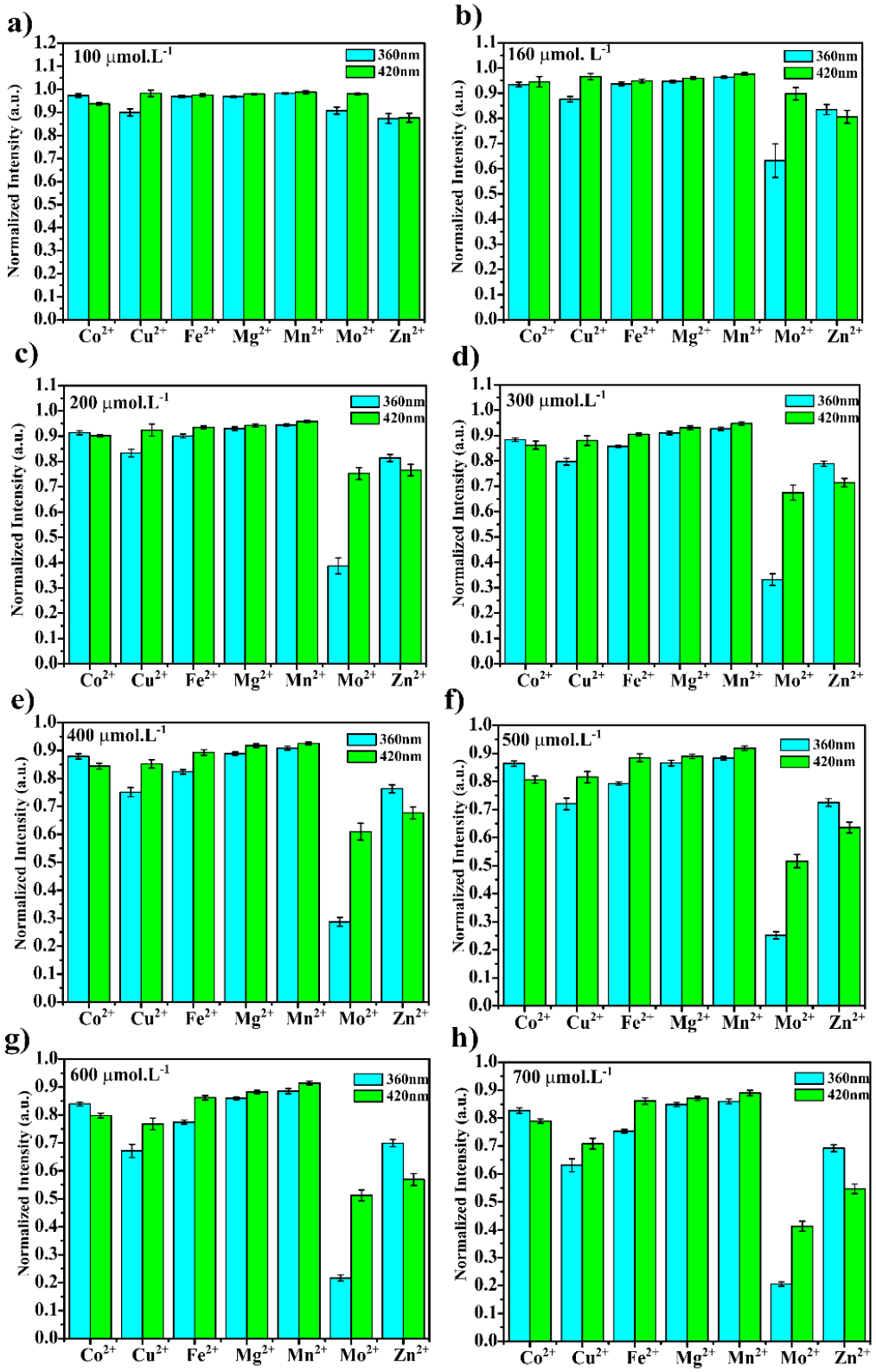

Source: Author

It is important to highlight that for the metallic ions considered as Co^{2+}, Cu^{2+} and Zn^{2+} features have different fingerprint, that is, there are different interactions between the CQDs. However, it is believed that the functional groups on the surface of the CQDs function as bases of electron donating species lewis, whereas metal ions function as electron receptor species lewis acids.

So, we can consider that we have different metal ion species, so, the formation of different complexes is taking place causing the quenching or enhancement of the fluorescence intensity. Finally, the value of the fluorescence intensity difference was processed through normalization and the fingerprint of each metal ion was obtained, which contained all the information of the CQDs that responded to these metal ions. From these fingerprints, we also obtained some important information about the sensor array. Therefore, in the present study, N-doped CQDs have multiple emissions and with the addition of metal ions, the physical interactions between CQDs and different species of metallic ions lead to changes in the surface properties of CQDs, which ultimately results in changes. The various fluorescence variations with the addition of different species of metal ions provide the basis of the dual signal model matrix sensor for differentiation and identification of metal ions, as illustrated in Figure 40.

Figure 40- Schematic illustration of dual-response sensor array based on CQD-N and CQD-$CONH_2$.

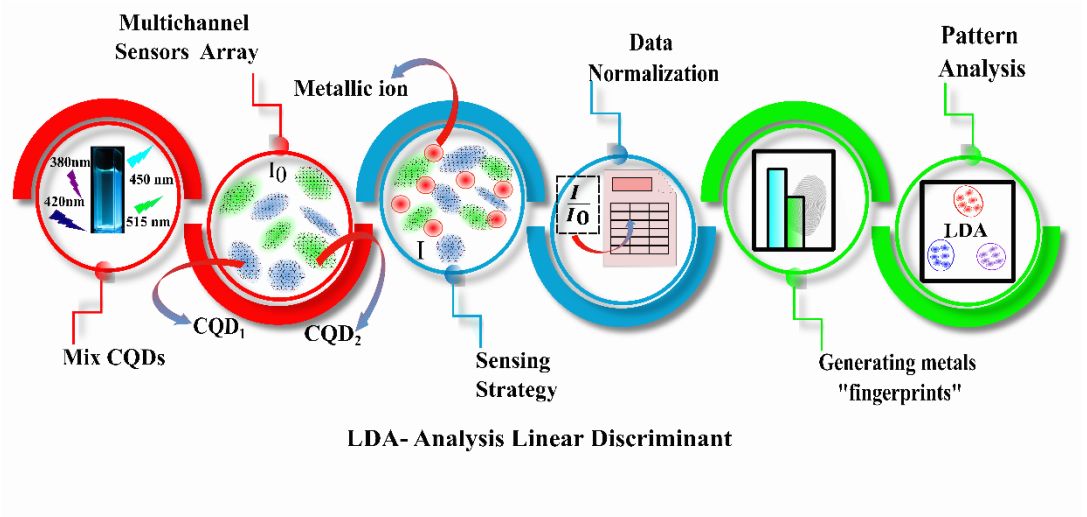

Source: Author

As shown in Figure 41, the fluorescence response pattern of each metal ion, indicating the practicality of discrimination using the multichannel sensor. Discrimination of metal ions was achieved by statistical analysis. For each metal ion, fluorescence responses

against the sensor array were tested six times in parallel, yielding a matrix 2 wavelength × 7 replicated metal ion concentrations × 6 replicates. To investigate the fluorescence response pattern of the multichannel sensor array against different target metal ion concentrations. Data processing was performed PCA (Principal component analysis) has been widely used to evaluate the pattern recognition capability of developed sensor arrays. This is usually an unsupervised statistical treatment used to reduce a multidimensional dataset into a new orthogonal dimension set, which is performed by calculating orthogonal eigen vectors (principal components, PCs) located in the direction of maximum variation within the dataset, followed by classical LDA to transform the matrix into canonical factors.

Figure 41- (a) Canonical scores for response patterns captured by the LDA for 100-700 mmol L^{-1} concentration range for Cu^{2+}. (b) Canonical scores for response patterns captured by the LDA for 100-700 μmol L^{-1}concentration range for Fe^{2+}.

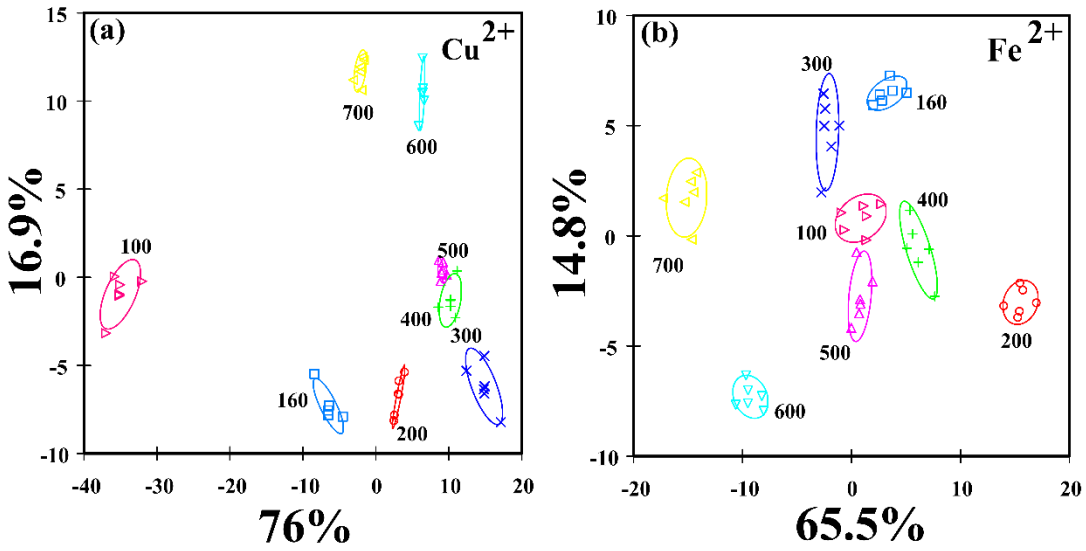

Source: Author

Six replicates were tested for each Cu^{2+} metal ion concentration sample and two canonical factors were generated. The first canonical factor accounts for 76.0% of the variability in the data, while the second subsequent canonical factor corresponds to 16.9%. The first two LDA contributions 92.9% of the total and therefore were applied to plot the LDA graph (figure 41a). It is possible to see that the clusters are on the more positive side as the concentration increases, indicating that greater separability occurs in larger dimensions, clearly differentiating 8 different concentrations of this metallic ions. The 48 training cases were

separated into 8 respective groups with 100% accuracy according to the classification matrix derived from subset analysis of the data sets.

Figure 41b shows the graph of the two main canonical factors for Fe^{2+} concentrations. The first canonical factor accounts for 65.5% of the variability in the data, while the second subsequent canonical factor corresponds to 14.8%. The first two LDA contributions were 80.3% of the total and therefore were applied to chart the LDA. No obvious grouping is observed on the chart, indicating that the LDA chart can clearly differentiate 8 different concentrations of this metal ion in the 100-700 $\mu mol.L^{-1}$ range. The training cases were separated into 8 respective groups with 100% accuracy according to the classification matrix derived from subset analysis of the data sets.

Figure 42- (a) Canonical scores for response patterns captured by the LDA for 100-700 $\mu mol.L^{-1}$ concentration range for Mg^{2+}. (b) Canonical scores for response patterns captured by the LDA for 100-700 $\mu mol.L^{-1}$ concentration range for Zn^{2+}.

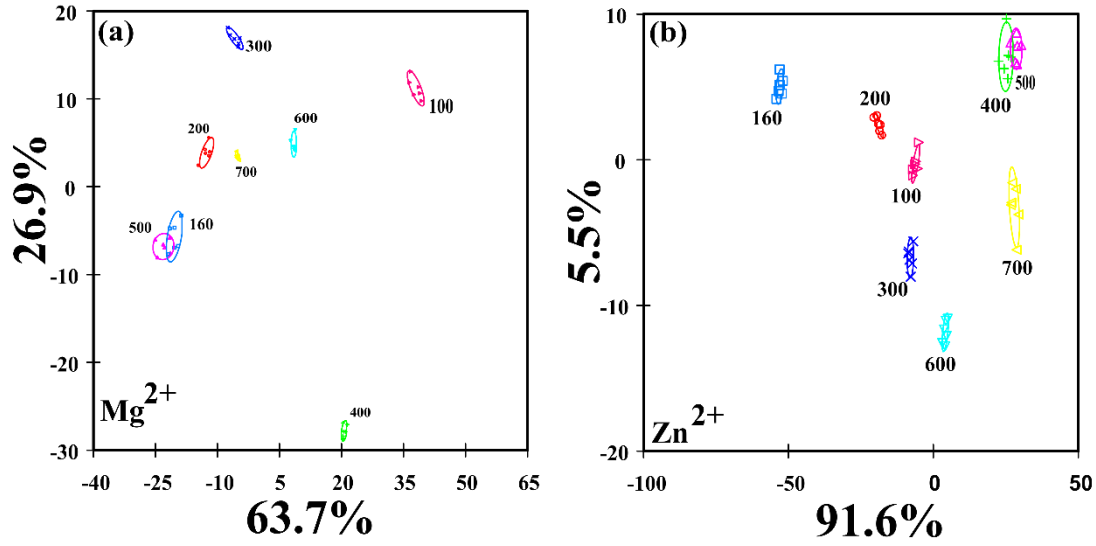

Source: Author

Figure 42a shows the graph of the two main canonical factors for Mg^{2+} concentrations. The first canonical factor accounts for 63.7% of the variability in the data, while the second subsequent canonical factor corresponds to 26.9%. The first two LDA contributions were 90.6% of the total and therefore were applied to the LDA chart. There are two concentrations of 160 $\mu mol.L^{-1}$ and 500 $\mu mol.L^{-1}$ clustering, most concentrations are located in the upper dimension of the graph indicating that in the lower dimensions may not discriminate the concentrations, so it is possible to observe in the graph, indicating that the LDA graph can

clearly differentiate 6 different concentrations of this metal ion in the 100-700 μmol.L^{-1} range. The 48 training cases were separated into 8 respective groups with 75% accuracy, according to the classification matrix derived from subset analysis of the data sets. However, in figure 42b shows the graph of the two main canonical factors for Zn^{2+} concentrations. The first canonical factor accounts for 91.6% of the variability in the data, while the second subsequent canonical factor corresponds to 5.5%. The first two contributions from the LDA were 97.1%. It is possible to observe in the graph that There are two concentrations of 400 μmol.L^{-1} and 500 μmol.L^{-1} of grouped, most of the concentrations are located in the upper and lower positive and negative dimension of the first canonical factor of the graph, indicating that in the lower dimensions of the second canonical factor may not discriminate concentrations, so it can be observed that in the LDA graph it can clearly differentiate 6 different concentrations of this metal ion in the range of 100-700 μmol.L^{-1}. The 48 training cases were separated into 8 respective groups with 75% accuracy, according to the classification matrix derived from subset analysis of the data sets.

Figure 43- (a) Canonical scores for response patterns captured by the LDA for 100-700 μmol.L^{-1} concentration range for Co^{2+}. (b) Canonical scores for response patterns captured by the LDA for 100-700 μmol.L^{-1} concentration range for Mn^{2+}.

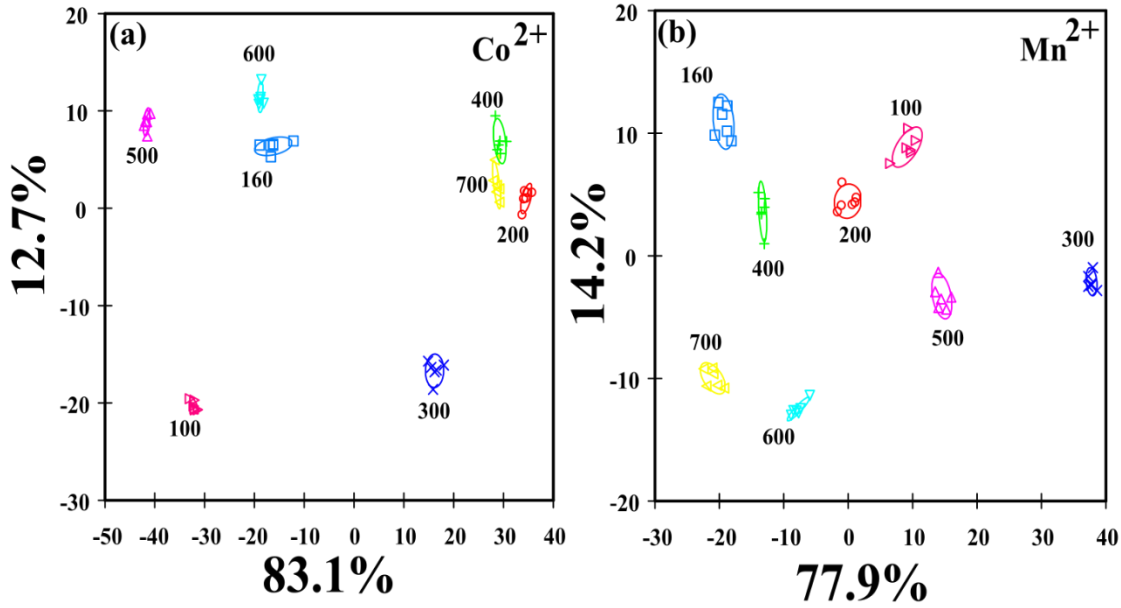

Source: Author

In addition, Co^{2+} metal ion concentration samples generated two canonical factors. The first canonical factor accounts for 83.1% of the variability in the data, while the second subsequent canonical factor corresponds to 12.7%. The first two LDA contributions were 95.8% of the total and therefore were applied to plot the LDA graph (figure 43a). It is possible to observe that the 400 μmol.L^{-1} and 700 μmol.L^{-1} concentrations may interfere with future analyses. However, it can be seen that most clusters are on the more positive side of the chart, indicating that greater separability occurs in larger dimensions. Thus, it is possible to clearly differentiate 8 different concentrations and the 48 training cases were separated into 8 respective groups with 100% accuracy. However, in the Mn^{2+} training samples 48 were separated into 8 respective groups, with 100% accuracy. The first two canonical factors correspond to about 92.1% of the total variability and the first canonical factor corresponds to about 77.9% of variance and the second canonical factor corresponds to 14.2% of variance, therefore, they were applied to plot the LDA graph (figure 43b). No obvious grouping is observed on the chart. However, once again, LDA chart can clearly differentiate 8 different concentrations of these metal ions.

Figure 44- Canonical scores for response patterns captured by the LDA for 100-700 μmol.L^{-1} concentration range for Mo^{2+}.

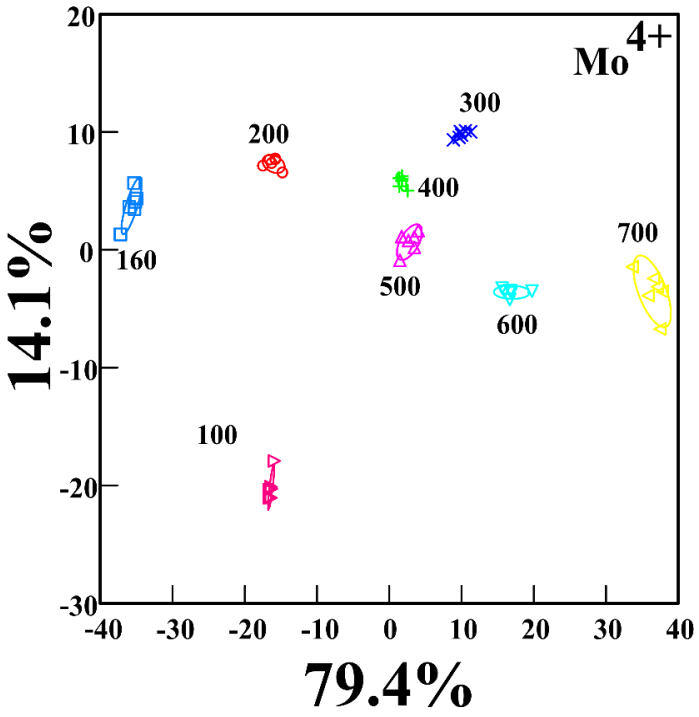

Source: Author

Figure 44 shows the 2D graph of the canonical factors of the Mo^{4+} metal ion concentration sample. The first canonical factor accounts for 79.4% of the variability in the data, while the second subsequent canonical factor corresponds to 14.1%. The first two LDA contributions 93.5%. No obvious grouping is observed in the graph, but it is possible to see that clusters are on the more positive side as the concentration increases, indicating in larger dimensions it is possible to better discriminate the concentrations. In addition, the LDA graph can clearly differentiate 8 different concentrations of these metal ions in the range of 100-700 $\mu mol.L^{-1}$. The 48 training cases were separated into 8 respective groups with 100% accuracy.

Figure 45- Canonical score plot of CQDs-N and CQD-$CONH_2$ without amino acids for the discrimination of nine metal ions at 100 $\mu mol.L^{-1}$ concentration.

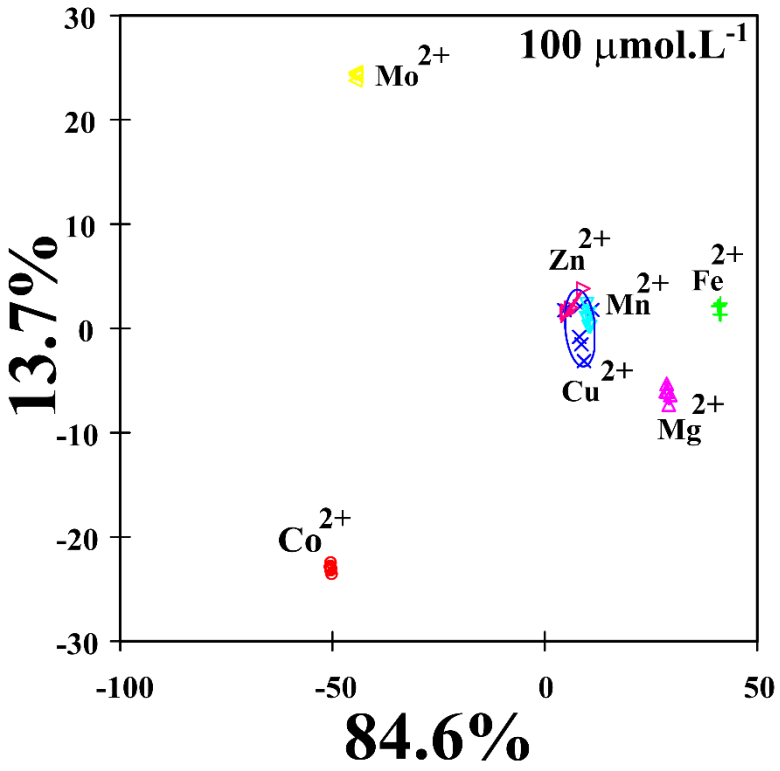

Source: Author

The canonical score graph of seven metal ions at a concentration of 4.98 ppm against the CQD-N and CQD-$CONH_2$ sensor array generated two canonical factors using the LDA in figure 45. The first canonical factor accounts for 84.6 % of the variability in the data, while the second subsequent canonical factor corresponds to 13.7%. The first two contributions from the LDA were 98.3% of the total. Only four metal ions (Co^{2+}, Mo^{2+}, Fe^{2+} and Mg^{2+}) at

4.98 ppm can be identified, so the training matrix was separated into 8 groups with 57% accuracy. When we increase the concentration to 300 μmol.L^{-1}, figure 10, it is possible to identify all metal ions. The first canonical factor, figure 10, accounts for 61.8% of the variability in the data, while the second subsequent canonical factor corresponds to 33.3%. The first two LDA contributions were 95.1% of the total, the training matrix was separated into 8 groups with 100% accuracy.

Figure 46- Canonical score plot of CQDs-N and CQ-CONH$_2$ without amino acids for the discrimination of nine metal ions at 300 mmol.L^{-1} concentration.

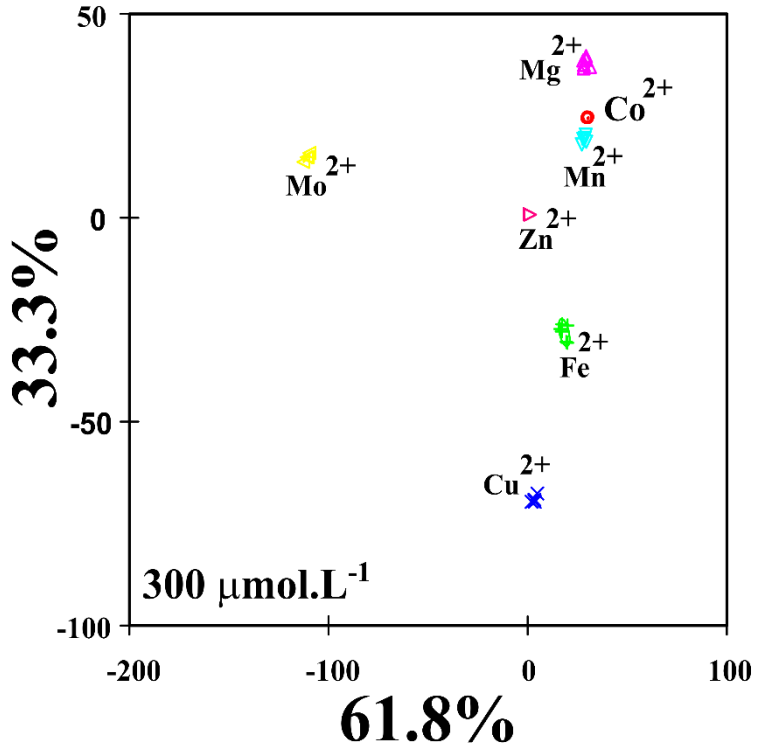

Source: Author

Figure 46 represents the graph of the two main canonical factors at a concentration of 700 μmol.L^{-1}. The first canonical factor corresponds to 79.9% of variability and the second canonical factor corresponds to 19.2% of variability, the two canonical factors contribute 99.1% of total variance. It is possible to observe that in this concentration were identified 4 metal ions (Mo^{2+}, Cu^{2+}, Zn^{2+} and Co^{2+}), the training matrices formed 8 groups with 50% accuracy.

Figure 47- Canonical score plot of CQDs-N and CQ-CONH$_2$ without amino acids for the discrimination of nine metal ions at 700 μmol.L^{-1} concentration.

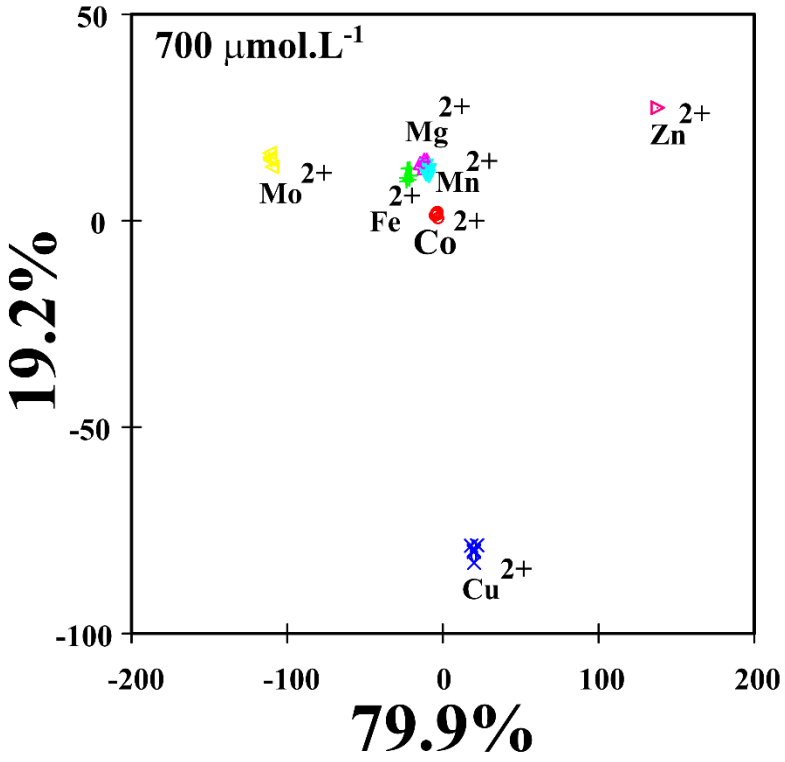

Source: Author

The rating matrix showed that the accuracy of the rating of seven metal ions was improved from 57% at 100 μmol.L^{-1}, figure 9, to 100% at 100 μmol.L^{-1}, figure 10. Notably, all seven metal ions at 100 μmol.L^{-1}, figure 10, were separated with 100% accuracy. However, when we are at 700 μmol.L^{-1} concentrations the separability accuracy is around 50%, figure 47. However, figure 10 and 11 have shown that trace metal ions Cu^{2+}, Mo^{2+} and Co^{2+} can be easily discriminated, but in Concentrations above 700 μmol.L^{-1} Co^{2+} may be interfered with other metal ions. At concentrations of 100 μmol.L^{-1} Co^{2+} and Mo^{2+} are easily discriminated. Thus, we easily conclude that the CQD-N and CQD-$CONH_2$ multichannel sensor array is effective in discriminating seven metal ions at 300 μmol.L^{-1}, but its discriminatory power is limited at concentrations of 100 μmol.L^{-1} and 700 μmol.L^{-1}.

4.5 CONCLUSION

In summary, we present a simple and easy strategy for building a multichannel sensor strategy, based on the fluorescence of CQDs doped with nitrogen, to quantify and identify analytes. As a proof of concept, metals were the chosen analytes to prove the methodology due to the importance of this analyte for the human health. In this regard, the nose-based multichannel sensor was able to provide the concentration, as well as the identity of the group of metals studied (Co^{2+}, Cu^{2+}, Mg^{2+}, Mn^{2+}, Fe^{2+}, Mo^{4+} and Zn^{2+}) in the range about 100, 300 and 700 $\mu mol.L^{-1}$. Interestingly, the titration curves at differente temperatures revealed the sensing mechanism through dynamic quenching for Co^{2+} and Fe^{2+} ions, while static quenching was observed for Cu^{2+} and Mo^{4+} ions. This may be related to the number of available sites on the surface of the both CQDs to interact. Additionally, the data from the titration curves were treated using PCA and LDA algorithms. The results revealed our nose-based strategy using the multichannel sensors was able to discriminate the metal ions at different concentrations. Interestingly, Mo^{4+} ions were easily identified by the probes no matter the concentration investigated. Therefore, the presence of two empty sites on the surface of the CQDs to interact with this metal ion is the key to explain this result. Finally, our multichannel sensing appears as an alternative for sensing trace elements in the field of biochemistry. It can also be used in sports as an anti-doping test, for sensing trace elements that improve athletes' performance. However, the present sensor has a potential application to discriminate molybdenum ions.

REFERÊNCIAS

A. ARBER, D.; ORAZI, A. The Updated WHO Classification Of Hematological Malignancies: The 2016 revision to the WHO classification of myeloid neoplasms and acute leukemia. **The Blood Journal**, v. 2, n. 20, p. 58–71, 2016.

ABREU, D. S. *et al.* SAM of Gliotoxin on Gold: A Natural Product Platform for Sugar Recognition based on the Immobilization of Canavalia brasiliensis lectin (ConBr). **Electrochimica Acta**, v. 241, p. 116–123, 2017.

ADÈS, L.; ITZYKSON, R.; FENAUX, P. Myelodysplastic syndromes. **The Lancet**, v. 383, n. 9936, p. 2239–2252, 2014.

ALGETHAMI, F. K. *et al.* Chemical fingerprinting and quantitative monitoring of the doping drugs bambuterol and terbutaline in human urine samples using ATR-FTIR coupled with a PLSR chemometric tool. **RSC Advances**, v. 10, n. 12, p. 7146–7154, fev. 2020.

ALI, M. *et al.* Microwave-assisted ultrafast in-situ growth of N-doped carbon quantum dots on multiwalled carbon nanotubes as an efficient electrocatalyst for photovoltaics. **Journal of Colloid And Interface Science**, 2020.

AN KIM, P. *et al.* A chelated-type colorimetric chemosensor for sensing Co2+ and Cu2+. **Inorganica Chimica Acta**, v. 505, n. December 2019, p. 119502, 2020.

ASKIM, J. R.; MAHMOUDI, M.; SUSLICK, K. S. Optical sensor arrays for chemical sensing: the optoelectronic nose. **Chemical Society Reviews**, v. 42, n. 22, p. 8649, 2013.

AYAZ AHMED, K. B.; MOHAMMED, A. S.; VEERAPPAN, A. Interaction of sugar stabilized silver nanoparticles with the T-antigen specific lectin, jacalin from Artocarpus integrifolia. **Spectrochimica Acta - Part A: Molecular and Biomolecular Spectroscopy**, v. 145, p. 110–116, 2015.

BAI, J. *et al.* Coal Tar Pitch Derived Nitrogen-doped Carbon Dots with Adjustable Particle Size for Photocatalytic Hydrogen Generation. **Carbon**, n. Iii, p. 124658, out. 2020.

BAI, L. Nitrogen-doped carbon dots derived from electrospun carbon nanofibers for Cu (II) ion. p. 1812–1817, 2019.

BALDWIN, E. A. *et al.* Electronic Noses and Tongues: Applications for the Food and Pharmaceutical Industries. p. 4744–4766, 2011.

BARAUNA, S. C. *et al.* Antidepressant-like effect of lectin from Canavalia brasiliensis (ConBr) administered centrally in mice. **Neurochemical Research**, v. 96, n. 2, p. 276–282, 2017.

BARBERO, N. *et al.* A study of the interaction between fluorescein sodium salt and bovine serum albumin by steady-state fluorescence. **Dyes and Pigments**, v. 80, n. 3, p. 307–313, 2009.

BATISTA, J. E. C. *et al.* Plant lectins ConBr and CFL modulate expression toll-like receptors,

pro-inflammatory cytokines and reduce the bacterial burden in macrophages infected with Salmonella enterica serovar Typhimurium. **Phytomedicine**, v. 25, p. 52–60, 2017.

BELHUMEUR, P. N.; HESPANHA, J. P.; KRIEGMAN, D. J. Eigenfaces vs. Fisherfaces: recognition using class specific linear projection. **IEEE Transactions on Pattern Analysis and Machine Intelligence**, v. 19, n. 7, p. 711–720, jul. 1997.

BHATI, A. Sunlight-induced photoreduction of Cr (VI) to Cr (III) in wastewater by nitrogen-phosphorus-doped carbon dots. **npj Clean Water**, n. October 2018, p. 1–9, 2019.

BIN, B. *et al.* Fluorescent carbon dots functionalization. **Advances in Colloid and Interface Science**, v. 270, p. 165–190, 2019.

BORUAH, A. *et al.* Blue-emitting fluorescent carbon quantum dots from waste biomass sources and their application in fluoride ion detection in water. **Journal of Photochemistry and Photobiology B: Biology**, v. 209, p. 111940, ago. 2020.

CAMPOS, M. P.; REIS, M. S. Data preprocessing for multiblock modelling – A systematization with new methods. **Chemometrics and Intelligent Laboratory Systems**, v. 199, p. 103959, abr. 2020.

CANAVALIA, K. ConBr, the Lectin from. p. 600–613, 2019.

CAO, N. *et al.* A fluorescent sensor array based on silver nanoclusters for identifying heavy metal ions. **Microchemical Journal**, v. 159, p. 105406, 2020.

CARNEIRO, S. V *et al.* Sensors and Actuators B : Chemical Sensing strategy based on Carbon Quantum Dots obtained from ribo fl avin for the identi fi cation of pesticides. v. 301, n. September, 2019a.

CARNEIRO, S. V. *et al.* Sensing strategy based on Carbon Quantum Dots obtained from riboflavin for the identification of pesticides. **Sensors and Actuators, B: Chemical**, v. 301, dez. 2019b.

CARNEIRO CRUZ, A. A. *et al.* Fluorescence Based Platform to Discriminate Protein Using Carbon Quantum Dots. **ChemistrySelect**, v. 4, n. 19, p. 5619–5627, maio 2019a.

CARNEIRO CRUZ, A. A. *et al.* Fluorescence Based Platform to Discriminate Protein Using Carbon Quantum Dots. **ChemistrySelect**, v. 4, n. 19, p. 5619–5627, maio 2019b.

CAVADA, B. S. *et al.* ConA-like lectins: High similarity proteins as models to study structure/biological activities relationships. **International Journal of Molecular Sciences**, v. 20, n. 1, 2019.

CAVADA, B. S. et al. Molecular dynamics and binding energy analysis of Vatairea guianensis lectin: a new tool for cancer studies. **Journal of Molecular Modeling**, v. 26, n. 2, 2020.

CHAHAL, S.; YOUSEFI, N.; TUFENKJI, N. Green Synthesis of High Quantum Yield Carbon Dots from Phenylalanine and Citric Acid: Role of Stoichiometry and Nitrogen Doping. **ACS Sustainable Chemistry and Engineering**, v. 8, n. 14, p. 5566–5575, abr. 2020.

CHANDRA, S. *et al.* Synthesis of highly fluorescent nitrogen and phosphorus doped carbon dots for the detection of Fe 3 + ions in cancer cells. n. March 2015, p. 81–87, 2016.

CHEN, D. *et al.* Intense multi-state visible absorption and full-color luminescence of nitrogen-doped carbon quantum dots for blue-light-excitable solid-state-lighting. p. 9027–9035, 2016.

CHEN, D. *et al.* Multi-color fluorescent carbon dots for wavelength-selective and ultrasensitive Cu2+sensing. **Journal of Alloys and Compounds**, v. 701, p. 75–81, 2017.

CHEN, L. *et al.* Construction of multi-channel fluorescence sensor array and its application for accurate identification and sensitive quantification of multiple metal ions. **Sensors and Actuators B: Chemical**, v. 303, p. 127277, 2020a.

CHEN, Z. H. *et al*. Design of smart chemical 'tongue' sensor arrays for pattern-recognition-based biochemical sensing applications. **TrAC - Trends in Analytical Chemistry**, v. 124, p. 115794, 2020b.

CHEN, Z.-H. *et al.* Design of smart chemical 'tongue' sensor arrays for pattern-recognition-based biochemical sensing applications. **TrAC Trends in Analytical Chemistry**, v. 124, p. 115794, 2020c.

CHENG, H. *et al.* Highly stable and selective measurement of Fe 3 + ions under environmentally relevant conditions via an excitation-based multiwavelength method using N , S-doped carbon dots. **Environmental Research**, v. 170, n. October 2018, p. 443–451, 2019.

COELHO, L. C. B. B. *et al.* Lectins, Interconnecting Proteins with Biotechnological/Pharmacological and Therapeutic Applications. **Evidence-based Complementary and Alternative Medicine**, v. 2017, 2017.

CRUZ, A. A. C. *et al.* Optical Sensing Strategy Based on Carbon Quantum Dots. Em: **Reference Module in Biomedical Sciences**. [s.l.] Elsevier, 2021.

DAI, B. *et al.* Synthesis and formation mechanism of s-doped carbon dots from low-molecule-weight organics. **Journal of Luminescence**, v. 190, n. April, p. 108–114, 2017.

DANG, D. K. *et al.* Dyes and Pigments Pyromellitic acid-derived highly fluorescent N-doped carbon dots for the sensitive and selective determination of 4-nitrophenol. **Dyes and Pigments**, v. 165, n. February 2018, p. 327–334, 2019.

DANIEL E SHUMER, NATALIE J NOKOFF, N. P. S. Array-based sensing using nanoparticles: an alternative approach for cancer diagnostics. **Physiology & behavior**, v. 176, n. 12, p. 139–148, 2017.

DAS, P. *et al.* Heteroatom doped blue luminescent carbon dots as a nano-probe for targeted cell labeling and anticancer drug delivery vehicle. v. 237, n. May, 2019.
DEVI, P.; SAINI, S.; KIM, K. H. The advanced role of carbon quantum dots in nanomedical applications. **Biosensors and Bioelectronics**, v. 141, n. March, p. 111158, 2019.

DHAULANIYA, A. S. *et al.* Qualitative and quantitative evaluation of corn syrup as a potential added sweetener in apple fruit juices using mid-infrared spectroscopy assisted chemometric modeling. **LWT**, v. 131, p. 109749, jun. 2020.

DING, H.; WEI, J. S.; XIONG, H. M. Nitrogen and sulfur co-doped carbon dots with strong blue luminescence. **Nanoscale**, v. 6, n. 22, p. 13817–13823, 2014.

DONG, C. Phosphorus and Nitrogen Dual-Doped Hollow Carbon Dot as a Nanocarrier for Doxorubicin Delivery and Biological Imaging. 2016a.

DONG, C. Phosphorus and Nitrogen Dual-Doped Hollow Carbon Dot as a Nanocarrier for Doxorubicin Delivery and Biological Imaging. 2016b.

DONG, Y. *et al.* Blue luminescent graphene quantum dots and graphene oxide prepared by tuning the carbonization degree of citric acid. **Carbon**, v. 50, n. 12, p. 4738–4743, 2012.

ELSONBATY, A. *et al.* Analysis of quinary therapy targeting multiple cardiovascular diseases using UV spectrophotometry and chemometric tools. **Spectrochimica Acta - Part A: Molecular and Biomolecular Spectroscopy**, v. 238, p. 118415, set. 2020.

FAHEINA-MARTINS, G. V. *et al.* Antiproliferative effects of lectins from Canavalia ensiformis and Canavalia brasiliensis in human leukemia cell lines. **Toxicology in Vitro**, v. 26, n. 7, p. 1161–1169, 2012.

FAN, H. *et al.* **Food waste as a carbon source in carbon quantum dots technology and their applications in food safety detection**. **Trends in Food Science and Technology**Elsevier Ltd, , jan. 2020.

FANG, J.; ZHUO, S.; ZHU, C. Fluorescent sensing platform for the detection of p - nitrophenol based on Cu- doped carbon dots. **Optical Materials**, v. 97, n. September, p. 109396, 2019.

FENG, Q.; XIE, Z.; ZHENG, M. Colour-Tunable Ultralong-Lifetime Room Temperature Phosphorescence with External Heavy-Atom Effect in Boron-Doped Carbon Dots. **Chemical Engineering Journal**, p. 127647, nov. 2020.

FERREIRA, M. M. C. **Quimiometria: conceitos, métodos e aplicações**. [s.l.] Editora da Unicamp, 2015.

FRAIJI, L. K.; HAYES, D. M.; WERNER, T. C. Static and dynamic fluorescence quenching experiments for the physical chemistry laboratory. **Journal of Chemical Education**, v. 69, n. 5, p. 424–428, 1992.

FREIRE, R. M. *et al.* NH<inf>2</inf>-rich Carbon Quantum Dots: A protein-responsive probe for detection and identification. **Sensors and Actuators, B: Chemical**, v. 1, p. 1–8, 2017.

FREIRE, R. M. *et al.* NH2-rich Carbon Quantum Dots: A protein-responsive probe for detection and identification. **Sensors and Actuators B: Chemical**, v. 255, n. Part 3, p. 2725–2732, 2018.

FU, X. et al. Sensors and Actuators B : Chemical Rapid and universal detection of ovalbumin based on N , O , P-co-doped carbon dots-fluorescence resonance energy transfer technology. v. 269, p. 278–287, 2018.

GAO, X. et al. Carbon quantum dot-based nanoprobes for metal ion detection. **Journal of Materials Chemistry C**, n. December, 2016.

GAO, Y. *et al.* Sensor array based on single carbon quantum dot for fluorometric differentiation of all natural amino acids. **Microchimica Acta**, v. 186, n. 12, p. 1–9, dez. 2019.

GEANĂ, E.-I. *et al.* Wine varietal discrimination and classification using a voltammetric sensor array based on modified screen-printed electrodes in conjunction with chemometric analysis. **Microchemical Journal**, v. 159, p. 105451, 2020.

GENG, Y.; PEVELER, W. J.; ROTELLO, V. M. Array-based " Chemical Nose " Sensing in Diagnostics and Drug Discovery Angewandte. p. 5190–5200, 2019.

GHOLAMI, M. *et al.* A new nano biosensor for maitotoxin with high sensitivity and selectivity based fluorescence resonance energy transfer between carbon quantum dots and gold nanoparticles. **Journal of Photochemistry and Photobiology A: Chemistry**, v. 398, n. April, p. 112523, 2020.

GHOSH, S. *et al.* Dendrimer functionalized carbon quantum dot for selective detection of breast cancer and gene therapy. **Chemical Engineering Journal**, v. 373, n. April, p. 468–484, 2019.

GONÇALVES, H. *et al.* Hg(II) sensing based on functionalized carbon dots obtained by direct laser ablation. **Sensors and Actuators B: Chemical**, v. 145, n. 2, p. 702–707, 2010.

GREENBERG, P. L. *et al.* Revised international prognostic scoring system for myelodysplastic syndromes. **Blood**, v. 120, n. 12, p. 2454–2465, 2012.

GUIMARÃES, L. L. *et al.* Multivariate Method Based on Raman Spectroscopy for Quantification of Dipyrone in Oral Solutions. **Journal of Spectroscopy**, v. 2018, p. 3538171, 2018.

GUO, S. *et al.* Highly Selective Red-Emitting Fluorescent Probe for Imaging Cancer Cells in Situ by Targeting Pim - 1 Kinase. 2018.

GUO, Y.; ZHAO, W. Hydrothermal synthesis of highly fluorescent nitrogen-doped carbon quantum dots with good biocompatibility and the application for sensing ellagic acid. **Spectrochimica Acta - Part A: Molecular and Biomolecular Spectroscopy**, v. 240, p. 118580, out. 2020.

HAIKE GHAZARIAN, BRIAN IDONI, AND S. B. O. A glycobiology review: carbohydrates, lectins, and implications in cancer therapeutics. v. 113, n. 3, p. 236–247, 2012.

HASSERJIAN, R. P. Myelodysplastic Syndrome Updated. **Pathobiology**, v. 86, n. 1, p. 53–

61, 2019.

HIRABAYASHI, J. Concept, strategy and realization of lectin-based glycan profiling. **Journal of Biochemistry**, v. 144, n. 2, p. 139–147, 2008.

HONG, G. *et al.* Carbon Nanomaterials for Biological Imaging and Nanomedicinal Therapy. 2015.

HOTELLING, H. Analysis of a complex of statistical variables into principal components. **Journal of Educational Psychology**, v. 24, n. 6, p. 417–441, 1933.

HU, Q. *et al.* An ultra-selective fluorescence method with enhanced sensitivity for the determination of manganese (VII) in food stuffs using carbon quantum dots as nanoprobe. **Journal of Food Composition and Analysis**, v. 88, p. 103447, maio 2020.

HU, Q. *et al.* Binder-free CuO nanoneedle arrays based tube-type sensor for H2S gas sensing. **Sensors and Actuators B: Chemical**, v. 326, p. 128993, 2021.

HUANG, S. *et al.* Novel up-conversion carbon quantum dots/α-FeOOH nanohybrids eliminate tetracycline and its related drug resistance in visible-light responsive Fenton system. **Applied Catalysis B: Environmental**, v. 263, n. October 2019, p. 118336, 2020.

HUANG, X. *et al.* Carbon quantum dot (CQD)-modified Bi3O4Br nanosheets possessing excellent photocatalytic activity under simulated sunlight. **Materials Science in Semiconductor Processing**, v. 122, n. October 2020, p. 105489, 2021.

JACQUES, A. V. *et al.* Lectin from Canavalia brasiliensis (ConBr) protects hippocampal slices against glutamate neurotoxicity in a manner dependent of PI3K/Akt pathway. **Neurochemistry International**, v. 62, n. 6, p. 836–842, 2013.

JIA, J. *et al.* Spectrochimica Acta Part A : Molecular and Biomolecular Spectroscopy Highly luminescent N-doped carbon dots from black soya beans for free radical scavenging , Fe 3 + sensing and cellular imaging. **Spectrochimica Acta Part A: Molecular and Biomolecular Spectroscopy**, v. 211, p. 363–372, 2019.

JIANG, Q. *et al.* Potentiality of carbon quantum dots derived from chitin as a fluorescent sensor for detection of ClO−. **Microchemical Journal**, v. 157, p. 105111, set. 2020.

JING, W. e*t al.* Fluorescence sensor array based on amino acids-modulating quantum dots for the discrimination of metal ions. **Analytica Chimica Acta**, v. 985, p. 175–182, 2017.

JU, B. *et al.* absorption and emission dual-mode responses. p. 168–174, 2019.
KEERTHI VASAN, K.; SURENDIRAN, B. Dimensionality reduction using Principal Component Analysis for network intrusion detection. **Perspectives in Science**, v. 8, p. 510–512, set. 2016.

KHAN, Z. G.; PATIL, P. O. **A comprehensive review on carbon dots and graphene quantum dots based fluorescent sensor for biothiols**. **Microchemical Journal**Elsevier Inc., , set. 2020.

KHAN, Z. M. S. H. *et al.* A facile one step hydrothermal synthesis of carbon quantum dots for label -free fluorescence sensing approach to detect picric acid in aqueous solution. **Journal of Photochemistry and Photobiology A: Chemistry**, v. 388, p. 112201, fev. 2020.

KIM, J. Sensors and Actuators B : Chemical N-doped carbon dots with tunable emission for multifaceted application : solvatochromism , moisture sensing , pH sensing , and solid state multicolor lighting. **Sensors & Actuators: B. Chemical**, v. 295, n. March, p. 12–21, 2019.

KONAR, S. *et al.* Sensors and Actuators B : Chemical N-doped carbon dot as fluorescent probe for detection of cysteamine and multicolor cell imaging. **Sensors & Actuators: B. Chemical**, v. 286, n. November 2018, p. 77–85, 2019.

KUMAR, N. *et al.* **Chemometrics tools used in analytical chemistry: An overview**. **Talanta**Elsevier B.V., , jun. 2014.

KWAN, M. N. H. *et al.* Carbon-dot dispersal in PVA thin film for food colorant sensing. **Journal of Environmental Chemical Engineering**, v. 8, n. 3, p. 103187, jun. 2019.

LAKOWICZ, J. R. **Principles of fluorescence spectroscopy, 3rd Edition, Joseph R. Lakowicz, editor**. [s.l: s.n.].

LEGIN, A.; RUDNITSKAYA, A.; NATALE, C. D. I. ANALYTICAL CHEMISTRY DIVISION * NONSPECIFIC SENSOR ARRAYS (“ ELECTRONIC TONGUE ”) FOR CHEMICAL ANALYSIS OF LIQUIDS (IUPAC Technical Report) Nonspecific sensor arrays (“ electronic tongue ”) for chemical analysis of liquids (IUPAC Technical Report). v. 77, n. 11, p. 1965–1983, 2005.

LENG, T. *et al.* Quantitative detection of binary and ternary adulteration of minced beef meat with pork and duck meat by NIR combined with chemometrics. **Food Control**, v. 113, p. 107203, jul. 2020.

LI, Y. *et al.* Detection of tannic acid exploiting carbon dots enhanced hydrogen peroxide/potassium ferricyanide chemiluminescence. **Microchemical Journal**, v. 157, n. May, p. 105113, 2020.

LI, Z.; ASKIM, J. R.; SUSLICK, K. S. The Optoelectronic Nose: Colorimetric and Fluorometric Sensor Arrays. **Chemical Reviews**, v. 119, n. 1, p. 231–292, 2019.

LIAO, S. *et al.* Talanta Nitrogen-doped carbon dots rapid and selective detection of mercury ion and biothiol and construction of an IMPLICATION logic gate. **Talanta**, v. 194, n. October 2018, p. 554–562, 2019.

LIM, S. Y.; SHEN, W.; GAO, Z. Carbon quantum dots and their applications. **Chemical Society Reviews**, v. 44, n. 1, p. 362–381, 2015.

LIN, H. *et al.* Stable and efficient hybrid Ag-In-S/ZnS@SiO2-carbon quantum dots nanocomposites for white light-emitting diodes. **Chemical Engineering Journal**, v. 393, n. January, p. 124654, 2020.

LIU, Q. *et al.* Differentiation of cancer cell type and phenotype using quantum dot-gold

nanoparticle sensor arrays. **Cancer Letters**, v. 334, n. 2, p. 196–201, 2013.

LIU, S. *et al.* Spectrochimica Acta Part A : Molecular and Biomolecular Spectroscopy Facile one-pot synthesis of highly fl uorescent nitrogen-doped carbon dots by mild hydrothermal method and their applications in detection of Cr (VI) ions. **Spectrochimica Acta Part A: Molecular and Biomolecular Spectroscopy**, v. 206, p. 65–71, 2019.

LIU, W. *et al.* Carbon dots : surface engineering and applications. p. 5772–5788, 2016.

LIU, W. *et al.* Carbon-dot-based ratiometric fluorescent pH sensor for the detections of very weak acids assisted by auxiliary reagents that contribute to the release of protons. **Sensors and Actuators, B: Chemical**, v. 244, p. 441–449, 2017.

LU, W. *et al.* Analytica Chimica Acta Comparative study for N and S doped carbon dots : Synthesis , characterization and applications for Fe 3 þ probe and cellular imaging. **Analytica Chimica Acta**, v. 898, p. 116–127, 2015.

LUO, Q. *et al.* A 3D porous fluorescent hydrogel based on amino-modified carbon dots with excellent sorption and sensing abilities for environmentally hazardous Cr(VI). **Journal of Hazardous Materials**, v. 401, p. 123432, jan. 2021.

LUO, X. *et al.* Carbon dots derived fluorescent nanosensors as versatile tools for food quality and safety assessment: A review. **Trends in Food Science and Technology**, v. 95, n. September 2019, p. 149–161, 2020.

MA, J. *et al.* Mass production of highly fluorescent full color carbon dots from the petroleum coke. **Chinese Chemical Letters**, n. 2019, 2020a.

MA, S. *et al.* Silver nanoclusters and carbon dots based light-addressable sensors for multichannel detections of dopamine and glutathione and its applications in probing of parkinson's diseases. **Talanta**, v. 219, p. 121290, 2020b.

MANIOUDAKIS, J. et al. As featured in : properties of carbon dots †. 2019.

MARTÍ, R. B.; BALDRICH, J. F. Fundamentals of PARAFAC. Em: **Data Handling in Science and Technology**. [s.l.] Elsevier Ltd, 2015. v. 29p. 7–35.

MAYNAR, M. *et al.* Serum concentration of cobalt, molybdenum and zinc in aerobic, anaerobic and aerobic-anaerobic sportsmen. **Journal of the International Society of Sports Nutrition**, v. 15, n. 1, p. 1–8, 2018.

MENG, A. *et al.* Sensors and Actuators B : Chemical A highly selective and sensitive " on-off-on " fluorescent probe for detecting Hg (II) based on Au / N-doped carbon quantum dots. **Sensors & Actuators: B. Chemical**, v. 255, p. 657–665, 2018.

MESSAI, H. *et al.* Chemometrics Methods for Specificity, Authenticity and Traceability Analysis of Olive Oils: Principles, Classifications and Applications. **Foods**, v. 5, n. 4, p. 77, nov. 2016.

MIAO, S. *et al.* Hetero-atom-doped carbon dots: Doping strategies, properties and

applications. **Nano Today**, v. 33, p. 100879, 2020.

MONAKHOVA, Y. B.; GORYACHEVA, I. Y. **Chemometric analysis of luminescent quantum dots systems: Long way to go but first steps taken**. **TrAC - Trends in Analytical Chemistry**Elsevier B.V., , set. 2016.

MONCAYO, S. *et al.* Evaluation of supervised chemometric methods for sample classification by Laser Induced Breakdown Spectroscopy. **Chemometrics and Intelligent Laboratory Systems**, v. 146, p. 354, ago. 2015.

NAIR, A. *et al.* Natural carbon-based quantum dots and their applications in drug delivery: A review. **Biomedicine and Pharmacotherapy**, v. 132, n. October, p. 110834, 2020.

NI, P. *et al.* Applied Surface Science Optical properties of nitrogen and sulfur co-doped carbon dots and their applicability as fl uorescent probes for living cell imaging. **Applied Surface Science**, v. 494, n. July, p. 377–383, 2019.

NIU, W. *et al.* Nano Energy Highly stable nitrogen-doped carbon nanotubes derived from carbon dots and metal-organic frameworks toward excellent e ffi cient electrocatalyst for oxygen reduction reaction. **Nano Energy**, v. 63, n. May, p. 103788, 2019.

OLAWOYIN, R. Nanotechnology : The future of fi re safety. v. 110, n. August, p. 214–221, 2018.

ONLINE, V. A. Nitrogen-doped, carbon-rich, highly photoluminescent carbon dots from ammonium citrate †. p. 1890–1895, 2014.

OTYEPKA, M.; ZBOR, R. Graphitic Nitrogen Triggers Red Fluorescence in Carbon Dots. 2017.

PEARSON, K. LIII. On lines and planes of closest fit to systems of points in space. **The London, Edinburgh, and Dublin Philosophical Magazine and Journal of Science**, v. 2, n. 11, p. 559–572, nov. 1901.

PENG, J. *et al.* Graphene Quantum Dots Derived from Carbon Fibers. 2012.

PINTO, L.; STECHI, F.; BREITKREITZ, M. C. A simplified and versatile multivariate calibration procedure for multiproduct quantification of pharmaceutical drugs in the presence of interferences using first order data and chemometrics. **Microchemical Journal**, v. 146, p. 202–209, maio 2019.

QU, C. *et al.* Spectrochimica Acta Part A : Molecular and Biomolecular Spectroscopy Nitrogen and sulfur co-doped graphene quantum dots for the highly sensitive and selective detection of mercury ion in living cells. **Spectrochimica Acta Part A: Molecular and Biomolecular Spectroscopy**, v. 206, p. 588–596, 2019.

QU, D. *et al.* Formation mechanism and optimization of highly luminescent N-doped graphene. p. 1–11, 2014.

RABATEL, G. *et al.* VSN: Variable sorting for normalization. **Journal of Chemometrics**, v.

34, n. 2, fev. 2020.

RAFI, P. Nanoscale Advances. v. 1, n. 1, 2019.

RAJA, D.; SUNDARAMURTHY, D. Facile synthesis of fluorescent carbon quantum dots from Betel leafs (Piper betle) for Fe3+sensing. **Materials Today: Proceedings**, abr. 2020.

RAMAMURTHY, K.; PONNUSAMY, K.; CHELLAPPAN, S. Excitation-resolved area-normalized emission spectroscopy: A rapid and simple steady-state technique for the analysis of heterogeneous fluorescence. **RSC Advances**, v. 10, n. 2, p. 998–1006, jan. 2019.

RANI, U. A. *et al.* A review of carbon quantum dots and their applications in wastewater treatment. **Advances in Colloid and Interface Science**, v. 278, p. 102124, abr. 2020.

RAZA, A. *et al.* The Biology of Myelodysplastic Syndromes: Unity Despite Heterogeneity. **Hematology Reports**, v. 2, n. 1, p. e4, 2010.

RAZA, A.; ALI, A.; IVERSON, N. Developments in the treatment of transfusion-dependent anemia in patients with myelodysplastic syndromes: epidemiology, etiology, genetics, and targeted therapies. **Advances in Genomics and Genetics**, p. 95, 2014.

RAZA, A.; GALILI, N. The genetic basis of phenotypic heterogeneity in myelodysplastic syndromes. **Nature Reviews Cancer**, v. 12, n. 12, p. 849–859, 2012.

REN, J. *et al.* Electronic Supplementary Material (ESI) for Nanoscale . This journal is © The Royal Society of Chemistry 2018 Electronic Supplementary information Influence of surface chemistry on optical , chemical and electronic properties of blue luminescent carbon . p. 1–8, 2018.

RIEGER, D. K. *et al.* Antidepressant-like effect of Canavalia brasiliensis (ConBr) lectin in mice: Evidence for the involvement of the glutamatergic system. **Pharmacology Biochemistry and Behavior**, v. 122, p. 53–60, 2014a.

RIEGER, D. K. *et al.* ConBr, a lectin from Canavalia brasiliensis seeds, modulates signaling pathways and increases BDNF expression probably via a glycosylated target. **Journal of Molecular Recognition**, v. 27, n. 12, p. 746–754, 2014b.

RIEGER, D. K. *et al.* ConBr, A Lectin Purified from the Seeds of Canavalia brasiliensis, Protects Against Ischemia in Organotypic Culture of Rat Hippocampus: Potential Implication of Voltage-Gated Calcium Channels. **Neurochemical Research**, v. 42, n. 2, p. 347–359, 2017.

RUSSI, M. A. *et al.* ConBr, a lectin from canavalia brasiliensis seeds, protects against quinolinic acid-induced seizures in mice. **Neurochemical Research**, v. 37, n. 2, p. 288–297, 2012.

SACCENTI, E.; CAMACHO, J. Multivariate Exploratory Data Analysis Using Component Models. Em: **Reference Module in Food Science**. [s.l.] Elsevier, 2020.

SCHNEIDER, J. *et al.* Molecular fluorescence in citric acid-based carbon dots. **Journal of Physical Chemistry C**, v. 121, n. 3, p. 2014–2022, 2017.

SHAMSIPUR, M. *et al.* Sensors and Actuators B : Chemical One-step synthesis and characterization of highly luminescent nitrogen and phosphorus co-doped carbon dots and their application as highly selective and sensitive nanoprobes for low level detection of uranyl ion in hair . **Sensors & Actuators: B. Chemical**, v. 257, p. 772–782, 2018.

SHAMSIPUR, M.; BARATI, A.; KARAMI, S. dots : Achievements made , challenges remaining , and applications. v. 124, 2017.

SHI, C. *et al.* Materials Science & Engineering C N , S-self-doped carbon quantum dots from fungus fi bers for sensing tetracyclines and for bioimaging cancer cells. **Materials Science & Engineering C**, v. 105, n. January, p. 110132, 2019a.

SHI, Y. *et al.* International Journal of Biological Macromolecules Synthesis of N-doped carbon quantum dots from bio-waste lignin for selective irons detection and cellular imaging. **International Journal of Biological Macromolecules**, v. 128, p. 537–545, 2019b.

SILVA, A. F. B. *et al.* International Immunopharmacology Comparison of immunomodulatory properties of mannose-binding lectins from Canavalia brasiliensis and Cratylia argentea in a mice model of Salmonella infection. v. 31, p. 233–238, 2016.

SILVA, F. DE O. *et al.* Antiproliferative effect of Canavalia brasiliensis lectin on B16F10 cells. **Research in Veterinary Science**, v. 96, n. 2, p. 276–282, 2014.

SINGH, R. *et al.* QPRTase modified N-doped carbon quantum dots: A fluorescent bioprobe for selective detection of neurotoxin quinolinic acid in human serum. **Biosensors and Bioelectronics**, v. 101, n. October 2017, p. 103–109, 2018.

SONG, X. *et al.* Synthesis of multi-color fl uorescent carbon quantum dots and solid state CQDs @ SiO 2 nanophosphors for light-emitting devices. **Ceramics International**, v. 45, n. 14, p. 17387–17394, 2019.

SONG, Y. *et al.* High capacity and rate capability of S / 3D ordered bimodal mesoporous carbon cathode for lithium / sulfur batteries. p. 1–8, 2018.

SOUSA, B. *et al.* International Journal of Biological Macromolecules One century of ConA and 40 years of ConBr research : A structural review. **International Journal of Biological Macromolecules**, v. 134, p. 901–911, 2019.

SUN, J. *et al.* **Colorimetric sensor array based on gold nanoparticles: Design principles and recent advances**. **TrAC - Trends in Analytical Chemistry**Elsevier B.V., , jan. 2020.

SUN, S. *et al.* Applying Carbon Dots-Metal Ions Ensembles as a Multichannel Fluorescent Sensor Array: Detection and Discrimination of Phosphate Anions. 2017a.

SUN, X.; LEI, Y. Fluorescent carbon dots and their sensing applications. **TrAC - Trends in Analytical Chemistry**, v. 89, p. 163–180, 2017.

SUN, X.; WANG, Y.; LEI, Y. Fluorescence based explosive detection: From mechanisms to sensory materials. **Chemical Society Reviews**, v. 44, n. 22, p. 8019–8061, 2015.

SUN, Y. *et al.* RSC Advances carbon dots for cell imaging and ion detecting. p. 16368–16375, 2015.

SUN, Y. *et al.* Magnetism of graphene quantum dots. **npj Quantum Materials**, v. 2, n. 1, p. 5, 2017b.
Systat Introduction. [s.d.].

TEJWAN, N.; SAHA, S. K.; DAS, J. **Multifaceted applications of green carbon dots synthesized from renewable sources**. **Advances in Colloid and Interface Science**Elsevier B.V., , jan. 2020.

TIAN, M. *et al.* Facile synthesis of yellow fluorescent carbon dots for highly sensitive sensing of cobalt ions and biological imaging. **Analytical Methods**, v. 11, n. 32, p. 4077–4083, 2019.

TRAVLOU, N. A. *et al.* S- and N-doped carbon quantum dots : Surface chemistry dependent antibacterial activity. v. 135, p. 104–111, 2018.

VASHISHT, D. *et al.* Solvothermal assisted phosphate functionalized graphitic carbon nitride quantum dots for optical sensing of Fe ions and its thermodynamic aspects. **Spectrochimica Acta - Part A: Molecular and Biomolecular Spectroscopy**, v. 228, p. 117773, mar. 2020.

WANG, B. Concentration-induced multi-colored emissions in carbon dots: origination from triple fluorescent centers. p. 6734–6743, 2018.

WANG, X. *et al.* Colloids and Surfaces B : Biointerfaces Novel Enteromorpha Prolifera based carbon dots : Probing the radical scavenging of natural phenolic compounds. v. 174, n. November 2018, p. 161–167, 2019.

WANG, Y. *et al.* Ratiometric fluorescent paper sensor utilizing hybrid carbon dots-quantum dots for the visual determination of copper ions. **Nanoscale**, v. 8, n. 11, p. 5977–5984, 2016.

WANG, Z. *et al.* Fluorescence sensor array based on amino acid derived carbon dots for pattern-based detection of toxic metal ions. **Sensors and Actuators, B: Chemical**, v. 241, p. 1324–1330, 2017.

WEI, Z. *et al.* Green synthesis of nitrogen and sulfur co-doped carbon dots from Allium fistulosum for cell. p. 718–723, 2019.

WINTER, S. *et al.* Integrating the “Immunome” in the stratification of myelodysplastic syndromes and future clinical trial design. **Journal of Clinical Oncology**, v. 38, n. 15, p. 1723–1735, 2020.

WOLD, S.; ESBENSEN, K.; GELADI, P. Principal component analysis. **Chemometrics and Intelligent Laboratory Systems**, v. 2, n. 1–3, p. 37–52, ago. 1987.

WOLIN, I. A. V. *et al.* ConBr lectin modulates MAPKs and Akt pathways and triggers autophagic glioma cell death by a mechanism dependent upon caspase-8 activation. **Biochimie**, v. 180, p. 186–204, 2021.

WU, L. *et al.* **A graphene-based chemical nose/tongue approach for the identification of normal, cancerous and circulating tumor cells**. **NPG Asia Mater**The Author(s) Nature Publishing Group, , mar. 2017.

WU, T. *et al.* Controllable Chain-Length for Covalent Sulfur – Carbon Materials Enabling Stable and High-Capacity Sodium Storage. v. 1803478, p. 1–11, 2019.

XU, S. *et al.* Rapid synthesis of nitrogen doped carbon dots and their application as a label free sensor array for simultaneous discrimination of multiple proteins. **Journal of Materials Chemistry B**, v. 5, n. 44, p. 8748–8753, nov. 2017a.

XU, X. *et al.* Electrophoretic analysis and purification of fluorescent single-walled carbon nanotube fragments. **Journal of the American Chemical Society**, v. 126, n. 40, p. 12736–12737, 2004.

XU, Y. *et al.* Enhanced-quantum yield sulfur/nitrogen co-doped fluorescent carbon nanodots produced from biomass Enteromorpha prolifera: Synthesis, posttreatment, applications and mechanism study. **Scientific Reports**, v. 7, n. 1, p. 1–12, 2017b.

YADAV, P. K. *et al.* A Facile Synthesis of Green-Blue Carbon Dots from Artocarpus lakoocha Seeds and Their Application for the Detection of Iron (III) in Biological Fluids and Cellular Imaging. **ChemistrySelect**, v. 4, n. 42, p. 12252–12259, 2019.

YANG, L. *et al.* Doxorubicin conjugated functionalizable carbon dots for nucleus targeted delivery and enhanced therapeutic efficacy. p. 6801–6809, 2016.

YANG, Q. *et al.* Precise surface state control of carbon quantum dots to enhance charge extraction for solar cells. **Nanomaterials**, v. 10, n. 3, 2020.

YAO, B. *et al.* Carbon Dots: A Small Conundrum. **Trends in Chemistry**, v. 1, n. 2, p. 235–246, 2019.

YI, Z. *et al*. High quantum yield photoluminescent N-doped carbon dots for switch sensing and imaging. **Talanta**, v. 222, n. July 2020, p. 121663, 2021.

YOU, A.; BE, M. A. Y.; IN, I. Fluorescently tuned nitrogen-doped carbon dots from carbon source with different content of carboxyl groups. v. 086102, n. August 2015, p. 1–8, 2016.

YOUSEFI-DARANI, A. *et al.* Model-based calibration of a gas sensor array for on-line monitoring of ethanol concentration in Saccharomyces cerevisiae batch cultivation. **Biosystems Engineering**, v. 198, p. 198–209, 2020.

YU, J. *et al.* Facilely synthesized N-doped carbon quantum dots with high fluorescent yield for sensing Fe 3 +. p. 2083–2088, 2016.

YUAN, G. *et al.* Journal of Colloid and Interface Science Small nitrogen-doped carbon dots as efficient nanoenhancer for boosting the electrochemical performance of three-dimensional graphene. **Journal of Colloid And Interface Science**, v. 536, p. 628–637, 2019.

ZHANG, C. *et al.* Selective determination of DNA based on the fluorescence recovery of

carbon dots quenched by Ru(bpy)2(dppz)2+. **Talanta**, v. 217, n. May, 2020a.

ZHANG, H. *et al.* Fluorescence Determination of Nitrite in Water Using Prawn-Shell Derived Nitrogen-Doped Carbon Nanodots as Fluorophores. **ACS Sensors**, v. 1, n. 7, p. 875–881, 2016.

ZHANG, J. *et al.* Talanta Folic acid-conjugated green luminescent carbon dots as a nanoprobe for identifying folate receptor-positive cancer cells. **Talanta**, v. 183, n. February, p. 39–47, 2018.

ZHANG, T. *et al.* hydrogen bond dominated molecular states. p. 13042–13051, 2017.

ZHANG, X.; ZHANG, W.; TANG, S. Journal of Photochemistry & Photobiology A : Chemistry L-Tryptophan functionalized graphene quantum dots as a fluorescence indicator for pH detection in real water. **Journal of Photochemistry & Photobiology, A: Chemistry**, v. 372, n. December 2018, p. 71–77, 2019.

ZHANG, X.-P. *et al.* Single gold nanocluster probe-based fluorescent sensor array for heavy metal ion discrimination. **Journal of Hazardous Materials**, p. 124259, 2020b.

ZHAO, J. *et al.* Protein biomarkers in cancer: natural glycoprotein microarray approaches. **Current opinion in molecular therapeutics**, v. 10, n. 6, p. 602–10, dez. 2008.

ZHAO, Y. *et al.* Analytica Chimica Acta Simple and sensitive fl uorescence sensor for methotrexate detection based on the inner fi lter effect of N , S co-doped carbon quantum dots. **Analytica Chimica Acta**, v. 1047, p. 179–187, 2019.

ZHENG, M.; XIE, Z. A carbon dots e based nanoprobe for intracellular Fe 3 þ detection. **Materials Today Chemistry**, v. 13, p. 121–127, 2019.

ZHI, B. *et al.* Investigation of phosphorous doping effects on polymeric carbon dots : Fluorescence , photostability , and environmental impact. v. 129, p. 438–449, 2018.

ZHOU, J. *et al.* RSC Advances Facile synthesis of P-doped carbon quantum dots with highly e ffi cient photoluminescence †. p. 5465–5468, 2014.

ZHOU, L. *et al.* Electrochemical luminescence sensor based on CDs@HKUST-1 composite for detection of catechol. **Journal of Electroanalytical Chemistry**, v. 871, p. 114215, 2020.

ZHU, J. *et al.* Sensors and Actuators B : Chemical Fluorescent carbon dots for auramine O determination and logic gate operation. **Sensors & Actuators: B. Chemical**, v. 219, p. 261–267, 2015a.

ZHU, J. *et al.* Carbon dots with efficient solid-state photoluminescence towards white light-emitting diodes. **Journal of Materials Chemistry C**, v. 5, n. 44, p. 11416–11420, 2017.

ZHU, J. *et al.* Emitting color tunable carbon dots by adjusting solvent towards light-emitting devices. **Nanotechnology**, v. 29, n. 8, 2018a.

ZHU, J. *et al.* solvent towards light-emitting devices Emitting color tunable carbon dots by

adjusting solvent towards light-emitting devices. 2018b.

ZHU, J. *et al.* Fluorescent probe based nitrogen doped carbon quantum dots with solid-state fluorescence for the detection of Hg2+ and Fe3+ in aqueous solution. **Microchemical Journal**, v. 158, p. 105142, nov. 2020.

ZHU, S. *et al.* The photoluminescence mechanism in carbon dots (graphene quantum dots, carbon nanodots, and polymer dots): current state and future perspective. **Nano Research**, v. 8, n. 2, p. 355–381, 2015b.

ZU, F. *et al.* The quenching of the fluorescence of carbon dots: A review on mechanisms and applications. **Microchimica Acta**, v. 184, n. 7, p. 1899–1914, 2017.